Stony Brook University

Synthesis and Characterization of Bimetallic Core-Shell-Supported Platinum Monolayer Electrocatalysts for the Oxygen Reduction Reaction

A Dissertation Presented

by

Kurian Abraham Kuttiyiel

to

The Graduate School

in Partial Fulfillment of the

Requirements

for the Degree of

Doctor of Philosophy

in

Material Science and Engineering

Stony Brook University

August 2011

Stony Brook University

The Graduate School

Kurian Abraham Kuttiyiel

We, the dissertation committee for the above candidate for the
Doctor of Philosophy degree, hereby recommend
acceptance of this dissertation.

Dr. Radoslav Adzic, Dissertation Advisor
Chemistry Department, Brookhaven National Laboratory

Dr. Devinder Mahajan, Chairperson of Defense
Department of Materials Science and Engineering

Dr. Hugh Isaacs, Adjunct Faculty
Department of Materials Science and Engineering

Dr. Kotaro Sasaki, Outside Member
Chemistry Department, Brookhaven National Laboratory

This dissertation is accepted by the Graduate School

Lawrence Martin
Dean of the Graduate School

Abstract of the Dissertation

Synthesis and Characterization of Bimetallic Core-Shell-Supported Platinum Monolayer Electrocatalysts for the Oxygen Reduction Reaction

by

Kurian Abraham Kuttiyiel

Doctor of Philosophy

in

Materials Science and Engineering

Stony Brook University

2011

Fuel cells are expected to be one of the major clean energy sources in the near future. However, the slow kinetics of electrocatalytic oxygen reduction reaction (ORR) and the high loading of Platinum (Pt) for the cathode material are the urgent issues to be addressed since they determine the efficiency and the cost of this energy source. In this study, a new approach was developed for designing electrocatalysts for the ORR in fuel cells. These electrocatalysts consist of only one Pt monolayer on suitable carbon-supported Iridium-Nickel (IrNi) core-shell nanoparticles. The synthesis involved depositing a monolayer of Copper (Cu) on IrNi metal alloy surface at under-potentials, followed by galvanic displacement of the Cu monolayer with Pt.

It was found that the electronic properties of Pt monolayer could be fine-tuned by the electronic and geometric effects introduced by the substrate metal. The Pt mass activity of the new Pt monolayer IrNi electrocatalysts was up to six times higher than the state-of-the-art commercial Pt/C catalysts. The structure and composition of the core-shell nanoparticles were

verified using transmission electron microscopy and in situ X-ray absorption spectroscopy, while potential cycling test was employed to confirm the stability of the electrocatalyst. The formation of Ir shell on IrNi alloy during annealing due to thermal segregation was monitored by time-resolved synchrotron XRD measurements. Our experimental results, supported by computations, demonstrated an effective way of using Pt that can resolve key ORR problems which include inadequate activity and durability while minimizing the Pt loading.

To my wife

and

parents

Table of Contents

List of Figures

List of Tables

List of Abbreviations

PEM	Proton exchange membrane
PEMFC	Proton exchange membrane fuel cell
f.c.c	Face centered close-packed
h.c.p.	Hexagonal close-packed
Pt_{ML}/Ni-Ir/C	Platinum monolayer deposited on carbon-supported Nickel- Iridium nanoparticles
ORR	Oxygen reduction reaction
STM	Scanning tunneling microscopy
TEM	Transmission electron microscopy
XAS	X-ray absorption spectroscopy
EXAFS	Extended X-ray absorption fine structure
XANES	X-ray absorption near edge structure
PGM	Platinum Group Metal
XRD	X-ray diffraction technique
UPD	Under potential deposition
OCP	Open circuit potential
OPD	Overpotential deposition
RDE	Rotating disk electrode
RRDE	Rotating ring disk electrode
E	Potential (V)
F	Faraday constant (96487 C mol^{-1})
R	Universal gas constant (8.314 J K^{-1} mol^{-1})
G	Gibbs free energy (J)
T	Temperature (K)
i_o	Exchange current (mA)
i_k	Kinetic current (mA)
$i_{l,c}$	Cathode limiting current (mA)
$i_{l,a}$	Anode limiting current (mA)

j	Current density (mA cm^{-2})
A	Catalyst geometric surface area (cm^2)
C_o	Oxygen bulk concentration in electrolyte (mole cm^{-3})
D_o	Oxygen diffusion coefficient (cm^2 s^{-1})
μ	Specific Gibbs free energy (J/mol)
ν	Electrolyte dynamic viscosity (cm^2 s^{-1})
ω	Rotating rate of the electrode (rpm)
η	Overpotential (V)
α	Transfer coefficient in Bulter-Volmer equation

Superscript

*	Bulk Phase
+	Positive charge
_	Negative charge

Subscript

ML	Atomic monolayer
a	Adsorption
l	Liquid phase
g	Gas phase
s	solid phase

Preface

The developments in the discipline of electrochemistry have been rapid and on a remarkably wide front. A generation ago, for example, aside from some optical methods, synchrotron spectroscopy had little to offer electrochemistry; now it is one of the major methods to study the electrode surface. New materials, often developed for different purpose, have allowed us to develop new technologies.

Originally, I had thought of my intended dissertation work as a kind of ordeal. Judging from what successful colleagues had told me, finding a worthwhile Ph.D. thesis, writing a dissertation, and persisting in all trials is like descending to hell. Nothing of this has happened to me. I managed to nail down the thesis proposal in 2009, continue with my research and its consolidation in 2010, and finish writing up the dissertation in 2011. One reason for this is the guidance and support I received from my advisor, Radoslav Adzic. I have learned immensely from him. He taught me how to find direction in Ph.D. thesis work, drill down to the essentials, and make a dissertation out of it. I am highly grateful to him for making my Ph.D. thesis work such a smooth and rewarding experience.

This dissertation has resulted in a number of publications and has also acknowledged me in the field of fuel cell technologies by receiving the 2010 Dr. Bernard S. Baker student award for fuel cell research.

August 2011 *Kurian A. Kuttiyiel*

Acknowledgements

It is a pleasure for me to acknowledge the contributions of many people to this dissertation. My advisor Dr. Radoslav Adzic, who introduced me into the field of electrochemistry, directed and supervised my research with patience and constant encouragement. His dedication and diligent work ethic is inspirational to me.

I would also like to thank Dr. Devinder Mahajan, Dr. Sasaki Kotaro, Dr. Hugh Isaacs and Dr. Hazem Tawfik for their serving on my committee. Their suggestions have been invaluable to me in many areas. To them, I express my sincere gratitude.

My great debt to, Dr. Misha Vukmirovic, Dr. Laura Barrio, Dr. Dong Su, Dr. YongMan Choi, Dr. Ping Liu, Dr. Anatoly Frenkel, Dr. Marinkovic Nebojsa, Dr. Kauping Gong and Meng Li for their assistance, collaboration, discussion, and friendship. I owe an equally great debt to my friends and professional colleagues, who patiently explained the subtleties of their subjects and read my drafts.

I would like to express profound appreciation to my dear wife, Sujai Jacob, for her patience, understanding, continuing support and encouragement. She and her support are the biggest treasure I always own.

Finally, I would like to acknowledge the research sponsorship from U.S. Department of Energy, Divisions of Chemical and Material Sciences, under Contract No. DE-AC02-98CH10886.

Publications

Peer-Reviewed Journal Papers

1. **K. Kuttiyiel**, K. Sasaki, Y. Choi, D. Su, P. Liu, R. Adzic
   Bimetallic IrNi core Pt monolayer Shell electrocatalyst for the Oxygen Reduction Reaction
   submitted to Energy Environ. Science

2. K. Sasaki, **K. Kuttiyiel**, L. Barrio, D. Su, A. Frenkel, N. Marinkovic, D. Mahajan, R. Adzic
   Carbon-supported IrNi core-shell nanoparticles: Synthesis, characterization and catalytic activity for H_2 Oxidation
   J. Phys. Chem. C, 2011, 115, 9894–9902.

3. K. Sasaki, **K. Kuttiyiel**, D. Su, R. Adzic
   Pt Monolayer on Ir-Fe core-shell nanoparticles electrocatalysts for ORR
   Electrocatal, 2011, 2, 134-140.

Conference Papers

1. DOE E-Beam Micro-characterization Centers and Nanoscale Science Research Centers Contractors' Meeting, Annapolis, Maryland (June 2011)
   Core-Protected Platinum Monolayer Shell High-Stability Electrocatalysts for Fuel-Cell Cathode

2. 219th Electrochemical Society Meeting, Montreal, QC, Canada (May 2011)
   Carbon Supported IrNi Core-Shell Nanoparticles: Synthesis, Characterization, and Catalytic Activity for H_2 Oxidation

3. 218th Electrochemical Society Meeting, Las Vegas, Nevada (Oct 2010)
   Bimetallic Ni-Ir Core Platinum Monolayer Shell Electrocatalysts for the Oxygen Reduction Reaction

4. Fuel Cell Seminar, San Antonio, Texas (Oct 2010)
   Platinum Monolayer on Ni-Ir Core Shell Electrocatalysts for the Oxygen Reduction Reaction

5. DOE review, Center of Functional Nanomaterials, BNL, NY (Sept 2010)
   Platinum Monolayer Shell Electrocatalysts for the Oxygen Reduction Reaction

Chapter 1. Introduction

The basic use of fuel cells is to generate electricity from the reactions of fuel (hydrogen) and oxidant (oxygen) on the anode and cathode of an electrochemical cell and was discovered by William Grove in the middle of the 19^{th} century [1]. Similar to batteries, fuel cells convert chemical energy of fuel and oxidant into energy. But unlike batteries, they do not require recharging as long as fuel and oxidant are continuously supplied. Nowadays finite resources of fossil fuels and environmental concerns, like global warming, have stimulated a broad interest in the development of alternative clean power sources. Compared with thermal engines, fuel cells show superior characteristics such as high efficiency, no environment pollution and quiet operation. Novel materials are helping to give the newest generation of fuel cell vehicles adequate durability and cheaper price tags. Therefore, fuel cells are expected to experience widespread commercial use in the areas of transportation and residential applications.

1.1 Fuel Cell Basics

The basic structure and the working principle are similar for all fuel cells. Two electrodes, anode and cathode are electronically separated by electrolyte that provides ionic conduction and circuit is closed externally by electronic conductors. At the anode, a fuel (H_2, CH_4, CH_3OH, or other hydrocarbons) is oxidized producing electrons, which are transferred to the cathode through an external circuit. While at the cathode, oxygen which is reduced to anion by the electrons from the anode meets with the H^+ diffusing from the anode and forms water. A fuel cell system, which includes a fuel reformer, can utilize any kind of hydrocarbon fuel from natural gas to methanol, and even gasoline.

1.1.1 Classification of Fuel Cell

Fuel cells are customarily classified according to the electrolyte employed, with different electrolytes working at different temperatures. The operating temperature and useful life of a fuel cell dictate the physicochemical and thermo mechanical properties of the materials used in the cell components (i.e., electrodes, electrolyte, interconnects, current collector, etc.). Aqueous electrolytes are limited to temperatures of about 200°C or lower because of their high water vapor pressure and rapid degradation at higher temperature. The operating temperature also plays an important role in dictating the type of fuel that can be used in a fuel cell. The low-temperature fuel cells with aqueous electrolytes are, in most practical applications, restricted to hydrogen as a fuel. In high temperature fuel cells, CO and even CH_4 can be used because of the inherently rapid electrode reaction kinetics and the lesser need for high catalytic activity at high temperature. All the existing fuel cells can be divided into five types based on the electrolyte that is used [2].

Proton Exchange Membrane Fuel Cells (PEMFCs): The electrolyte used in PEMFCs is a solid organic polymer poly-perflourosulfonic acid that conducts electricity by proton transfer. The solid electrolyte is an advantage because it reduces corrosion and management problems. These cells operate at relatively low temperature (about 80° C), have high power density, and vary their output quickly to meet shifts in power demand. Cell output generally ranges from 50kW~250kW. The only liquid in this fuel cell is water, so the problem of corrosion is minimal. Water management is critical for the efficient performance; the cell must operate under conditions where the byproduct water does not evaporate faster than it is produced because the

membrane must be hydrated. This type of fuel cell, however, is sensitive to fuel impurities. Because CO “poisons” the catalyst, the fuel may contain no CO.

Alkaline Fuel Cells (AFCs): These fuel cells use alkaline solution soaked in a matrix as the electrolyte, with a wide range of electrocatalysts that can be used (e.g. Ni, Ag, metal oxide, spinels, and noble metals). Cell efficiency can reach up to 70%. Operating temperature ranges from 150~250°C. One of the main advantages of AFC is that the activation overvoltage of oxygen reduction is smaller than that of PEMFC. However, the AFC is easily poisoned by CO_2 which react with the electrolyte (usually KOH) to form K_2CO_3, thus altering the electrolyte. Even the small amount of CO_2 in the air is detrimental to alkaline fuel cells, thus increasing the cost of purifying the fuel. They typically have a cell output of 300W~5kW. Long used by NASA in space mission, these cells are too costly for commercial use.

Phosphoric Acid Fuel Cells (PAFCs): As the most mature fuel cell technology, these cells are commercially available today. Concentrated phosphoric acid (up to 100%) retained in silicon carbide matrix is used as the electrolyte of these cells. The relative stability of concentrated phosphoric acid is high compared to other common acids; consequently PAFCs can operate at the high end of acid temperature. In addition, the use of concentrated acid minimizes the water vapor pressure so water management is not difficult in the cell. Operating temperature ranges from 150~200°C. At low temperature, phosphoric acid is a poor ion conductor. One of the main advantages of these cells is that it can use impure hydrogen as fuel. The CO tolerance is up to 1.5%. The electrocatalyst in both the anode and the cathode is Pt. Existing PAFCs have outputs up to 200kW.

Molten Carbonate Fuel Cells (MCFCs): This type of fuel cells uses molten lithium, sodium or potassium carbonates retained in a ceramic matrix for the electrolyte, with carbonate ions providing ionic conduction. High operating temperature (about 650°C) is needed to keep good conductivity of the molten carbonate electrolyte. Due to the high temperature, the advantages of these cells are high efficiency, less expansive catalyst, and fuel flexibility. Ni (anode) and nickel oxide (cathode) are adequate to promote reaction. Noble metals are not required. However, for the same reason of high operating temperature, enhanced corrosion and breakdown of the cell component are the disadvantages.

Solid Oxide Fuel Cells (SOFCs): As another highly promising fuel cell, SOFCs could be used in big, high-power applications including industrial and large-scale central electricity generating stations. Solid oxide system uses a non-porous hard ceramic material of solid zirconium oxide and a small amount of yttria, instead of a liquid electrolyte, allowing operating temperatures reach 1000°C. Oxygen ions provide ionic conduction in this fuel cell. Typically, the anode is Co-ZrO_2 or Ni-ZrO_2 cermet, and the cathode is Sr-doped $LaMnO_3$. Power generating efficiency is up to 60% and 85% for cogeneration, and cell output is up to 100kW.

The following Table (Table 1.1) gives a comparison of the five types of fuel cells on electrolyte, electrode catalysts, conductive ions, operating temperature, electrode reactions, and poisonous gas species.

	PEMFC	AFC	PAFC	MCFC	SOFC
Electrolyte	Hydrated polymeric ion exchanger	Potassium hydroxide in matrix	Phosphoric acid in SiC matrix	Molten carbonate in $LiAlO_2$	Perovskites (ceramics)
Electrodes	Carbon	Transition metals	Carbon	Nickel and nickel oxide	Perovskite and perovskite/ metal cermet
Catalysts	Platinum	Platinum	Platinum	Electrode material	Electrode material
Operating Temperature	80 °C	150~200 °C	150~200 °C	650 °C	600~1000 °C
Anode reaction	$H_2(g) \rightarrow 2H^+(aq) + 2e^-$	$H_2(g) + 2OH^-(aq) \rightarrow 2H_2O(l) + 2e^-$	$H_2(g) \rightarrow 2H^+(aq) + 2e^-$	$H_2(g) + CO_3^{2-} \rightarrow H_2O(g) + CO_2(g) + 2e^-$	$H_2(g) + O^{2-} \rightarrow H_2O(g) + 2e^-$
Cathode reaction	$½O_2(g) + 2H^+(aq) + 2e^- \rightarrow H_2O(l)$	$½O_2(g) + H_2O(l) + 2e^- \rightarrow 2OH^-(aq)$	$½O_2(g) + 2H^+(aq) + 2e^- \rightarrow H_2O(l)$	$½O_2(g) + CO_2(g) + 2e^- \rightarrow CO_3^{2-}$	$½O_2(g) + 2e^- \rightarrow O^{2-}$
Cell reaction	$H_2(g) + ½O_2(g) \rightarrow H_2O(l)$	$H_2(g) + ½O_2(g) \rightarrow H_2O(l)$	$H_2(g) + ½O_2(g) + CO_2 \rightarrow H_2O(l) + CO_2$	$H_2(g) + ½O_2(g) + CO_2(g) \rightarrow H_2O(g) + CO_2(g)$	$H_2(g) + ½O_2(g) \rightarrow H_2O(g)$
Conductive ions	H^+	OH^-	H^+	CO_3^{2-}	O^{2-}
Poisonous gas species	CO (50ppm per stack, reversible)	CO, CO_2, S, CH_4	CO (<0.5%) S (<50ppm)	S (<0.5ppm)	S (<1.0ppm)

Table 1.1. Comparison of different types of fuel cells.

1.2 Proton Exchange Membrane Fuel Cell (PEMFC)

The PEMFC have been actively developed for use in vehicles, portable electronics and combined heat and power (CHP) systems due to its simplicity, low temperature, high power density and quick start-up. Several recent pivotal innovations, including lowering Pt catalyst loading, introducing thin film electrodes, and balancing water transport has lowered the cost and prolonged the lifetime of fuel cells, thus making PEMFC more realistic. The PEMFC also allows

direct use of methanol without a fuel processor, called the direct methanol fuel cell (DMFC). The DMFC is seen as the leading candidate technology for the application of fuel cells to cameras, notebook computers, and other portable electronic applications.

1.2.1 Cell Components

A typical PEMFC unit within a cell stack contains the following components:

- The ion exchange membrane;
- An electrically conductive porous backing layer;
- An electrocatalyst (the electrodes) at the interface between the membrane and the backing layer;
- Cell interconnects and flow plates that deliver the fuel and oxidant to reactive site via flow channels and electrically connect the cells.

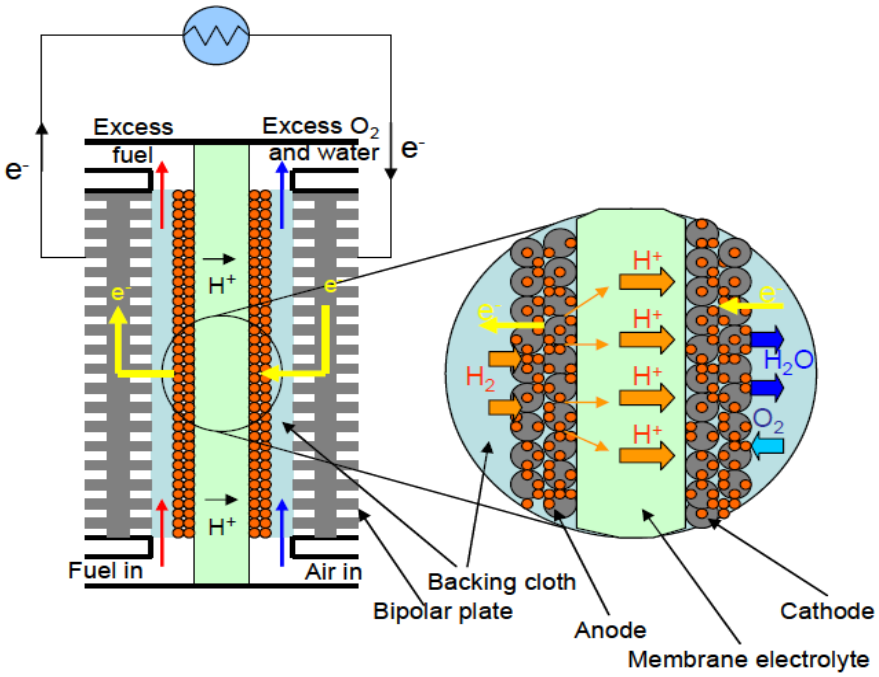

Figure1.1. The schematic illustration of a single PEMFC stack

Figure 1.1 is the schematic illustration of a unit cell in the PEMFC system. The PEMFC stack consist of a various number of unit cells in series connected by bipolar plates to achieve the required voltage. The electrodes and the ion exchange membrane is the key part of the PEMFC which is called as membrane electrode assembly (MEA). The MEA usually is not thicker than a few hundred micros, generating electric power at cell voltages around 0.7V and power densities up to 1W cm^{-2}. In the MEA, the membrane functions as an ionic conductor; at the same time, it provides a separation between the fuel and the oxidant. Electrons cannot pass through the membrane. The ionic groups in the polymer provide active sites for ionic conduction. The conductivity of the polymer is highly dependent on the bound and free water associated with those sites. The most common membrane is Nafion made by DuPont.

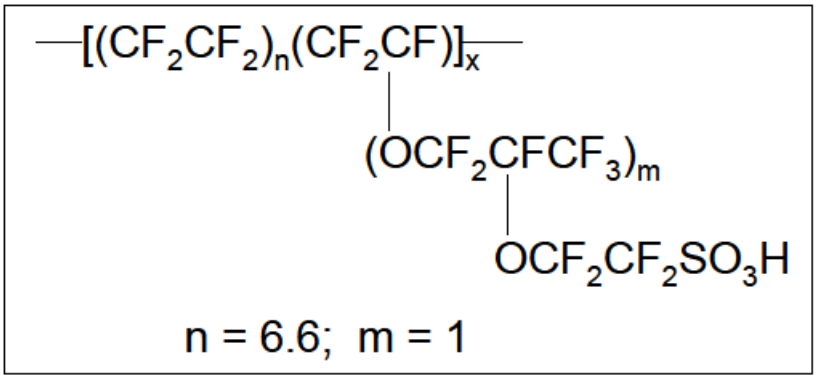

Figure1.2. Structure of Nafion® membrane from DuPont

As shown in the Figure1.2, Nafion consist of a strongly hydrophobic polytetrafluoroethylene (PTFE) backbone, which makes it inert to chemical attack. The side chain ending with sulphonic acid SO_3H is attached to the backbone with an oxygen atom through a process known as sulphonation. Indeed, the SO_3H group is ionically bonded which means the end of the side chain is actually SO_3^-. The interesting property of this kind of side chain is its

high hydrophilicity. Thus, the regions around the side chain can absorb large quantities of water. Within these hydrated regions, the protons are weakly attracted to the SO_3^- group, which explains how the Nafion film works as the conductor of proton. These groups preclude anion transport through the membrane.

The electrolyte membrane is sandwiched between two sheets of porous backing media, referred to as gas diffusion layer or current collectors. The functions of the backing layer are (1) act as a gas diffuser; (2) provide mechanical support; (3) provide an electrical pathway for electrons; and (4) channel product water away from the electrodes. The backing layer is typically carbon based, or may be in cloth form. The layer incorporates a hydrophobic material, such as PTFE. The function of the hydrophobic material is to prevent water pooling within the pore volume of the backing layer so that gases can freely contact the catalyst sites.

There are two sides of the membrane and between it and the backing layer are the catalyst layers. This catalyst layer, integral with its binder, forms the electrodes. The catalyst is platinum based for both the anode and the cathode. To promote hydrogen oxidation, the anode uses carbon supported pure platinum. In the case that the fuel contains CO impurity, an alloy of platinum and ruthenium is desired. For oxygen reduction, carbon supported platinum is used. Because of the expense of platinum catalyst, there have been numerous efforts to minimize the use of the platinum in the catalyst layer. The platinum particle size has been extensively optimized, and general agreement is that a ~3.5nm particle size on suitable carbon support is close to optima: the platinum mass specific activity is near optimal under these conditions. In parallel, there have been numerous efforts to substitute other materials to platinum. Due to the slow kinetics of oxygen reduction at the cathode[3,4], much higher platinum loading is required for the cathode

compared with the anode; therefore, low platinum loading cathode catalyst with higher activity is desirable[4]. For the oxygen reduction reaction, platinum alloy with 3*d* transition metals were reported to have higher catalytic activity than pure platinum particles, and carbon supported Pt_3Co particles are commercially available for cathode catalyst. But these alloys are usually rich in platinum. Among those efforts, platinum monolayer catalysts developed by Adzic's group over the past few years showed good activity for both anode and cathode, while decreasing the use of platinum to an ultimate minimum.

1.2.2 Thermodynamics and Electrochemical Kinetics

In a fuel cell the Gibbs free energy (ΔG) of an electrochemical reaction is converted into electrical energy in the form of an electric current. Thus the maximum electrical work (W_e) obtained in a fuel cell is equal to the change of the Gibbs free energy of the electrochemical reaction [5].

$$W_e=\Delta G=-n_eFE \tag{1.1}$$

Where n_e is the number of electrons transferred per mole of fuel and F is the Faradays constant and E is the potential difference across the electrodes. The same substitution is applied to the standard Gibbs free energy ($\Delta G°$) to define the standard potential, E^0.

$$\Delta G^0=-n_eFE^0 \tag{1.2}$$

For a general cell reaction:

$$\alpha A+\beta B=\gamma C+\delta D \tag{1.3}$$

The Gibbs free energy change of this cell reaction can be expressed as:

$$\Delta G = \Delta G^{\circ} + RT \ln \frac{[C]^{\gamma}[D]^{\delta}}{[A]^{\alpha}[B]^{\beta}} \tag{1.4}$$

where ΔG° is the standard Gibbs free energy; $[A]$, $[B]$, $[C]$ and $[D]$ are the concentration of species A, B, C and D respectively. Substituting equation (1.4) to (1.1) gives the Nernst's equation:

$$E = E^{\circ} + \frac{RT}{nF} \ln \frac{[C]^{\gamma}[D]^{\delta}}{[A]^{\alpha}[B]^{\beta}} \tag{1.5}$$

For the case of a H_2/O_2 PEM fuel cell, the overall reaction:

$$H_2 + \frac{1}{2} O_2 \rightarrow H_2O \tag{1.6}$$

Based on the Nernst equation, the ideal performance of this cell can be calculated as:

$$E = E^{\circ} - \frac{RT}{4F} \ln \frac{P_{H_2O}^2}{P_{H_2}^2 P_{O_2}} \tag{1.7}$$

where P is the gas pressure. Thus the ideal potential of H_2/O_2 PEM fuel cell is 1.23V with liquid water product, or 1.18V with gaseous water product.

1.2.3 Fuel Cell Performance and Voltage Losses

The thermodynamic equilibrium potential of a fuel cell can be described by the Nernst equation; but even the open circuit potential is lower than the Nernstian value because of the irreversible process. The deviation of the potential from the equilibrium value, which is called polarization or over potential, originates mainly from three sources: 1) activation polarization; 2) ohmic polarization; and 3) concentration polarization.

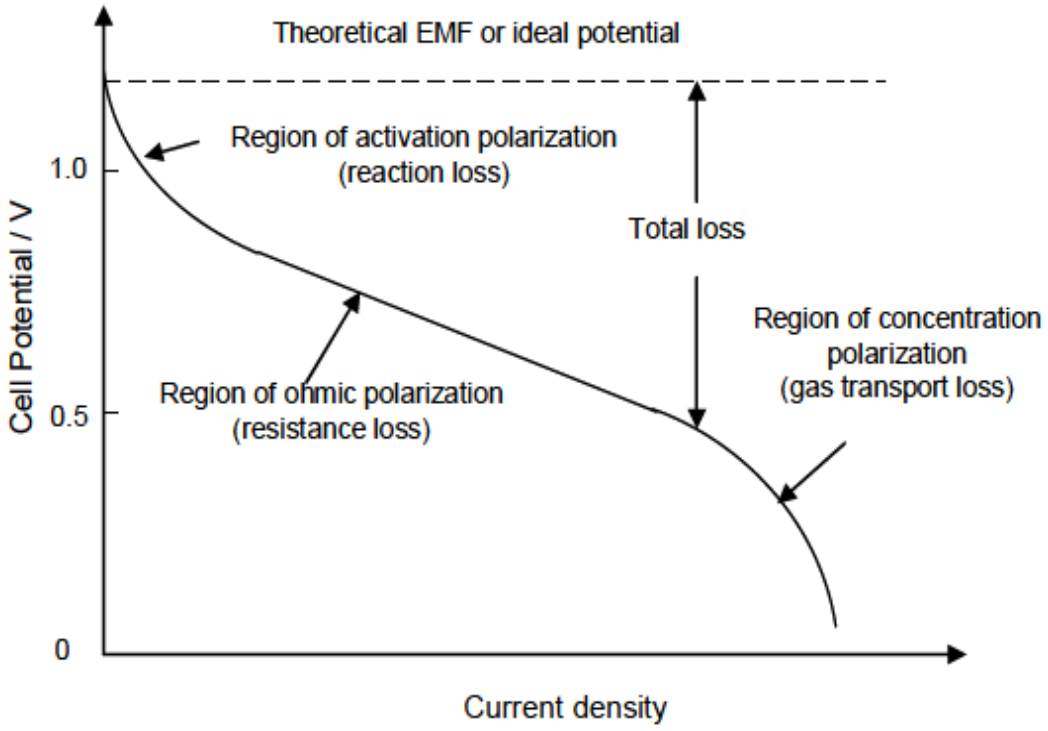

Figure1.3. A typical polarization curve of the PEMFC operating at 80°C

Activation polarization is caused by sluggish electrode kinetics; in other words, it is directly related to the electrochemical reaction rate. In order to decrease the activation losses, better catalysts need to be developed.

Ohmic losses occur because of the resistance to the ion flow in the electrolyte and resistance to the electron flow through the electrode. A thinner electrolyte with higher ion conductivity helps decreasing the ohmic resistance. Less separation of electrode catalyst and better contact between the backing layer and the bipolar plates are also important to reduce the ohmic loss.

As a reactant is consumed at the electrode, there is a potential loss due to the reactant concentration gradient between the bulk fluid and the electrode surface. Concentration polarization is primarily caused by slow diffusion of the reactant and product to and from electrochemical reaction site. The larger current density a fuel cell it provides, the larger concentration loss is produced.

If we define η as the losses, the overall voltage of the cell would be

$$E_{\text{cell}} = E - \eta_{\text{activation}} - \eta_{\text{ohm}} - \eta_{\text{concentration}} \qquad (1.8)$$

As indicated in figure 1.3, when current density is small, the potential is near equilibrium value, where the activation polarization is the major loss. When the current density is increased to a certain range, ohmic polarization together with activation polarization dominates the loss. At relatively high current density, the concentration polarization is another significant loss. There is a limiting current density for a cell which is determined by the diffusion limit. In order to get a

practically useful power density and reasonable efficiency, a real PEM fuel cell works at a potential of around 0.7V.

1.2.4 Fuel Types

In the PEMFC, not only pure hydrogen but also some liquid fuels can be fed to the anode as a fuel. Molecular hydrogen is currently receiving the most attention as the starting point in the development of fuel cell technology [6]. The most important aspect of hydrogen is that the kinetics of hydrogen oxidation reaction (HOR) is very fast. The reaction mechanism of HOR has been extensively studied [7, 8]. There are three elementary steps for the HOR on a Pt electrode in acid media [9-11].

$$2\mathrm{Pt} + \mathrm{H_2} \rightarrow 2\mathrm{Pt} - \mathrm{H} \qquad \text{Tafel reaction} \tag{1.9}$$

$$\mathrm{Pt} + \mathrm{H_2} \rightarrow \mathrm{Pt} - \mathrm{H} + \mathrm{H^+} + e^- \qquad \text{Heyrovsky reaction} \tag{1.10}$$

$$\mathrm{Pt} - \mathrm{H} \rightarrow \mathrm{Pt} + \mathrm{H^+} + e^- \qquad \text{Volmer reaction} \tag{1.11}$$

With an overall HOR reaction:

$$\mathrm{H_2} \rightarrow 2\mathrm{H^+} + 2e^- \tag{1.12}$$

Based on these reactions, one can find there are two pathways for HOR. In the Tafel-Volmer pathway, the dissociative adsorption of a H_2 molecule is followed by two separate one-electron transfer steps from adsorbed H atom. While in the Heyrovsky-Volmer pathway, the hydrogen is absorbed on the Pt simultaneously with a one-electron oxidation, followed by

another one-electron oxidation of the adsorbed H atom. Recent results reveal that both reaction pathways are involved so that the commonly used Butler-Volmer equation is inappropriate for describing the kinetics of the HOR. Wang et al. developed a dual-pathway kinetic equation which showed that a fast, inversed exponential increase of kinetic current at small overpotential occur through the Tafel-Volmer pathway[12], while a much more gradual current rise in the overpotential region larger than 50mV involves the Heyrovsky-Volmer pathway.

The production of H_2 is one of the key issues of hydrogen economy. If H_2 is generated by reforming methanol, ethanol or natural gas, a very small concentration of CO in fuel causes a significant drop in cell efficiency [13]. CO-tolerant electrocatalysts have been searched to overcome the negative effects of CO poisoning. Generally, these electrocatalysts are combinations of platinum and oxophilic elements, such as ruthenium, tin, molybdenum, osmium, etc., in binary, ternary, or quaternary alloys [14-18]. The alternative way to increase CO tolerance of the electrocatalysts is to deposit sub-monolayer of Pt on Ru nanoparticles. One of the main advantages of the sub-monolayer Pt electrocatalysis is to reduce the amount of Pt used by more than 10 times in comparison with commercial Pt alloy electrocatalysts [19-21].

Even though H_2 is the ideal fuel for PEMFC, several big challenges still remain arising from the production, transportation, distribution and storage of gaseous hydrogen [6]. Liquid fuels (methanol, ethanol, dimethyl ether) have no such problems, but on the other hand these fuels have their own technological barriers thus preventing them from commercialization. Methanol and ethanol rapidly oxidize at the Pt cathode [22-23], which results in a mixed potential lowering the cells efficiency, thus requiring better tolerance cathode catalyst. On the other hand, their oxidation at anodes is slow and incomplete.

1.3 Cathode Electrocatalyst of the PEMFC

The oxygen reduction reaction (ORR) is a very complicated process consisting of a number of possible reactions and through various pathways [4], which is discussed in more detail in the next section. The thermodynamic potentials for the reactions that proceed in acid solution are shown below:

$$O_2 + 4H^+ + 4e^- \rightarrow 2H_2O \quad E^0 = 1.229\,V \tag{1.13}$$

$$O_2 + 2H^+ + 2e^- \rightarrow H_2O_2 \quad E^0 = 0.695\,V \tag{1.14}$$

$$O_2 + H^+ + e^- \rightarrow HO_2 \quad E^0 = -0.046\,V \tag{1.15}$$

Therefore, the catalyst capable of , the ORR with exchange of four electrons (reaction 1.13) is a necessity because it offers the highest cell voltage, i.e. the most efficient energy conversion. However, even the best catalyst for ORR (Pt) the reaction requires large overpotential, which is 0.3-0.4V below the E^0 [24]. Therefore great effort has been made to develop better catalyst.

1.3.1 Platinum Catalysts

Carbon supported Pt nanoparticles (Pt/C) allow a much higher metal dispersion and hence more surface area than Pt blacks. However the ORR activity of Pt/C is particle size dependent. The effect of particle size is known from the specific adsorption of anions on different Pt faces, the distribution of which changes with particle size [25]. Some researchers

ascribe this to the particle size induced changes in the adsorption of OH_{ads}, which is believed to act as the catalytic poison [26]. It was found that the smaller the particle size, the lower the potential at the point of zero charge (pzc) of Pt/C [27].The pzc shifts 35mV negatively by decreasing the particle size of Pt/C from 30 to 1nm. That is, more OH_{ads} on the Pt surface at the same potential by increasing the Pt dispersion. The particle effect implies that the Pt particle cannot be extremely small. The Pt nanoparticles with a size at 3-4 nm have the highest mass activity. This also implies that the development of more active Pt alloys is the only way to achieve higher mass activity.

1.3.2 Platinum Alloy Catalysts

The intrinsic activity of Pt was found to be enhanced up to 3–fold by alloying an inexpensive non-noble metal (such as Fe, Ni, Co, Cr etc.) forming bimetallic surfaces. In the PEMFC system, an improvement of 20-40 mV compared with Pt/C has been demonstrated using Pt-alloys/C catalyst [28]. Numerous studies have been conducted to understand the origins of the enhancement.

Due to the slow kinetics of oxygen reduction at the cathode[4, 26], much more platinum loading is required for the cathode compared with the anode; therefore, low platinum loading cathode catalyst with higher activity is desirable[4]. For the oxygen reduction reaction, platinum alloy with 3d transition metals were reported to have higher catalytic activity than pure platinum particles, and carbon supported Pt_3Co particles are commercially available for cathode catalyst. But these alloys are usually rich in platinum.

1.3.3 Non-Pt Alloy Catalysts

Another way to lower the cost of the catalyst is alloying non-noble metals with other noble metals (Pd, Ru, Ir, and Au), among which only Pd based alloys (Pd-Co, Pd-Fe, Pd-Au, Pd-Ti) [29-32] show high ORR activity comparable to that of commercial Pt/C. Besides high activity, another advantage of Pd alloys is that they have excellent methanol tolerance, leading them to be promising candidates for cathode material in DMFC. However further improvement in the activity and stability of Pd alloy electrocatalyst is required to meet the industry standard.

A different class of non-Pt catalyst consists of transition metal ion, typically Fe and Co, stabilized by several nitrogen atoms forming an aromatic or graphite like carbon structure [33-36]. This approach was demonstrated to modify the carbon supported M–Nx/C catalyst materials, increasing the concentration of available ORR active sites. These structural transformations are a subject of extensive debate, where at high temperatures the atomic configuration of the macrocycle compounds was found to partially or completely decompose. These conflicting reports can most likely be attributed to differences in the synthesis procedures (i.e. type of macrocycle precursor, pyrolysis temperature and duration) and the nature and sensitivity of the characterization techniques utilized. As in this type of catalyst no noble metal is used, the challenge to maintain its stability and activity holds true. The ORR activity of non-noble catalyst needs to be less than $1/10^{th}$ of that of Pt/C, but the currently reported catalysts are far away from the target. Furthermore, most of the product of the ORR on non-noble catalyst was found to be H_2O_2 which attacks the MEAs, accelerating the degradation of the solid electrolyte and the catalyst itself.

1.3.4 Core-shell supported Platinum Catalysts

The creation of core-shell nanoparticles has in recent years developed into an increasingly important research area at the frontier of advanced materials chemistry [37, 38-40]. In general, core-shell catalysts consist of metal core and another metal shell nanoparticle. In electrocatalysis, the particles with a Pt monolayer shell supported on suitable metal core were first used as electrocatalysts for ORR. These electrocatalysts have a very high activity and an ultra-low Pt content that promises to alleviate the problems associated with ORR. Platinum is deposited in a monolayer amount on the surfaces of carbon-supported non-noble metal/noble metal core-shell nanoparticles by galvanic displacement of a Cu monolayer formed by under potential deposition (upd) with Pt. Using non-noble metals for the cores facilitates a further reduction of the content of the noble metal in the ORR electrocatalysts. In addition, by properly selecting the noble-metal shell, the activity of the Pt monolayer can be heightened through electronic and/or geometric effects. The choice of the metals constituting the substrate for the Pt monolayer is based on the segregation properties of the two metals, as well as their electronic and strain-inducing effects on the Pt monolayer. It is well known that the chemical composition at the surface of an alloy may differ from the composition in the bulk; that is, one of the alloy components may enrich the surface region. This phenomenon, known as surface segregation, is of vital importance in all of surface chemistry. At elevated temperatures the atoms of some noble metal tend to segregate to the nanoparticle surface.

The noble-metal shell in the core-shell nanoparticle has two roles. First, it protects the non-noble core from contacting the acid electrolyte, i.e. it prevents its dissolution. Second, the proper shell can improve the catalytic properties of a Pt monolayer by affecting its electronic properties and/or by inducing strain in the monolayer, which increases its activity. A strong

surface segregation of the noble metal component is the key feature of these systems. The modification of electronic and geometrical structures of Pt monolayer by the substrates results in a catalytic activity different with that of pure Pt. Density functional theory (DFT) calculations shows that the binding energies and reactivity of small atom or molecule adsorption on strained surfaces and metal overlayers correlate well with the position of d-band center of the surface atoms. The ORR activity strongly depends on the d-band center of Pt monolayer [37]. The other factor that contributes to the modification of the surface Pt properties in the bimetallic systems is the electronic interaction between the two metals. This factor, also termed ligand effect [41] arises due to the presence of other metals around a metal atom changing its electronic environment, giving rise to modifications of its electronic structure and consequently, its chemical properties. Due to different adsorption properties of the substrate and the Pt monolayer, the adsorbate on the substrate metal will change the electronic environment of Pt surface and consequently, change the electrocatalytic activity of the Pt atoms.

1.4 Reaction Mechanisms of the ORR

1.4.1 Oxygen reduction Reaction (ORR) Basics

The electrocatalysis of the ORR has been extensively studied because of its importance for energy conversion, corrosion and physiological processes [4, 42-43]. Particularly, ORR plays a key role to achieving high efficiency in low temperature fuel cells. In spite of numerous studies, ORR is still a challenge for electrochemists because of its complexity and need for better electrocatalyst.

The overall reaction of the ORR (reaction 1.13), involves multiple intermediates, electron and proton transfers, and reaction steps [4]. In aqueous solutions, oxygen reduction is considered to occur through two distinguished pathways: a direct four-electron reduction involving dissociation of the oxygen molecule and its subsequent reduction to water (in acid solutions) or OH^- (in alkaline solutions), and a peroxide pathway involving the formation of H_2O_2, which can be a final product or an intermediate whose further reduction leads to water or OH^- formation.

In acid solutions, the direct four-electron pathway was shown as reaction 1.13, while in alkaline solutions it is

$$O_2 + 2H_2O + 4e^- \rightarrow 4OH^- \quad E^0 = 0.401\,V \tag{1.16}$$

In acid solution, the peroxide pathway follows reaction 1.14. The produced H_2O_2 can be further reduced or decompose leading to a four-electron reduction, via either reaction:

$$H_2O_2 + 2H^+ + 2e^- \rightarrow 2H_2O \quad E^0 = 1.77\,V \tag{1.17}$$

or

$$2H_2O_2 \rightarrow 2H_2O + O_2 \tag{1.18}$$

In alkaline solutions, the formation of H_2O_2

$$O_2 + H_2O + 2e^- \rightarrow HO_2^- + OH^- \quad E^0 = -0.065\,V \tag{1.19}$$

is followed by either further reduction reaction

$$HO_2^- + H_2O + 2e^- \rightarrow 3OH^- \quad E^0 = 0.867\,V \tag{1.20}$$

or by decomposition reaction

$$2HO_2^- \rightarrow 2OH^- + O_2 \tag{1.21}$$

In fuel cells, it is desired to achieve a four-electron reduction in order to obtain maximum efficiency and to avoid corrosion by peroxide. It was found that the four-electron reduction only occurs on Pt and its alloys. On other surfaces, peroxide is the final product. Under certain conditions, superoxide (O_2^-) anion can also exist in the solution phase besides peroxide.

In the oxygen reduction, electrons are transferred from the metal to the antibonding orbitals of O_2, which decreases the bond order and elongates the O-O bond, subsequently decreases the vibrational frequency of the O-O stretching. However, the adsorption sites and the configuration for the O_2 adsorption on electrode surface are unclear. There are three possible O_2 absorption models on metal surfaces, named Griffith, Pauling and Yeager model [4]. O_2 is adsorbed on a single substrate atom with two bonds in the Griffith model, and through a single bond in the Pauling model (end-on configuration), whereas in Yeager model, O_2 is adsorbed on two sites with two bonds (bridge configuration). The two-electron and four-electron reduction may involve the Pauling and Yeager model respectively.

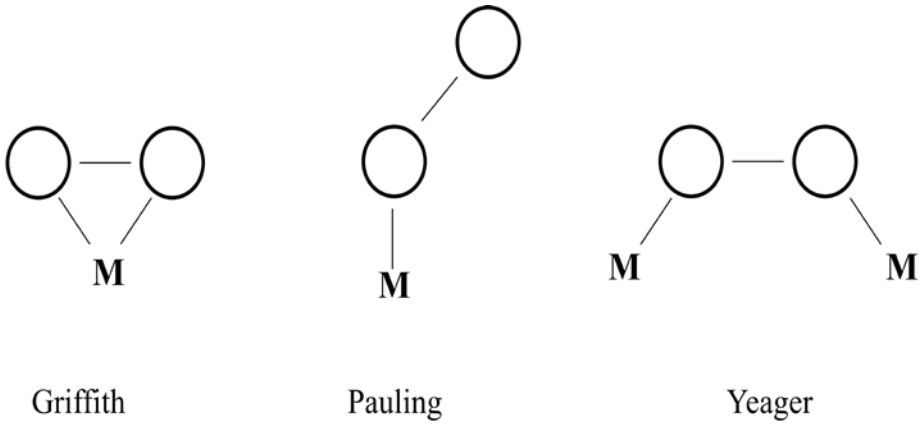

Figure 1.4. Possible adsorption configurations of O_2 on Pt surfaces

1.4.2 Reaction Pathways

Rotating ring-disk electrode (RRDE) technique was first applied to the study of the ORR by Mueller and Nekrasov [44] and still this principle is widely used for kinetic measurements and detection of some reaction intermediates. A significant amount of work has been conducted to try to gain more information by analyzing the RRDE response with rotation rate and disk potential. Since the first description by Damjanovic et.al [45, 46], several reaction schemes, including Wroblowa et.al [47], Bagotskii et.al [48, 49] and Anastasijevic et.al [50] have been proposed based on RRDE data, among which Anastasijevic's is the most general one.

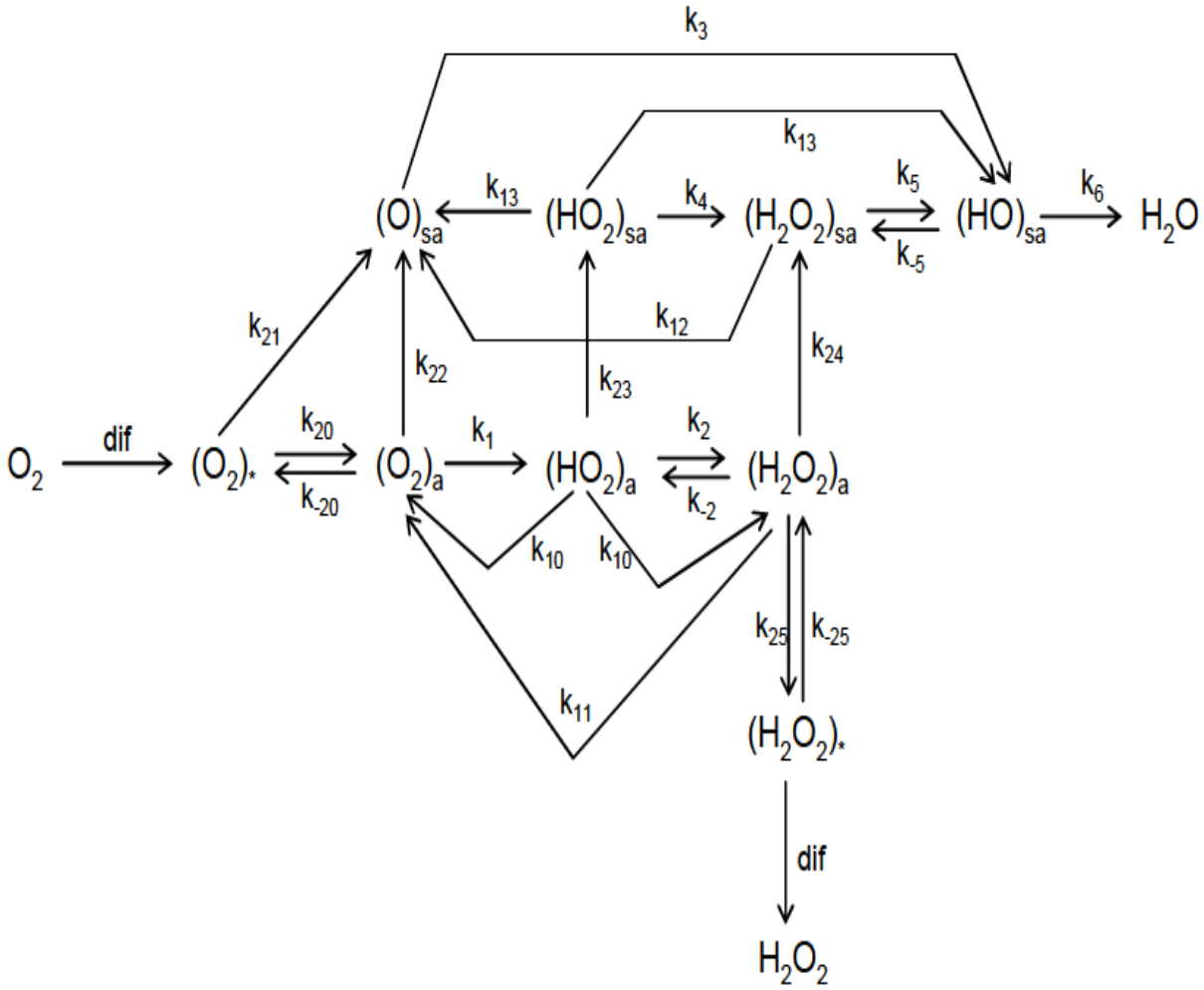

Figure 1.5. Anastasijevic et.al scheme for ORR

Figure 1.5 shows the Anastasijevic et.al scheme, which includes nearly all the possible intermediates. The original scheme has been written for alkaline solutions, but it is transformed into an analogous scheme here for acid solution [51], in order to keep consistence with previous schemes discussed above. The k_i are overall rate constants for the i^{th} step, and the subscripts a, sa, and * denote adsorbed, strongly adsorbed, and in the solution adjacent to the electrode surface, respectively; without a subscript denotes in bulk solution. The scheme is the most

comprehensive scheme proposed so far and, as before, consists of two major paths by which ORR can take place, i.e., the O_2 can be electrochemically reduced either directly to water without formation of the intermediate hydrogen peroxide or with the intermediate hydrogen peroxide. The adsorbed hydrogen peroxide (H_2O_2) can be either reduced to water, oxidized back to O_2, decomposed on the electrode surface into O_2 and H_2O, or desorbed and diffuse into the bulk of the solution. Two main features of this scheme make it distinct from previous ones is:

(1) The superoxide species (HO_2) can explicitly be an intermediate and

(2) Weakly adsorbed intermediates from the series path can undergo surface diffusion and form their strongly bound counterparts in the direct path.

Although it is impossible to obtain all of the rate constants in the reaction scheme (Fig. 1.5), one can draw some qualitative conclusions and obtain some information as to the pathway of the reaction by the careful examination of experimental data [50]. The equations relating the ratio of currents at the disk (I_D) and the ring (I_R) to the electrode rotation rate are as follows:

$$\frac{NI_D}{I_R} = 2\left(1 + A_0 + A_1 k_{-25}/Z\omega^{1/2}\right)/n_R \tag{1.22}$$

where A_0 and A_1 are dimensionless functions of the rate constants. The intercepts and slopes from the NI_D / I_R vs. $\omega^{-1/2}$ plots are related by the equation

$$J = 2(1 + A_3)n_R + ZS/k_{-25} \tag{1.23}$$

where J and S are the ordinate intercepts and slopes at various potentials, and A_3 is a dimensionless function of rate constants. Anastasijevic et al. [50] got some conclusions after careful examinations of these equations: (1) Linearity of the NI_D / I_R vs. $\omega^{-1/2}$ plot is a sufficient

proof for a first-order reaction in its all stages; (2) When the equilibrium of adsorption/desorption of H_2O_2 does not exist, $S = 0$; (3) A non-linearity of $J - S$ plot occurs when an interactive pathway involved, in which diffusion of species from series path into a direct path takes place. (4) Linearity of $J - S$ plot with the J-axes intercept $J' > 2 / n_R$ is a characteristic of a true parallel pathway. In such case, the ratio of the direct pathway to the series pathway can be evaluated. These criteria provided a way to obtain the most extendedly information of ORR that the rotating disk ring technique can provide. Further insight into the mechanism of the ORR will highly depend on the spectroscopic methods with the ability to detect intermediates associated with the reaction.

Due to the considerable non-uniformity in the terminology for the reaction schemes of O_2 reduction, Adzic et.al [4] proposed a clearer standard to classify the ORR pathways. It is defined as:

i) a “direct” four-electron reduction to H_2O (in acids) or to OH^- (in alkaline) without hydrogen peroxide detected on the ring;

ii) a two-electron pathway involving reduction to hydrogen peroxide;

iii) a “series” pathway with two- and four-electron reduction. The case of only four-electron reduction without hydrogen peroxide detected on the ring is indistinguishable from a “direct” four-electron reduction;

iv) a “parallel” pathway that is a combination of (i), (ii), and (iii); and

v) an “interactive” pathway in which diffusion of species from a “series” path into a “direct” path is possible.

1.4.3 ORR on Pt surface

It is widely accepted that the oxygen electro reduction on platinum occurs through parallel reaction pathway with predominately direct four-electron reduction [4, 52-55]. However, the details about the mechanism remain elusive. The overall ORR is a multistep process involving four-electron transfers during which bonds are broken and formed. It is still not clear whether the process starts from the oxygen molecule dissociation on Pt electrode, which is followed by electron and proton transfer, or whether the first reduction step happens before O-O bond cleavage. To answer this question, the information about the site and the configuration of O_2 adsorbed on a Pt electrode surface is critical. Three plausible types of O_2 adsorption were proposed by earlier researchers, viz., Griffith (on-top, double bond), Pauling (on-top, single bond), and "bridge", see figure 1.4.

Oxygen adsorption on clean metal surfaces at the metal-gas interface has been the subject of numerous studies in order to establish the nature of the chemisorption, the bond strength, and the structure of the absorbed layer. Oxygen adsorbs in molecular form at low temperatures, while dissociative adsorption on platinum group metals occurs at temperatures in the range 150~300K. The system O_2-Pt (111) was investigated with a particularly broad variety of methods. A recent study confirmed the existence of the three types oxygen adsorbates on Pt(111), i.e., physisorbed O_2, at about 25K, chemisorbed, at 90-135K, and an atomic phase above 150K[56]. The chemisorption of molecular oxygen on a Pt (111) surface was recently examined using tight-binding extended Hückel calculations [57]. It was found that chemisorption of O_2 appears to be more favorable at the 2-fold-bridge site than on on-top or on 3-fold sites. The stabilization is due to the better overlap of the O_2 $2\sigma_u$ orbital with the Pt surface.

Damjanovic et al [58, 59] proposed that the first step is an electron transfer to the O_2 molecule.

$$O_2 + e^- \rightarrow O_2^- \tag{1.24}$$

This step is the rate-determining step, which is accompanied by or followed by a fast proton transfer. This proposal is supported by the results of Sepa et al. [60, 61], based on their experiments on ORR at Pt surface in electrolytes with various pH. It is also supported by recent results of Markovic et al. [62, 63], based on their ORR experiments on single crystal electrodes.

In a recent study by Wang et al [64], the kinetic parameters and anion adsorption effect for ORR on Pt(111) surface was investigated in sulfuric acid and perchloric acid. By using the same set of kinetic parameters and correlating the kinetic equation with the anion adsorption coverage, the authors were able to fit polarization curves of ORR on Pt(111) in both sulfuric acid and perchloric acid, see fig. 1.6. In these two acids, the anion adsorbates on Pt(111) at ORR region are mainly (bi)sulfate and hydroxyl species, respectively. The kinetics of the reaction was found to be 4-electron reduction with the first charge transfer as the rate determining step in both acids. Oxygen was believed to be adsorbed on dual Pt sites. Besides the geometric site blocking effect, the anion adsorption was also found to have an adverse electronic effect on ORR kinetics.

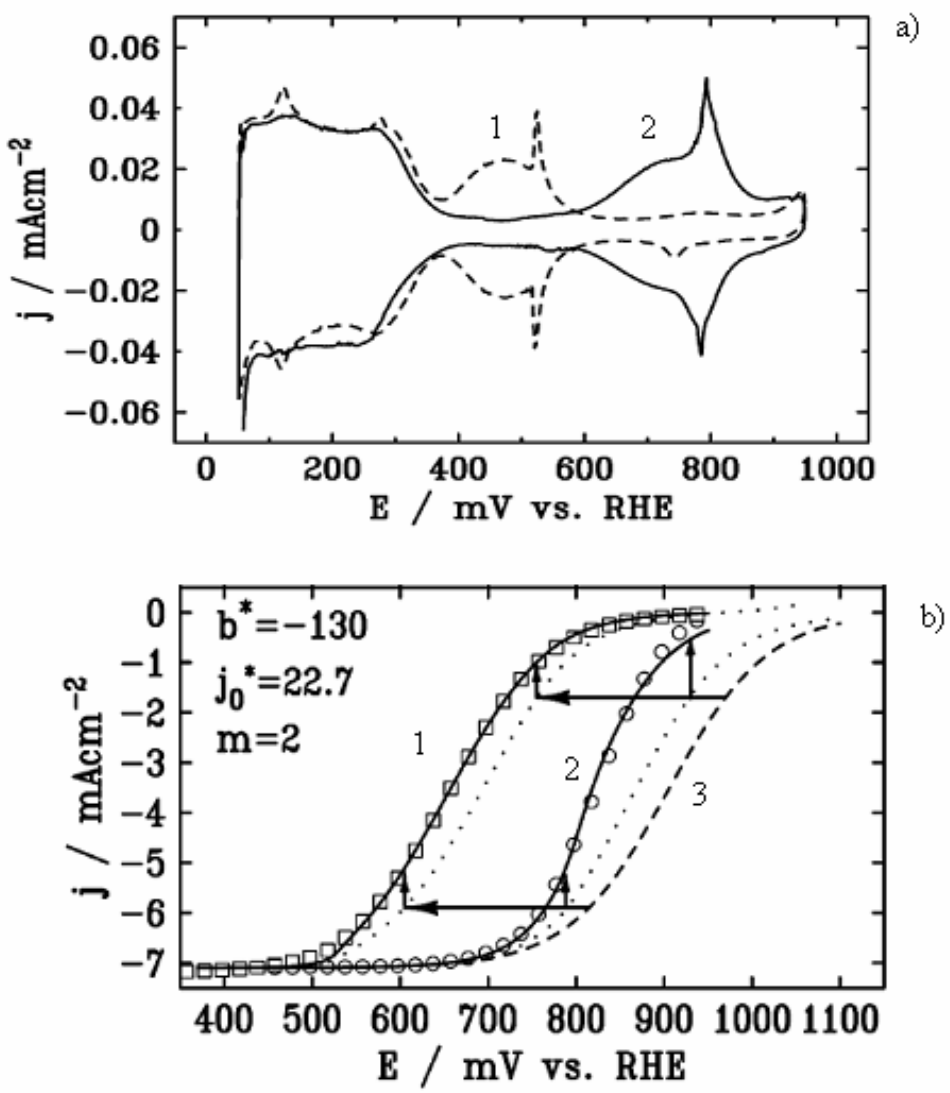

Figure1.6 (a) 1, 2: Pt(111) CV's in 0.05M H_2SO_4 and in 0.1M $HClO_4$, respectively, scan rate 50mV/s; (b) ORR polarization curves at 2500rpm on Pt(111) in H_2SO_4 (1), $HClO_4$ (2) and in an ideal electrolyte without anion adsorption (3), respectively. From J. X. Wang, N. M. Markovic, and R.R. Adzic, J. Phys. Chem. B 2004, 108, 4127-4133

The second view was advocated by Yeager and coworkers [65-67], who proposed that the most likely mechanism of the four electron oxygen reduction on Pt involves dissociative chemisorption of the O_2 molecule on a platinum surface. This probably occurs with simultaneous charge transfer. From the experimental point of view, there is evidence of dissociative adsorption

of O_2 on platinum at temperatures in the range 150-300K [68-70], but there is no evidence for the direct cleavage of O-O bond at the electrochemical interface.

Now it is well established the reaction rates of oxygen reduction on different low index Pt surfaces are structure sensitive, due to structure sensitive adsorption of intermediates (O_2ads and OOH_{ads}) and spectator species (OH_{ads}). The adsorption of OH is probably the most important in the process. In 0.05M H_2SO_4, the ORR rate increases in the sequence Pt(111) < Pt(100) < Pt(110)[71]. An exceptionally large deactivation is observed on Pt(111) surface due to the blocking and electronic effect of strongly adsorbing (bi)sulfate anion. In perchloric acid solution, the variation of activity at 0.8~0.9V is relatively small between the three low index surfaces, with the activity increasing in the order Pt(100) < Pt(110) ≈ Pt(111)[62]. A similar structural sensitivity is observed in 0.1M KOH. In the potential range where oxygen reduction is under combined kinetic-diffusion control (E > 0.75V), the activity increases in the sequence Pt(100) < Pt(110) < Pt(111)[72]. The decrease of Pt(100) surface activity is related to high affinity of (100) sites for the hydroxyl adsorption, leading to a lack of active centers for O_2 adsorption because the Pt(100) surface is highly covered by OH_{ads}. Markovic et al. suggested O_2 reduction should be proportional to the part of the surface not covered by hydroxyl species $(1- \Theta_{OH})$[63]. Nørskov et al.[73] used the DFT method to calculate the stability of reaction intermediates of electrochemical processes of oxygen reduction on Pt(111) surface, based on their Gibbs free energy, see Fig. 1.7. Adsorbed oxygen and hydroxyl are found to be very stable intermediates at potentials close to equilibrium, which is believed to be the origin of the O_2 reduction overpotential for Pt, and effectively prevents reaching 1.23V of open circuit potential. The calculated rate constants for the activated proton/electron transfer agree with the observed kinetics. These calculations also showed Pt has the smallest overpotential over other metals.

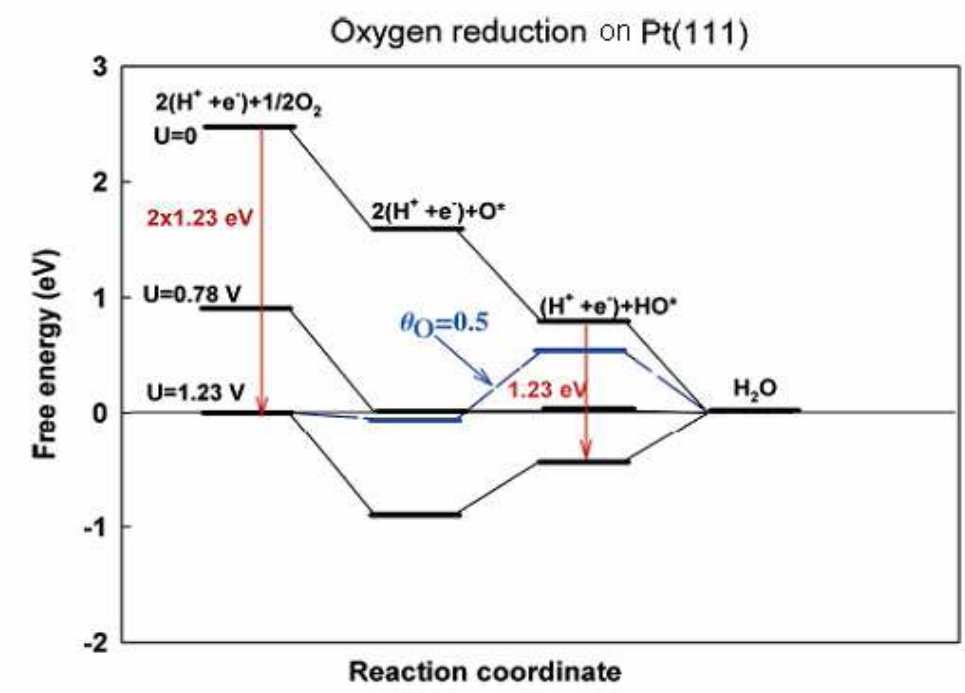

Figure1.7. Free-energy diagram for oxygen reduction on Pt(111) based on the free energies. Results for low oxygen coverage are shown at zero cell potential (U = 0), at the equilibrium potential (U = 1.23 V), and at the highest potential (U = 0.78 V), where all reaction steps are exothermic. For U= 1.23 V, the free-energy diagram for the case of an oxygen coverage of 1/2 is included.
From J.K. Nørskov et al. J. Phys. Chem. B 2004, 108, 17886-17892

As the best catalyst for O_2 reduction, platinum is on the top of several volcano plots in the literature. Further enhancement of its activity is an interesting topic. Alloying of Pt with the first row transition metal such as V, Cr, Si, or Ti produced significant enhancement of the Pt electrocatalytic activity for oxygen reduction, which has been explained by a more favorable Pt-Pt distance for O_2 adsorption due to contraction of Pt-Pt bond in the alloy [74]. For the review, see the article by Mukerjee [75]. Recent investigations on five binary carbon-supported Pt alloy electrocatalysts (Pt/Cr, Pt/Mn, Pt/Fe, Pt/Co, Pt/Ni) using in-situ X-ray absorption spectroscopy

(XAS) show that the alloys have higher Pt 5d-orbital vacancies and shorter Pt-Pt bond distances[76], the so called electronic effect and geometrical effect, respectively. These results also imply that alloying inhibits chemisorption of OH on the Pt surface at potentials above 0.8V. Another factor that becomes important for oxygen reduction on highly dispersed electrocatalyst particles is the influence of the particle size on reduction kinetics. As the electrocatalyst particle becomes smaller, a large fraction of total number of atoms in the particle is associated with surface sites, and the properties of these surface atoms may differ significantly from those of surface atoms in bulk samples. The review of this topic was given by Knoshita [77].

1.5 THE SUBJECT OF RESEARCH IN THIS DISSERTATION

1.5.1 Study of Ni-Ir core-shell structure

Nanostructured core-shell materials are becoming increasingly attractive for environmentally friendly energy conversion devices because they often exhibit better physical and chemical properties than their single-component counterparts and alloys. During the last decade, immense efforts have been made to fabricate core-shell materials with tailored structural, optical, and catalytic surface properties [78-83].

The choice of metals for the shell and core of bimetallic nanoparticles is based on the segregation properties of the two metals [84, 85], as well as their electronic and strain-inducing effects [86, 87]. The chemical composition at the surface of an alloy may differ from that in the bulk; that is, one of the components of the alloy may be enriched in the surface region. At elevated temperatures, the atoms of some noble metals tend to segregate to the surface; [88, 89] the formation of a complete noble metal shell can protect the non-noble-metal core from oxidation or dissolution. Therefore, the durability of the core-shell nanoparticles depends greatly on the integrity of the shell's structure.

Carbon supported IrNi core-shell nanoparticles were synthesized by chemical reduction and subsequent thermal annealing. The formation of Ir shells on IrNi solid solution alloy cores was verified by various experimental methods. The EXAFS analysis is consistent with the model wherein the IrNi nanoparticles are composed of two-layer Ir shells and IrNi alloy cores. *In situ* XAS revealed that the Ir shell completely protects Ni atoms in the cores from oxidation or dissolution in an acid electrolyte under elevated potentials. The formation of Ir shell during annealing in H_2 atmosphere is monitored by time-resolved synchrotron XRD measurements, coupled with Rietveld refinement analyses.

1.5.2 Designing Novel electrocatalyst for ORR

As discussed in previous sections, the commercialization of PEM fuel cells is encountering a few troubles. The slow kinetics of electrocatalytic oxygen reduction and the high loading of Pt of the cathode material are among those major ones [90]. Further increasing the fuel cell efficiency and reducing the cost will highly depend on availability of better electrocatalysts with decreased Pt content and increased activity [3-4, 42]. To alleviate these impediments, Adzic and coworkers developed a new approach to designing the low-Pt electrocatalysts for the cathode[19-20, 29-30] and for the anode[21, 91]. This approach involves depositing a sub-monolayer Pt or monolayer Pt on suitable metal or metal alloy substrates of carbon-supported metal nanoparticles. Two deposition methods developed by the same group facilitated the application of this new approach. One is electroless or spontaneous deposition of a submonolayer Pt on ruthenium surface[19, 92]; the other involves a red-ox replacement of monolayer Cu by Pt. Cu is deposited on suitable substrate under UPD conditions[91, 93]. Both methods produce Pt deposits in which all Pt atoms can be involved in the catalytic reaction. Consequently, Pt loading can be greatly reduced compared with other catalysts.

The catalytic properties of bimetallic surfaces consisting of metal monolayers on single-crystal metal surfaces have been extensively studied in ultra-high vacuum systems [94] and to a lesser extent, in electrochemical ones [95-97]. In many cases, the formation of a surface metal-metal bond significantly changed the electronic properties of the metal overlayers, and pronounced differences were observed in the reactivity of some transition metal monolayers on various substrates [94].

Norskov and co-workers recently proposed a new model to explain the adsorption properties of simple atoms and molecules on transition metal surfaces [86, 98]. In this model,

instead of the density of states at Fermi level or the number of d-holes, the average energy of the whole d-band (called d-band center ε_d) is used to explain the reactivity of the adsorption sites on the surface. Density functional theory (DFT) calculations showed that the binding energies and reactivity of small atom or molecule adsorption on strained surfaces and metal overlayers correlate well with the position of ε_d of surface atoms [99], in accord with data from numerous experimental studies [85, 100-101].

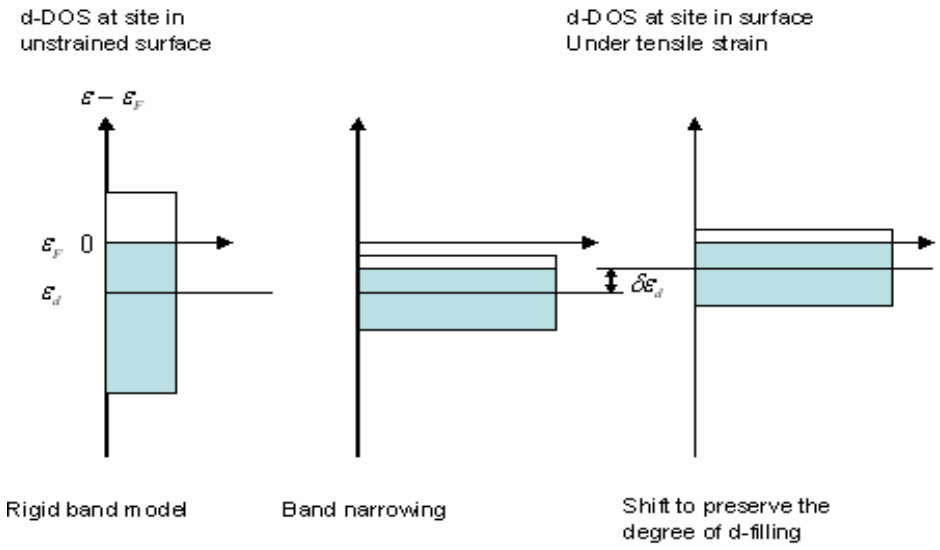

Figure1.8. Illustration of the effect of tensile strain on the d-band center increasing the lattice constant shrinks the band width, and in order to keep the number of d-electrons fixed, the d-states have to move up in energy.
From B. Hammer and J. K. Nørskov, Adv. Catal. 45, 71 (2000).

When this model is applied to a Pt monolayer deposit on a transition metal substrate, there are two critical factors that contribute to the modification of ε_d of the Pt atoms. First, the surface bond lengths are typically different from those of bulk Pt metal. This gives rise to

changes in orbital overlap due to strain effect and modifies the electronic structure of the metal[87]. According to these arguments, when the surface atoms are subjected to tensile strain, the d-orbital overlap is decreased, resulting in a sharpening of the d-band and an up shift of the d-band center (see Fig 1.8), which indicates a stronger adsorption energy. On the other hand, when the surface atoms are under compressive strain, the d-orbital overlaps are increased, resulting in a broadening of the d-band and a lowering of its average energy. Correspondingly, the adsorption energies of simple adsorbate are expected to decrease compared to those of bulk Pt. The second factor that contributes to the modification of the surface Pt properties in the bimetallic systems is the electronic interaction between the two metals. This factor, also termed ligand effect [41, 102], arises due to the presence of other metals around a metal atom changes its electronic environment, giving rise to modifications of its electronic structure and consequently, its chemical properties.

The above discussions imply that it is theoretically possible to modify the electronic properties of the monolayer Pt atoms toward desirable direction. Recently, Zhang et al [37, 93] found that if suitable substrate metal is selected, monolayer Pt electrocatalysts can have better electrocatalytic activity than bulk Pt. For Pt monolayer atoms, there are two ways to further refine its activity. The first is discussed above, i.e., by using different substrates, to modify the electronic properties of Pt atoms through geometric and electronic or ligand effects resulted from the interaction between Pt and the substrate metal; the second is to modify the Pt monolayer, by adding another metal to form a mixed Pt-metal monolayer. Due to different adsorption properties of the two metals, the adsorbate on the other metal will change the electronic environment of Pt surface and consequently, change the electrocatalytic activity of the Pt atoms.

In this thesis, further improvement in the ORR activity and stability was done by depositing a Pt monolayer on the IrNi core-shell nanoparticles deposited on the glassy carbon electrode and also using the scale-up synthesis method. The catalyst was characterized by *in situ* x-ray absorption spectroscopy (XAS), TEM-EELS and RDE technique. Due to the electronic interactions between Ir and Ni substrate, the Pt monolayer modifies the surface electronic structure and thereby changes its chemical properties resulting in enhanced electrocatalytic activity. The expansion in Ni bonds and the contract in Ir bonds as a consequence of the formation of IrNi solid solution alloy prevent the dissolution of the core material from the bulk phase of nanoparticles, thus making it very stable for ORR. The DFT calculations were carried out to address the possible mechanism for the observed enhancement in activity and durability.

Chapter 2. Experimental Methods and Techniques

2.1 Synthesis of carbon supported IrNi core-shell nanoparticles

Carbon supported Iridium (Ir) and Nickel (Ni) core-shell nanoparticle were prepared by mixing equal molecular ratio of $(NH_4)_2IrCl_6$, $Ni(HCO_2)2H_2O$ salts with high area Vulcan XC72R carbon black to obtain the loading of 20 wt-% total metal. The mixture was dissolved in Millipore water and purged with Ar under ultrasonic bath for an hour. The salts were then reduced by adding $NaBH_4$ simultaneously purging with Ar. The mixture obtained was washed and rinsed with Millipore water and then dried. The dried mixture was annealed at 600°C under H_2 for 2 hours in a tube furnace, to obtain a surface segregation of the noble metal. Chemical analysis of the resultant IrNi sample was carried out using energy-dispersive X-ray (EDX) equipped with a JEOL JEM2100F transmission electron microscope. The mean mole ratio of Ni to Ir (x_{Ni}/x_{Ir}) determined from eight particles was 0.56 with a standard deviation of 0.02.

2.2 Pt monolayer deposition on IrNi core-shell nanoparticles

2.2.1 RDE Method

Catalyst inks of IrNi/C nanoparticles were prepared by mixing 5mg of catalysts with 5mL of 18 MΩ water. The solution was ultrasonicated for 10 min or until a dark, uniform ink was achieved. Thin-film electrodes with IrNi/C nanoparticles were prepared by placing 10µl of nanoparticle suspension onto a flat glassy carbon electrode (5-mm diameter, Pine Instrument). After drying in vacuum, the electrode was covered with 10 µl of a dilute Nafion solution (2 µg/5 µl) and dried again. The Pt monolayer was placed on the IrNi/C thin-film electrode by galvanic displacement of a Cu monolayer formed by under potential deposition (UPD) with Pt. The Cu

monolayer was deposited in a 50 mM H_2SO_4 + 50 mM $CuSO_4$ solution. The electrode covered with a Cu monolayer, was rinsed and immersed in a 1.0 mM K_2PtCl_4 + 50 mM H_2SO_4 solution to displace the Cu with Pt. A leak-free reference electrode (Ag/AgCl) was used. All the potentials are given with respect to a reversible hydrogen electrode (RHE). A platinum wire served as the counter electrode. The electrolytes were prepared from Optima sulfuric acid and perchloric acid (Fisher), and MilliQ UV-plus water. All these procedures were carried out in a multi-compartment electrochemical cell as shown in figure 2.1 purged with Ar to prevent the oxidation of Cu ad atoms.

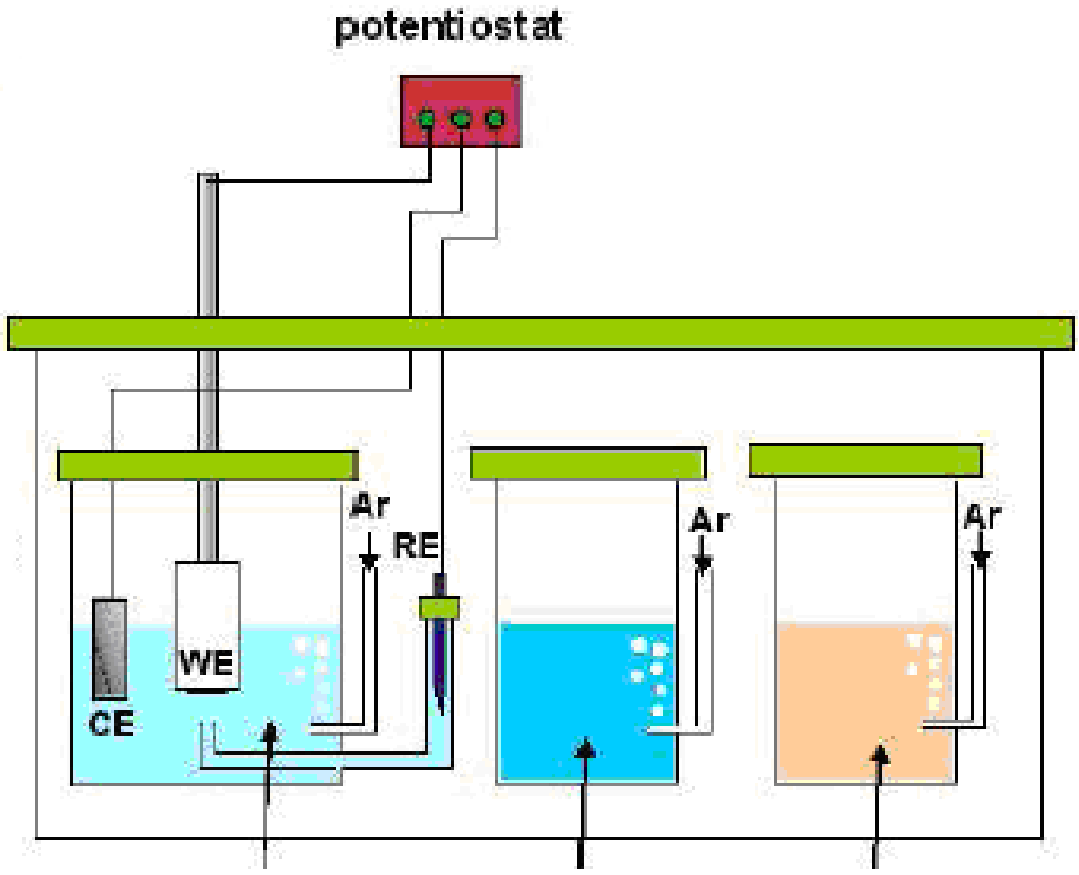

Figure2.1. Illustration of procedures of Pt monolayer deposition on metal nanoparticles using RDE synthesis

The mechanism of UPD has been extensively investigated with various electrochemical [103] and surface characterization techniques [104]. Cyclic voltammetry is customarily employed to deduce the UPD shift, viz. the difference between the peak potentials of monolayer formation and bulk deposition [105]. The formation of the first monolayer is inferred from the pronounced current peaks at the potential $E > E_{rev}$ while the bulk deposition occurs at $E < E_{rev}$ where E_{rev} denotes the Nernstian equilibrium potential (for example, UPD of Cu on Au occurs at 0.46V while bulk deposition occurs at 0.24V, E_{rev} being 0.34V vs Standard Hydrogen Electrode). Figure 2.2 depicts the constituent processes involved in the monolayer formation of metal on substrate. Since the UPD shift denotes the difference in potential between the monolayer formation and bulk deposition, it is imperative to consider the two processes separately. The monolayer formation of metal on substrate can be envisaged as follows [106]:(i) movement of the solvated ions from the bulk to the reaction zone, getting rid of their solvation sheath, and (ii) electron transfer from the substrate to the metal ions leading to the subsequent bond formation with the substrate.

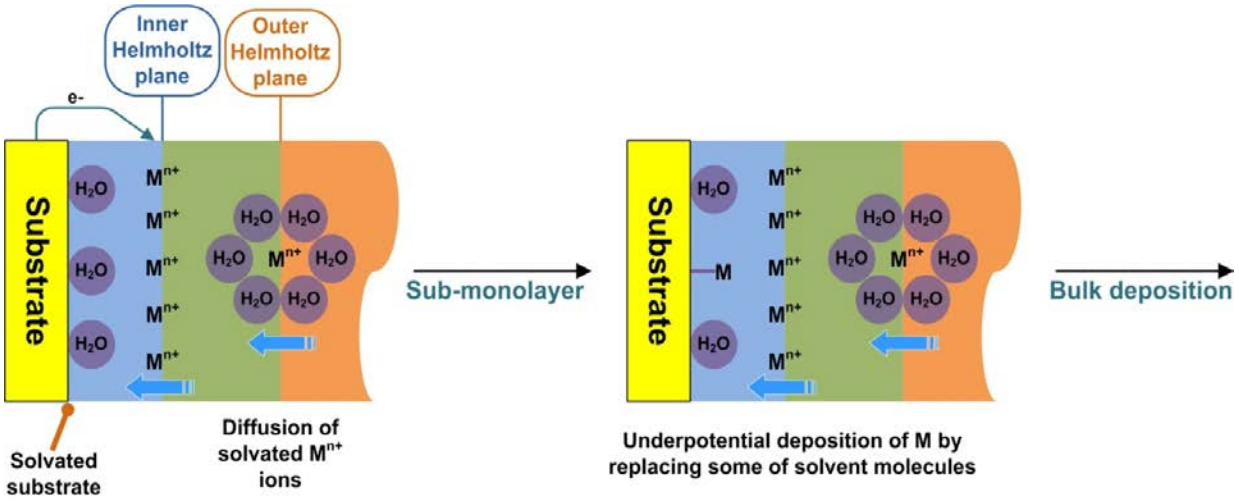

Figure2.2. Schematic representation of processes constituting adsorption of metal upon substrate.

2.2.2 Scale-up synthesis method

The gram-scale sample was produced in a 1gm batch synthesized in a home-designed electrochemical cell which consists of a Ti cylinder as shown in figure 2.3 that acts as a working electrode, Pt black as counter electrode and an Ag/AgCl/KCl (3M) leak-free electrode as reference electrode. Detailed explanation of the electrochemical cell can be found elsewhere [107].

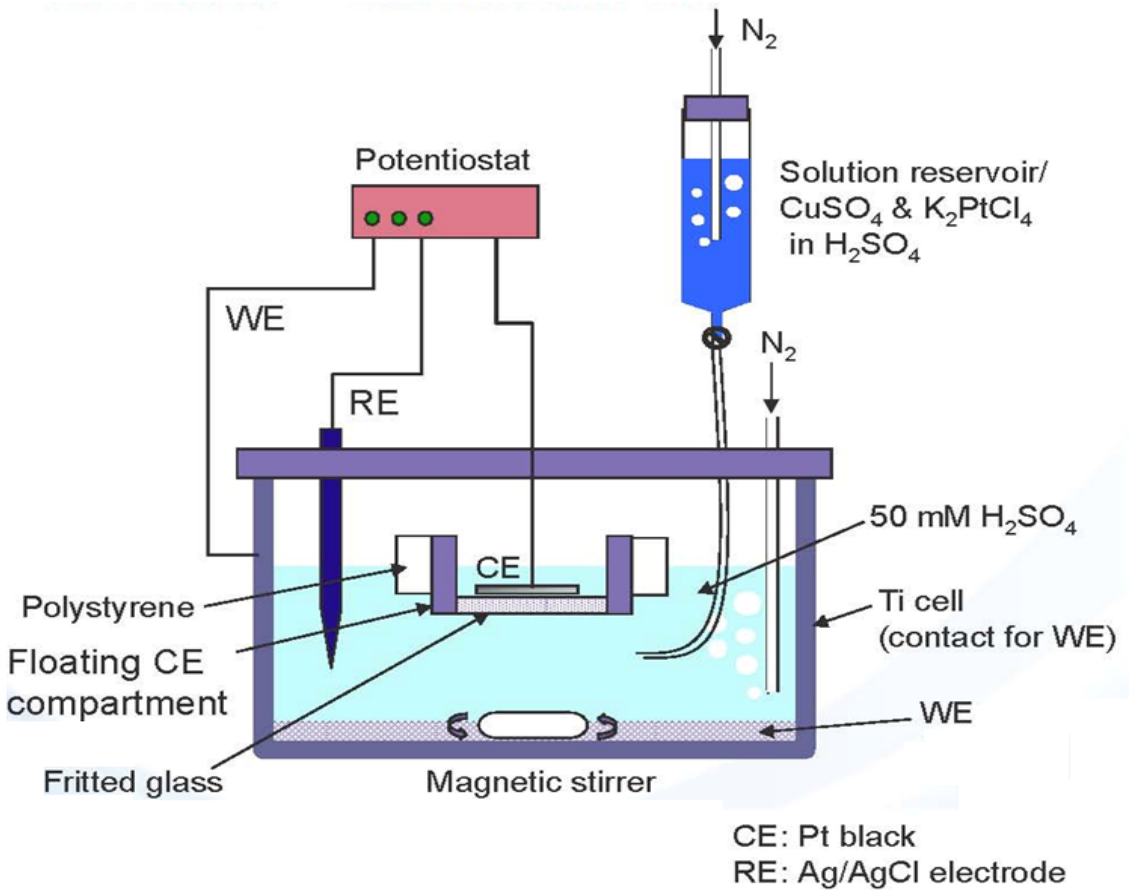

Figure2.3. Illustration of the electrochemical cell used for Pt monolayer deposition

After reducing IrNi nanoparticles surface oxides by applying potential cycles in 50 mM H_2SO_4 solution, $CuSO_4$ solution (50mM) is added in the cell. Purged continuously with Ar gas, a constant potential is then applied to form UPD Cu adatoms on the IrNi nanoparticle surfaces. At

constant potential, the solution is occasionally magnetic stirred to disperse the IrNi/C particles in the electrolyte, and therefore to ensure the formation of UPD Cu monolayer's on the whole surfaces. The Cu UPD process is carried out until the current becomes a steady value near zero. After the Cu UPD formation, a Pt^{2+} solution (K_2PtCl_4 in a 50mM H_2SO_4 solution) in a separate reservoir is injected slowly into the cell. To allow Pt atoms to replace Cu monolayer's on IrNi surfaces galvanically the solution is vigorously stirred. The resultant Pt/IrNi/C electrocatalyst is washed repeatedly by filtering. The Pt content in the scale-up synthesis sample (4.4 wt. %) were determined by assay elemental analysis using inductively coupled plasma (ICP) emission spectroscopy. From combined XAS and EDX/TEM elemental analysis we get the final product molar ratio as Pt $Ir_{2.29}$ $Ni_{1.29}$.

2.3 Rotating Disk Electrode (RDE)

Rotating disk electrode is a kind of hydrodynamic technique involving forced convection. Hydrodynamic methods have two major advantages. One is that a steady state is attained quickly. The other is that the rates of mass transfer at the electrode surface are much larger than the one of diffusion which results in the much smaller effect of mass transfer to electron transfer kinetics. In addition, the valuable time variable is introduced in the RDE method with the rotation rate of the electrode.

2.3.1 Determination of the Velocity Profile

For an incompressible fluid, the velocity profile is obtained by solving the continuity equation and the Navier-Stokes equation. The continuity equation is given by

$$\nabla \cdot \mathbf{v} = \mathbf{div}\ \mathbf{v} = 0 \tag{2.1}$$

that is a statement of incompressibility. The Navier-Stokes equation representing Newton's first law (**F**= m**a**) for a fluid is given by

$$d_s \frac{dv}{dt} = -\nabla \boldsymbol{P} + \eta_s \nabla^2 \mathbf{v} + \mathbf{f} \tag{2.2}$$

The left and the right sides presents $m\boldsymbol{a}$ per unit volume and the total force ($\boldsymbol{P}$ is the pressure, $\eta_s \nabla^2 \mathbf{v}$ the frictional forces, and **f** the force/volume exerted on an element of fluid by gravitational forces).

In electrochemical system only the steady velocity profile is of interest. Thus, eq. 2.2 is solved for $dv/dt = 0$. In a system involved forced convection, such as RDE, the gravitational effects from **f** is neglectable, i.e. $\mathbf{f} = 0$

The velocity profile, **v** of a fluid near a rotating disk was calculated by Von Karman and Cochran by solving the hydrodynamic equations under steady state. In the symmetrical system like a disk rotating in a solution, it is convenient to express the hydrodynamic equations in terms of cylindrical coordinate's *r*, *y* and *Ø* (Figure 2.4). In cylindrical coordinates, the velocity is expressed as

$$\mathbf{v} = v_r \boldsymbol{\mu}_1 + v_y \boldsymbol{\mu}_2 + v_\phi \boldsymbol{\mu}_3 \tag{2.3}$$

where $\boldsymbol{\mu}_1$, $\boldsymbol{\mu}_2$, $\boldsymbol{\mu}_3$ are unit vectors in the directions of positive changes of *r*, *y* and *Ø* respectively.

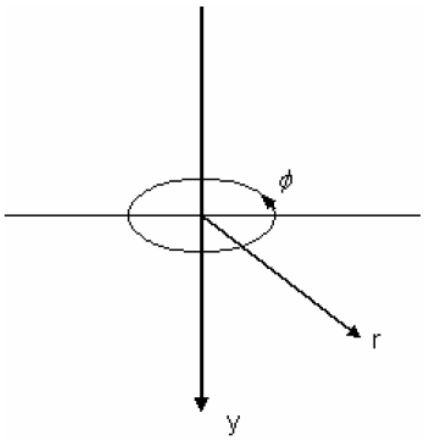

Figure2.4. Cylindrical polar coordinates for rotating disk

The divergence and Laplacian are given by

$$\nabla \cdot \mathbf{v} = \frac{1}{r^2}\left[\frac{\partial}{\partial r}(v_r r^2) + \frac{\partial}{\partial y}\left(v_y r^2\right) + \frac{\partial}{\partial \phi}(v_\phi)\right] \tag{2.4}$$

$$\nabla^2 = \frac{1}{r}\left[\frac{\partial}{\partial r}\left(r\frac{\partial}{\partial r}\right) + \frac{\partial}{\partial y}\left(r\frac{\partial}{\partial y}\right) + \frac{\partial}{\partial \phi}\left(r\frac{\partial}{\partial \phi}\right)\right] \tag{2.5}$$

The boundary conditions at the disk surface (y = 0) are:

$v_r = 0$, $v_y = 0$ and $v_\varnothing = \varpi r$

This implies that the solution is dragged along the electrodes surface with an angular velocity ϖ.

The boundary conditions in the bulk solution (y $\rightarrow\infty$) are:

$v_r = 0$, $v_\varnothing = 0$ and $v_y = -U_0$

This indicates that there is no fluid flow in the *r* and *Ø* directions. While the solution flows towards the disk with a constant velocity, U_0. The values of the velocities derived by Von Karman and Cochran, in the form of infinite series in terms of dimensionless variable γ, where

$$\gamma = \left[\frac{\omega}{y}\right]^{1/2} y \tag{2.6}$$

$$v_r = r\omega(\gamma) = r\omega\left[a\gamma - \frac{\gamma^2}{2} - \frac{1}{3}b\gamma^3 + \cdots\right] \tag{2.7}$$

$$v_\phi = r\omega G(\gamma) = r\omega\left[1 + b\gamma + \frac{1}{3}a\gamma^3 + \cdots\right] \tag{2.8}$$

$$v_y = [\omega v]^{1/2} H[\gamma] = [\omega v]^{1/2}\left[-a\gamma^2 + \frac{\gamma^3}{3} + \frac{b\gamma^4}{6} + \cdots\right] \tag{2.9}$$

a = 0.51023 and b= -0.6159

For the RDE in an electrochemical system, the most important velocities are v_r and v_y. Near the electrode surface, y →0, Eq. 2.7 and 2.9 can be simplified to Eq. 2.10 and 2.11.

$$v_r = r\omega(a\gamma) = 0.51\omega^{3/2}v^{-1/2}ry \tag{2.10}$$

$$v_y = [\omega v]^{1/2}[-a\gamma^2] = -0.51\omega^{3/2}v^{-1/2}y^2 \tag{2.11}$$

The limiting velocity in the *y* direction, U_0 is

$$U_0 = \lim_{y\to\infty} v_y = -0.88447[\omega v]^{1/2} \tag{2.12}$$

2.3.2 Solution of the Convective-Diffusion Equation

The general convective-diffusion equation is

$$\frac{\partial C_j}{\partial t} = D_j \nabla^2 C_j - \mathbf{v} \cdot \nabla C_j \tag{2.13}$$

where C_j is the concentration of the species, $\nabla^2 \equiv \frac{c^2}{\partial x^2} + \frac{\partial^2}{\partial y^2} + \frac{\partial^2}{\partial z^2}$ is the Laplacian operator and $\nabla \equiv \mathbf{i}\frac{\partial}{\partial x} + \mathbf{j}\frac{\partial}{\partial y} + \mathbf{k}\frac{\partial}{\partial z}$. Under the steady state condition, $(\partial C_j / \partial t) = 0$. Thus the steady state convective-diffusion equation written in terms of cylindrical coordinates becomes

$$v_r\left(\frac{\partial C_0}{\partial r}\right) + \frac{v_\emptyset}{r}\left(\frac{\partial C_0}{\partial \emptyset}\right) + v_y\left(\frac{\partial C_0}{\partial y}\right) = D_0\left[\frac{\partial^2 C_0}{\partial y^2} + \frac{\partial^2 C_0}{\partial r^2} + \frac{1}{r}\frac{\partial C_0}{\partial r} + \frac{1}{r^2}\left(\frac{\partial^2 C_0}{\partial \emptyset^2}\right)\right] \tag{2.14}$$

for the limiting current condition, the boundary conditions are $y = 0$, $C_0 = 0$ and $C = C_0^*$. Because C_0 is not a function of $\emptyset$, $\left(\frac{\partial C_0}{\partial \emptyset}\right) = \left(\frac{\partial^2 C_0}{\partial \emptyset^2}\right) = 0$. In addition, v_y is not related to r, and at $y = 0$, $\left(\frac{\partial C_0}{\partial r}\right) = 0$. Thus across the face of the disk electrode, Eq. 2.14 is simplified to be

$$v_y = \left(\frac{\partial C_0}{\partial y}\right) = D_0 \frac{\partial^2 C_0}{\partial y^2} \tag{2.15}$$

by substitution of the value of v_y from Eq. 2.11, this equation can be solved directly by integration and after making a substitution of $z = y^3/3B$, the final result is given by

$$C_0^* = \left(\frac{\partial C_0}{\partial y}\right)_{y=0} 0.8934\left[\frac{3D_0 \varpi^{-3/2} \nu^{1/2}}{0.51}\right]^{1/3} \tag{2.16}$$

The current *i*, is the flux at the electrode surface that is given by

$$i = nFAD_0 \left(\frac{\partial C_0}{\partial y}\right)_{y=0} \tag{2.17}$$

where, *n* is the number of charge transfer, *F* is the Faraday constant and *A* is the electrode area. Under the chosen current conditions, $i = i_{l,c}$, from (2.16) and (2.17), we obtain the Levich equation:

$$i_{l,c} = 0.62nFAD_0^{2/3}\omega^{1/2}v^{-1/6}C_0^* \tag{2.18}$$

It predicts that the limiting current is proportional to the bulk concentration of the reaction species and the square root of the angular velocity.

2.3.3 General Polarization curves at the RDE

For a total irreversible one-step, one-electron reaction, the disk current is

$$i = FAk_f(E)C_0 \text{ (y = 0)} \tag{2.19}$$

where k_f is the reaction rate constant, which is a function of potential *E* . Since we know that the general current-potential equation at planar electrode is

$$i = FAk_f(E)C_0^*\left(1 - \frac{i}{i_{l,c}}\right) \tag{2.20}$$

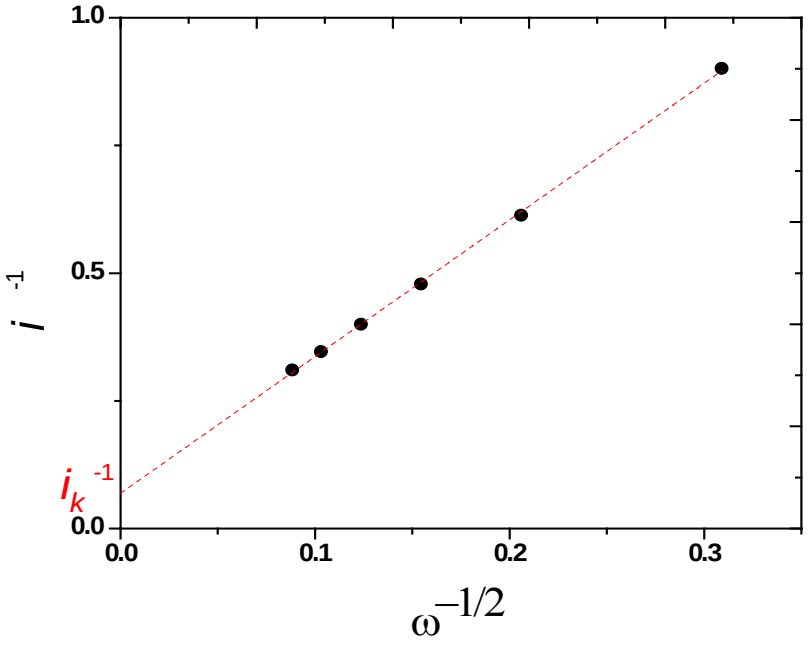

Figure2.5. The *Koutecký-Levich plot*

with rearrangement and defining,

$$i = FAk_f(E)C_0^* \tag{2.21}$$

one obtains the *Koutecký-Levich equation*:

$$\frac{1}{i} = \frac{1}{i_k} + \frac{1}{i_{l,c}} = \frac{1}{i_k} + \frac{1}{0.62nFAD_0^{2/3}\varpi^{1/2}\nu^{-1/6}C_0^*} \tag{2.22}$$

where i_k represents the current without any mass transfer effects. If ($1/i$) is plotted against $\varpi^{-1/2}$, apparently a linear curve will be obtained (Figure 2.5). The intercept of this plot is ($1/i_k$) from

which the kinetic parameters can be determined. The slope of the plot can be used to estimate the number of electrons involved in the reaction.

The ORR activity of Pt-based catalysts is generally quantified by measuring the current at 0.9 V vs. the reversible hydrogen electrode (RHE) and dividing this current either by Pt mass to obtain the so-called mass activity ($i_{m(0.9\ V)}$ in units of A/mg_{Pt}) or by the electrochemically active Pt surface area to obtain the so-called specific activity ($i_{s(0.9\ V)}$ in units of mA/cm_{Pt}^{2}). While mass activity is the relevant figure-of-merit for practical applications, as it dictates the required Pt loading in a fuel cell, the specific activity is a more fundamental measure of the intrinsic activity of a Pt-based catalyst.

2.4 Synchrotron Techniques

X-rays have been used as one of the most important characterization tool, ever since the history of modern science. With the advent of synchrotron radiation source x-ray absorption spectroscopy (XAS) has become a powerful tool for *in situ* characterization of electrode/electrolyte interface. A great advantage is that XAS is element specific and this permits investigation of the chemical environment of an element in a composite material. It can not only provide compositional information but also average information on atomic structures from thousands of nanoparticles. [108, 109]

2.4.1 Absorption Coefficients and Absorption Edges

When a collimated beam of monochromatic x-ray travels through a material of thickness *x*, it will lose its intensity via interaction with the material. The intensity loss is proportional to the original intensity and the thickness of the material.

$$dI = -\mu I dx \tag{2.23}$$

where μ is the proportionality constant known as the linear absorption coefficient. Integrating Eq. 2.23, we obtain

$$\frac{I}{I_0} = e^{-\mu x} \tag{2.24}$$

where I and I_0 are the incident and transmitted x-ray intensities respectively. The absorption coefficient μ is approximately expressed as

$$\mu \approx \frac{Z^4}{E^3} \tag{2.25}$$

where Z is the atomic number of the element and E is the energy of the photons. As seen from Eq.2.25, μ generally decreases as the incident beam energy increases. However the absorption coefficient increases by several folds when a certain critical energy level is reached. This discontinuity called absorption edge always occurs at the energy levels corresponding to the electronic shell (K, L, M etc.) of the element, where more electrons are available for photoemission.

2.4.2 XANES and EXAFS

Figure 2.6 shows an x-ray absorption spectrum for Pt foil L_3 edge covering both the XANES and EXAFS regions. The near-edge part of the spectrum is referred to as the x-ray absorption near-edge structure (XANES). The oscillations, starting about 50eV above the edges, are the extended x-ray absorption fine structure (EXAFS). The fine structure in the XANES region can be explained in terms of (a) transition of the ejected photoelectron to unoccupied states in the vicinity of the Fermi level, and (b) to the long mean free path of the low-energy photoelectron, which results in multiple scattering around the excited atom. The shape of the edge yields information on both the type and symmetry of the ligand around the excited atom. Edge shifts due to core-hole interactions are indicative of changes in oxidation state. So XANES yields important chemical information about the absorbing atom. [109, 110]

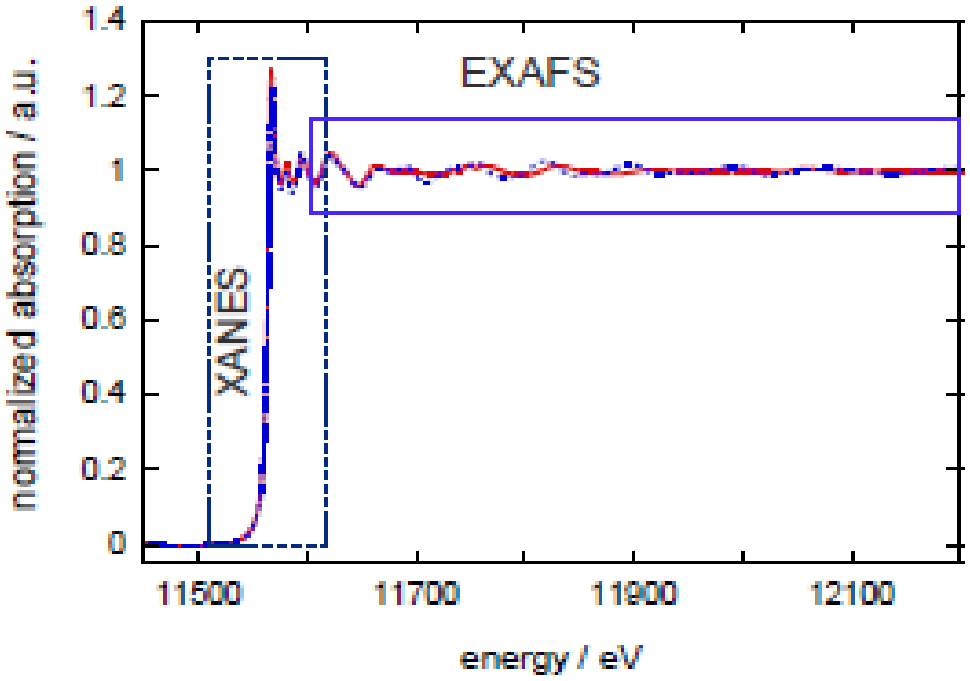

Figure2.6. XAS of Pt L_3 edge showing the XANES and EXAFS regions

The position of the absorption edge is sensitive to the valence of the absorbing atom. The edge moves to higher energies as the atom has a higher valence. The reason for this phenomenon is that as the atom becomes more positively charged, the binding energy of the core level electron increases which requires more energy to excite the core level electrons. Therefore the valence of an unknown sample can be qualitatively analyzed by comparing its XANES spectrum with suitable standards.

XANES directly probes the angular momentum of the unoccupied electronic states which may be bound or unbound, discrete or broad, atomic or molecular. The transition is restricted to the dipole selection rule $\Delta L = \pm 1$, $\Delta J = 0, \pm 1$, and $\Delta S = 0$, where L is the orbital angular momentum quantum number, J is the total angular momentum quantum number ($J = L+S, L+S-1, |L-S|$) and S is the spin angular momentum numbers. Thus, the primary transitions for transition metals are: $s \rightarrow p$ for K ($1s$ core electrons) and L_1 ($2s$ core electrons) edges, $p \rightarrow d$ for L_2 ($2p_{1/2}$ electrons) and L_3 ($2p_{3/2}$ electrons) edges. In the case of Pt the L_2 absorption edge is associated with transitions from $2p_{1/2}$ to $d_{3/2}$ states above the Fermi level. The L_3 edge corresponds to transitions from $2p_{3/2}$ to $d_{3/2}$, and $d_{5/2}$ states, see Figure 2.8. The final $5d$ states of Pt split due to spin orbit coupling effects with $5d_{5/2}$ states at higher energy levels than $5d_{3/2}$. As a result the unoccupied d states above the Fermi level are predominantly those with J = 5/2. Thus, the L_3 transitions are more favored as the final states contribute 14 times more than those with J = 3/2 as shown in Figure 2.7. The white line intensity of L_3 is much larger than that of L_2 which is due to the increase in Pt d-band vacancy. The difference in areas under the Pt L_3 and L_2 white lines between the sample and a pure Pt reference foil, one can estimate the fractional change in d-band vacancies relative to pure Pt. [28]

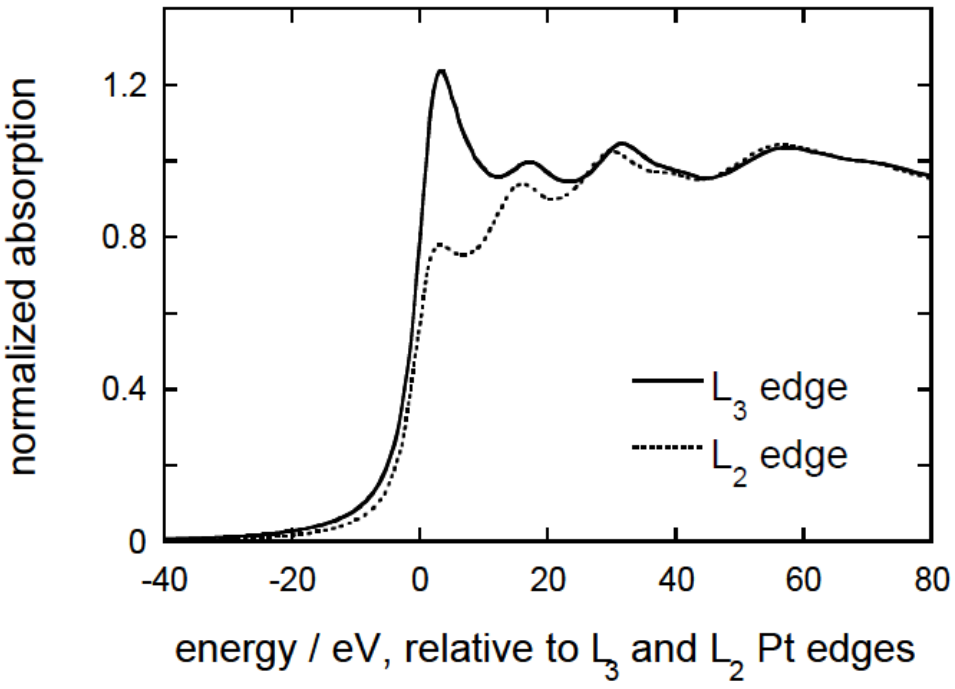

Figure2.7. Normalized Pt foil XANES spectra near L_2 and L_3 edges

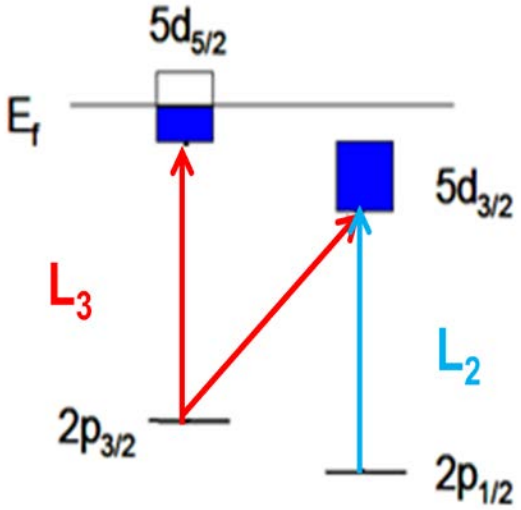

Figure2.8. Schematic of the transition of Pt L_2 and L_3 electrons

The EXAFS region is 50 to 1000eV beyond the absorption edge. It is caused by the modulation of the x-ray intensity due to back scattering by a small fraction of the backscattered photoelectron wave. This interference effect provides information about the short-range atomic order such as coordination number and bond distance.

2.4.3 XAS Experimental Set-up

Figure 2.9 is a schematic representation of the experimental set up. It consists of an x-ray source, a double-crystal monochromator, a thin sample of material, ionization chamber detectors for monitoring the intensities of the beam for the inlet (I_0), fluorescence (I_f), and transmission (I_t), and a data acquisition system. The data acquisition is used for several purposes. This includes stepping the monochromator to pass the desired photon energies, alignment of the sample in the beam, and monitoring the signals from the detectors. This was the scheme used at the National Synchrotron Light Source (NSLS) at Brookhaven National Laboratory (BNL).

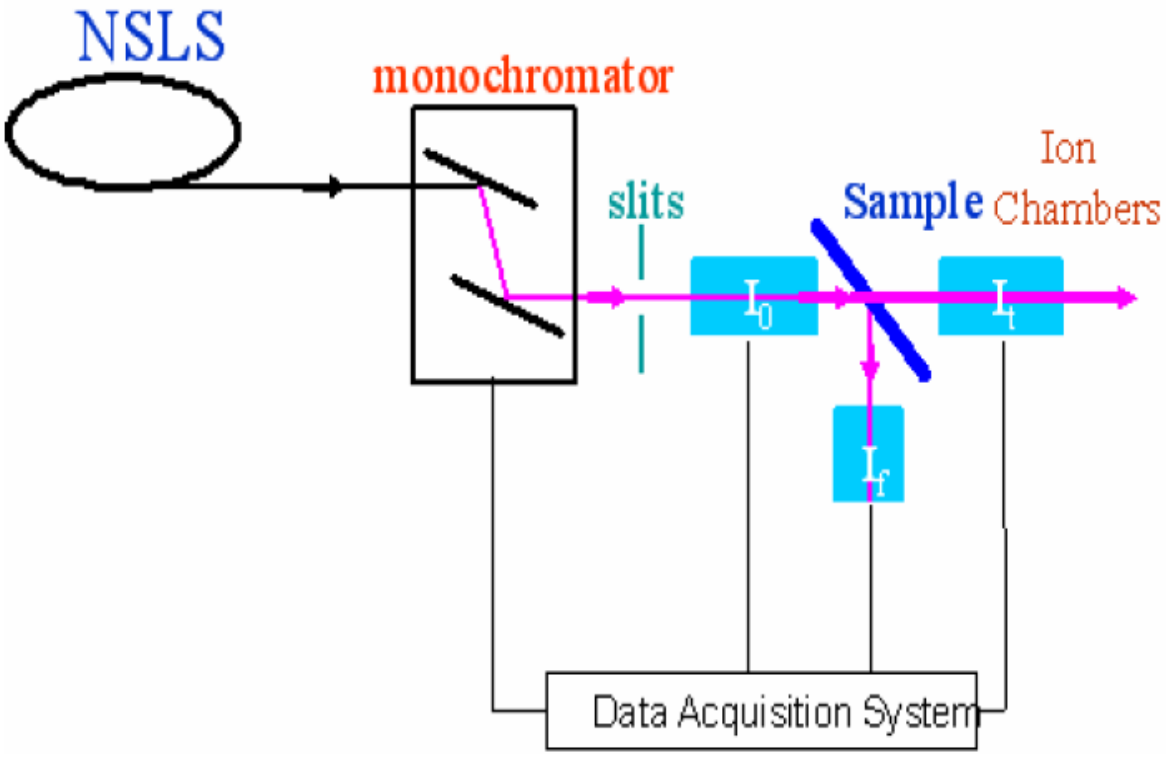

Figure2.9. Experimental setup for XAS measurements

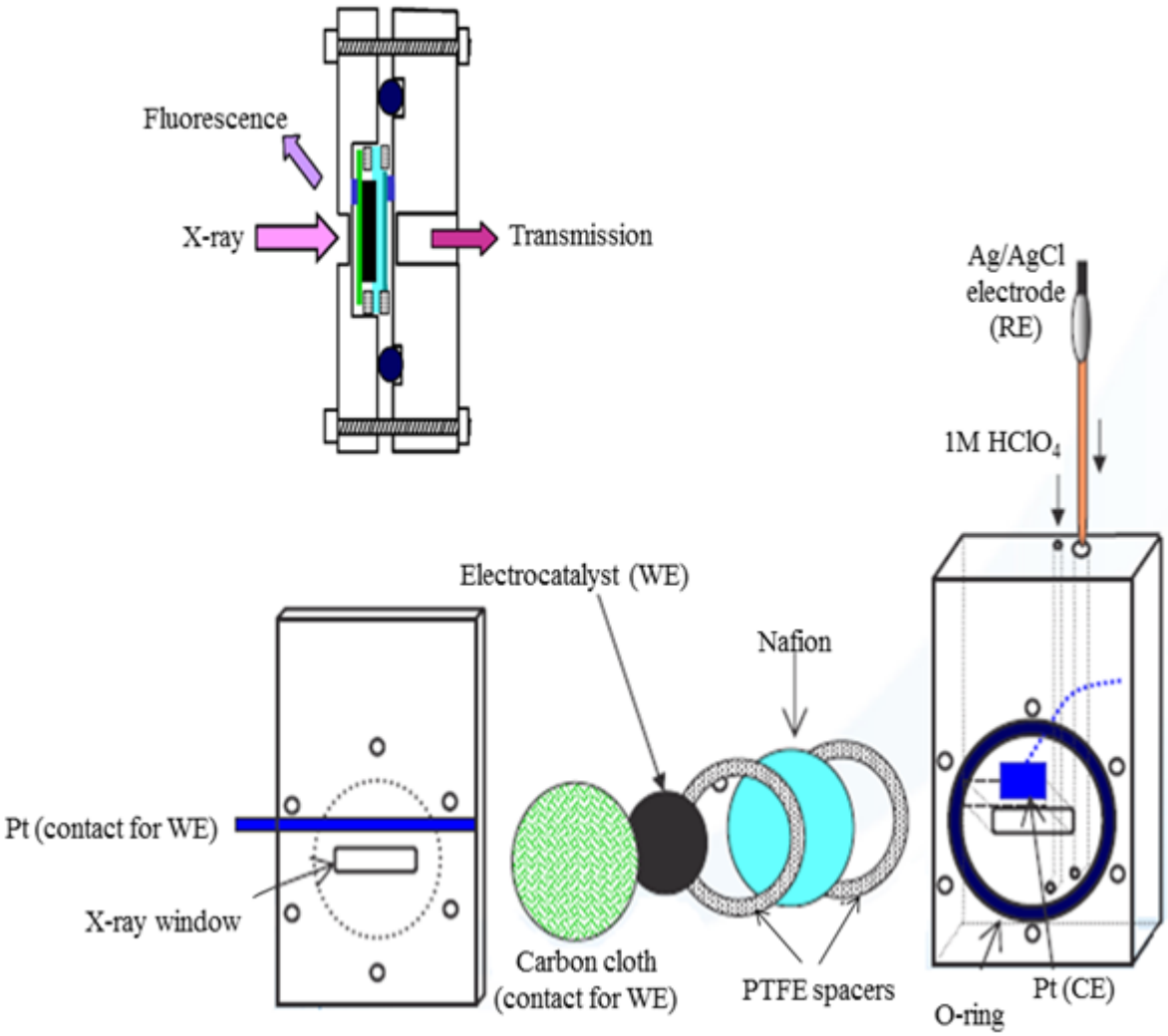

Figure2.10. Schematic diagram of the *in situ* electrochemical cell used for XAS measurements

In-situ X-ray absorption near edge structure spectroscopy (XANES) measurements were conducted using an electrochemical cell designed for acquiring good absorption spectra without compromising the electrochemistry, see figure 2.10. This electrochemical cell was designed for acquiring XAS data in both the transmission and fluorescence modes. The Pt monolayer electrocatalysts working electrode was pasted on a conductive carbon cloth which was connected to out circuit through a Pt foil. A proton exchange membrane (Nafion 117, DuPont 63 Chemical

Co., DE) separated the working and counter electrodes. All the above components were clamped tightly by two acrylic plastic bodies with an O-ring. An electrolyte of 1M $HClO_4$ was added to the cell to increase the wetting of the sample. It did not affect the measurements because of its low x-ray absorption and anion adsorption characteristics. A reference electrode (Ag/AgCl) was inserted in a compartment machined in the acrylic block. XANES measurements were carried out at the National Synchrotron Light Source (NSLS), Brookhaven National Laboratory (BNL) using Beam Line X18B and X19A.

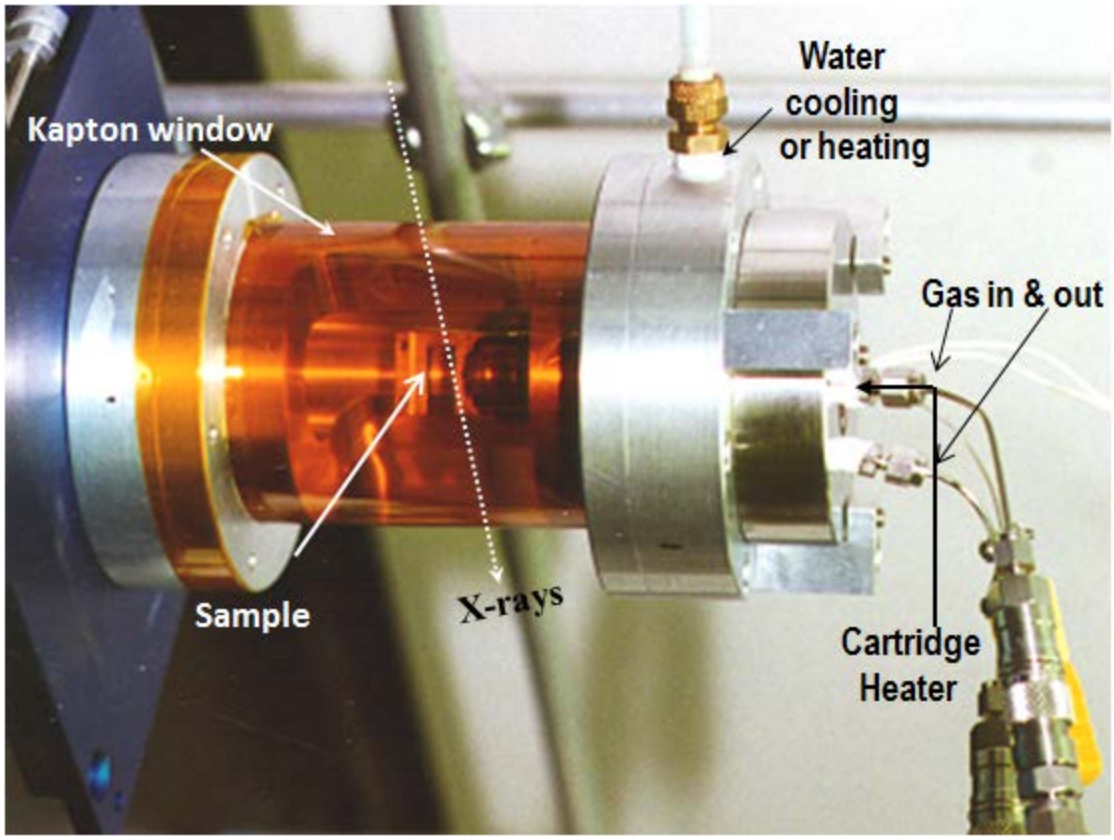

Figure2.11. Illustration of experimental set-up for *in situ* thermal XAS studies of catalysts

The other kind of XAS experiment consisted of *in situ* thermal XAS measurements; the experimental cell we used is pictured in Figure 2.11. Approximately 100 mg of carbon supported IrNi particles, which were reduced only by $NaBH_4$ but were not annealed in H_2 atmosphere, were compressed into a circular disk at room temperature; the disk was installed on a holder with a window, through which X-rays impinged on the sample disk. A resistance heater, embedded inside the holder, annealed the sample at given temperatures up to 400 ºC. We monitored the annealing temperature with a thin chromel-alumel thermocouple placed near the sample. The thermal reactor cell was shielded with a thin Kapton film, in which a gas containing 5% H_2 in He was flowed (10 mL/min) during annealing. The measurements were carried out separately at the Ir L_3 edge (11215 eV) and Ni K edge (8333 eV) from room temperature to 400ºC. The data acquired by both the electrochemical and thermal cells were processed and analyzed by Athena and Artemis software. [111]

2.4.4 In situ Time-Resolved XRD

Time-resolved synchrotron XRD studies are important technique for characterizing the structural properties of catalysts under various reaction conditions. [112-113] This technique can identify the active phase and composition of the material during the synthesis of material. It can be also used to study the crystalline size as function of time or temperature and identify crystalline or amorphous intermediates occurring in nanoparticles during phase transition. Crystal structure determination from powder diffraction data is extremely challenging due to the overlap of reflections in a powder experiment. The crystal structures of known materials can be refined, i.e. as a function of temperature or pressure, using Rietveld refinement. The Rietveld

method uses a least squares approach to refine a theoretical line profile until it matches the measured profile. [114]

2.4.5 Time-Resolved XRD Experimental Set-up

The measurements were performed at the X7B beamline at NSLS to detail the structural changes during annealing. The instrument parameters (Thompson-Cox-Hastings profile coefficients) were derived from the fit of a LaB_6 reference pattern. Approximately 5 mg of the carbon-supported IrNi nanoparticles, which were reduced only by $NaBH_4$, were loaded in a 1 mm quartz reactor (figure 2.12) that was attached to a flow system, and annealed up to 600°C at a heating rate of 4.8 °C/min. A small resistance heater was wrapped around the reactor capillary, and the temperature was monitored with a thin chromel-alumel thermocouple placed inside the capillary near the sample. A 10 mL/min gas flow containing 5% H_2 in He was maintained throughout the annealing process. The wavelength of x-ray used was 0.3184 Å. As shown in figure 2.12 XRD patterns were recorded on a Mar345 image plate detector during annealing; the recording time for a spectrum is *ca* 2.6 min. From the XRD data, accurate lattice constants, and the concentration of phases appearing during reaction were determined by a Rietveld analysis using the GSAS (general structure analysis system) program. [115-116]

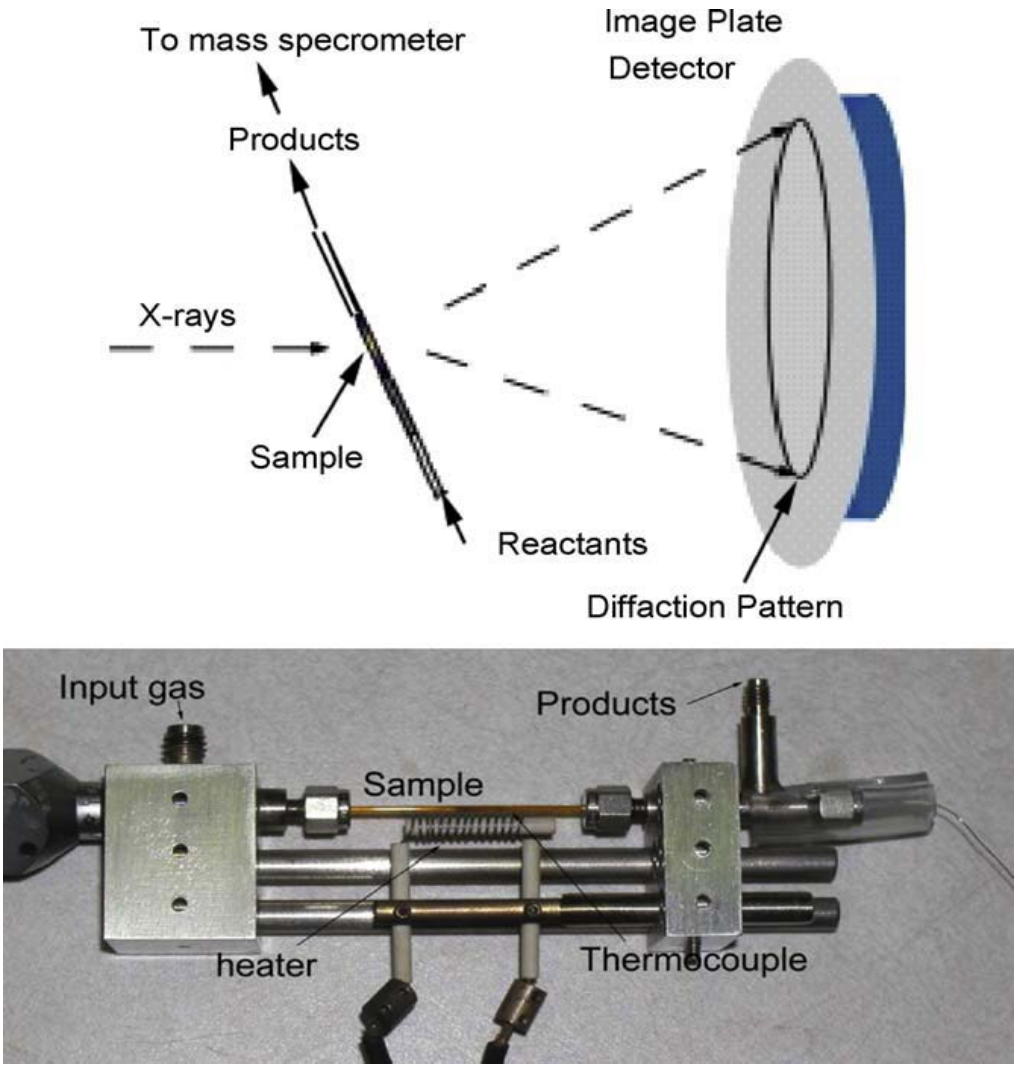

Figure2.12. Scheme of experimental set-up (top) and quartz flow cell (bottom) for *in situ* time-resolved X-ray diffraction studies of catalysts.
(From Rodriguez, J.A et al. *Catal. Today* 2009, 145, 188-194)

2.5 Structural Characterization of Electrocatalysts

X-ray Powder Diffraction (XRD) utilizes a monochromatic x-ray emission source to probe a sample in an attempt to identify crystalline structures from diffracted x-rays. The incident angle of the beam relative to the plane of the sample begins at ~10° and is increased at a steady rate sufficient to obtain a high number of counts at each point. The number of counts at

any particular angle can be correlated to the known x-ray wavelength from the source to determine the lattice spacing of a crystalline structure according to the Bragg equation. When a Bragg angle is reached, x-rays will diffract in a coherent manner, resulting in an increase in the magnitude of x-rays reaching the detector. In a plot of Counts vs 2θ (Bragg angle), this will result in peaks of various aspect ratio depending upon the distribution of crystallite sizes. Amorphous materials will result in low detection, and a steady baseline decrease in signal with increasing angle absent of any features. Detection limits vary with materials, the source emission, and detector quality. XRD measurements were taken with a Phillips 3100 diffractometer using Cu Kα radiation (1.54056 Å). Samples for analysis were obtained by loading the slurries onto a glass slide, followed by drying them in air. The diffraction patterns were collected from 20° to 80° at a scanning rate of 0.6° per minute, with a step size of 0.02°.

Transmission electron microscopy (TEM) provide visual means of examining the particle size distribution, micro-structure, and homogeneity of a powder. It probes a sample using an accelerated beam of electrons. A TEM beam is accelerated at 100keV-300keV and detects electrons which pass through the sample. The resulting image depicts the silhouette of a cross section from within the sample's depth corresponding to the point at which the beam is focused. The technique requires very small amounts of a sample compared to other characterization methods. TEM, in particular, can provide a great deal of information in addition to external morphology. The ordered atomic structure of crystalline samples will diffract electrons to form a pattern which can be analyzed to determine lattice structure, as well as single crystal or poly-crystalline nature. The high spatial resolution (0.2nm) of TEM allows for analysis of individual nanoparticles apart from the surrounding material. TEM requires that samples be sufficiently thin so as to allow enough electrons to pass through to provide detectable contrast. When electrons

from the higher energy beams employed in TEMs pass through the sample, many are inelastically scattered, resulting in an energy loss. The reduced energies of scattered electrons will also be characteristic of specific elements and can be quantitatively measured. This technique is known as electron energy loss spectroscopy (EELS). More powerful electron beams allow for the excitation of higher energy orbitals closer to the atomic nucleus. For the scanning transmission electron microscopy-electron energy loss spectroscopy (STEM-EELS), Hitachi aberration-corrected scanning transmission electron microscope (HD-2700C) at the Center for Functional Nanomaterials (CFN), Brookhaven National Laboratory (BNL) was used. A schematic block diagram of a typical electron energy loss experiment is given in Figure 2.13. To form a mono-energetic beam of electrons, an electrostatic deflecting system in combination with entrance and exit slits is used to select electrons of well-defined energy from those emitted by an appropriate source. The electrons which pass through the monochromator strike the sample, and a second electrostatic system is used as an analyzer of the energy spectrum of the scattered electrons.

Figure2.13. Block diagram of an electron energy loss spectrometer

For this study, we used a 1.4Å electron probe with probe current ~50 pA. The microscope is equipped with a cold field emission electron source with energy resolution of 0.35 eV. The carbon supported nanoparticles were dispersed in water and one drop of the slurry was deposited on a carbon covered copper grid (EMS, Hatfield, PA).

2.6 Theoretical calculations

When discussing alloy catalysts the first relevant question is what the composition and atomic distribution of the exposed surfaces are, and how they may change under reaction conditions. Surface segregation of one or more of the alloy components may be driven by temperature, adsorbate, and/or electrochemical potential conditions. [117-121] Modeling these phenomena has been done with a variety of approaches including lattice models, Monte Carlo simulations, and density functional theory (DFT). [120-124] A significant starting point is the analysis introduced by Ruban et al. [124] about segregation of an infinitely diluted transition-metal solute to the surface of a host transition-metal matrix that provided a database where the dominant segregation trends in these systems can be identified.

Density functional theory has shown to be an excellent tool for providing important insights into the interpretation of experimental results, property prediction, and even first principles design of materials. [125] Significant research efforts have also been made with the goal of elucidating and finding solutions to the dissolution of platinum and especially that of other less-noble transition-metal elements in acid solution. [126-129] Norskov et al. in their d-band center model correlated the electronic structure of the surface metal (represented as the energy center of the valence d-band density of states) and its catalytic activity; [130] the model has been applied to explain the catalytic activity and electrochemical behavior of some strained surfaces and metal overlayers. Adzic et al. correlated the ORR activities of Pt monolayers supported on different noble metal single crystals and their d-band center, [37] or oxygen-binding energy calculated using DFT as shown in figure 2.14 and concluded that they show a volcano-type dependence on the center of their d-bands. This behavior is explained by two opposite trends: while a higher

lying d-band center tends to facilitate O-O bond breaking, a lower lying one tends to facilitate bond formation.

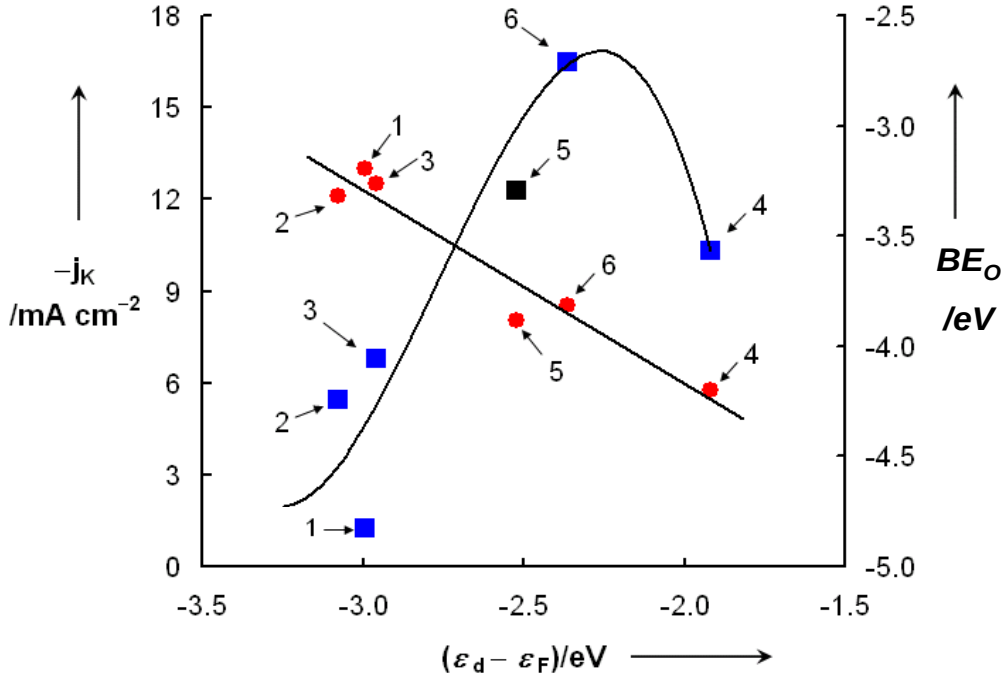

Figure2.14. Kinetic currents (j_k; square symbols) at 0.8V for O_2 reduction on the platinum monolayers supported on different single crystal surfaces in a 0.1M $HClO_4$ solution and calculated binding energies of atomic oxygen (BE_O; filled circles) as a function of calculated d-band centers (ε_d - ε_f; relative to the Fermi level) of the respective clean platinum monolayers. Labels: 1. Pt_{ML}/ Ru(0001), 2. Pt_{ML}/ Ir(111), 3. Pt_{ML}/ Rh(111), 4. Pt_{ML}/ Au(111), 5. Pt(111) 6. Pt_{ML}/ Pd(111), From J. Zhang et al. *Angew. Chem*. 2005, 117, 2170-2173.

DFT calculations were done to elucidate the observed enhancement of the Pt mass activity of Pt_{ML}/IrNi/C compared to that of Pt/C and Pt_{ML}/Ir/C electrocatalysts. DFT calculations were carried out using the Vienna ab initio simulation package (VASP) code. [131-132] Only the Γ point was used for **k** sampling, and the cut-off energy was 400 eV. We applied the projector

augmented wave method (PAW) [133] with the generalized gradient approximation (GGA) using the revised Perdew-Burke-Ernzerhof (RPBE) functional. [134] Sphere-like nanoparticle models were employed to simulate core-shell nanoparticles studied in our experiments, where all atoms were allowed to fully relax. The binding energy of atomic oxygen on the (111) plane of a nanoparticle (BE-O) was calculated and considered as a descriptor for scaling the ORR activity. Our previous studies showed that DFT calculated BE-O based on the hemisphere-like model was able to well describe the experimentally measured ORR activity of core-shell nanoparticles. [135] Here, BE-O is defined as BE-O = E[O-NP] – E[NP] – E[O], where E[O-NP], E[NP], and E[O] are, respectively, the calculated electronic energies of an adsorbed oxygen atom on a nanoparticle, a clean nanoparticle, and a triplet oxygen atom. In addition, to examine geometric effects, we predicted surface strains according to $(a - a_0)/a_0$ where a and a_0 are an averaged Pt-Pt distance of Pt monolayer and the calculated Pt-Pt distance of bulk Pt (2.824 Å), respectively.

Chapter 3. Results and Discussions

3.1 ORR activity for Pt Monolayer Deposited on Carbon Supported Ir Nanoparticles

The platinum monolayer electrocatalyst concept seems a very promising idea that can alleviate the problem of high Pt content and its low activity for the ORR. The selection of the substrates, and determination of what electronic and structural properties that substrates should have, are the key points for higher activity and durability of the catalyst. Iridium is one of the most stable metals but it shows low activity towards ORR due to disproportionately strong binding energy of oxygen at the surface. [136] As shown in the figure 2.12 (previous chapter), the experimentally measured electrocatalytic activity of platinum monolayer on various substrates for ORR shows a volcano-type dependence on the center of their d-bands determined by DFT calculations. The platinum monolayer supported on Ir(111) (denoted as Pt_{ML}/Ir(111)) shows a less ORR activity over pure Pt(111) because breaking the O-O bond is more difficult. No exclusive study has been done on Pt monolayer on Ir nanoparticles, so to understand the enhanced activity of Pt_{ML}/ IrNi catalyst we compared it with Pt_{ML}/Ir nanoparticles.

3.1.1 Pt monolayer on Carbon Supported Ir nanoparticles

Pt monolayer for carbon supported Ir (E-tek 10%) nanoparticles using the RDE synthesis method was deposited using the same procedure as mention in chapter 2, section 2.2.1. Figure 3.1(a) shows the typical curve for the underpotential deposition (upd) of Cu on an Ir surface while the dashed line shows the curve for an Ir surface in the absence of Cu ions in solution. The Cu upd area as seen in the figure 3.1(a) shows a smaller area than the H upd for Ir as two

different parameters are used in this measurement. First, the electrolyte used for Cu upd is 0.05 H_2SO_4 whereas the electrolyte for measuring CV curves for Ir is 0.1M $HClO_4$ acid and second the scan rate for Cu upd is 10mV/s, whereas the scan rate for Ir CV is 20mV/s. As the CV is different in various electrolyte conditions, the above figure should be used for visualization. Fig. 3.1(b) shows the voltammetry curve for the Pt monolayer on Ir nanoparticles obtained by displacing the Cu monolayer from Fig. 3.1(a). It depicts a characteristic hydrogen adsorption/desorption region and the PtOH formation and reduction. The upd charge was used to calculate the amount of Pt on the electrode which was 3.56μg cm^{-2}. The particle size for Ir/C nanoparticles were estimated from XRD pattern (not shown) to be 1.8 nm. The electrochemical surface areas was calculated by integrating the charges associated with the hydrogen desorption peaks in CV and the Ir metal loadings of the catalysts was determined by using the ratio of surface to total atoms of nanoparticles as a function of particle size. [137] The Ir loading was estimated to be 8.1μg cm^{-2}.

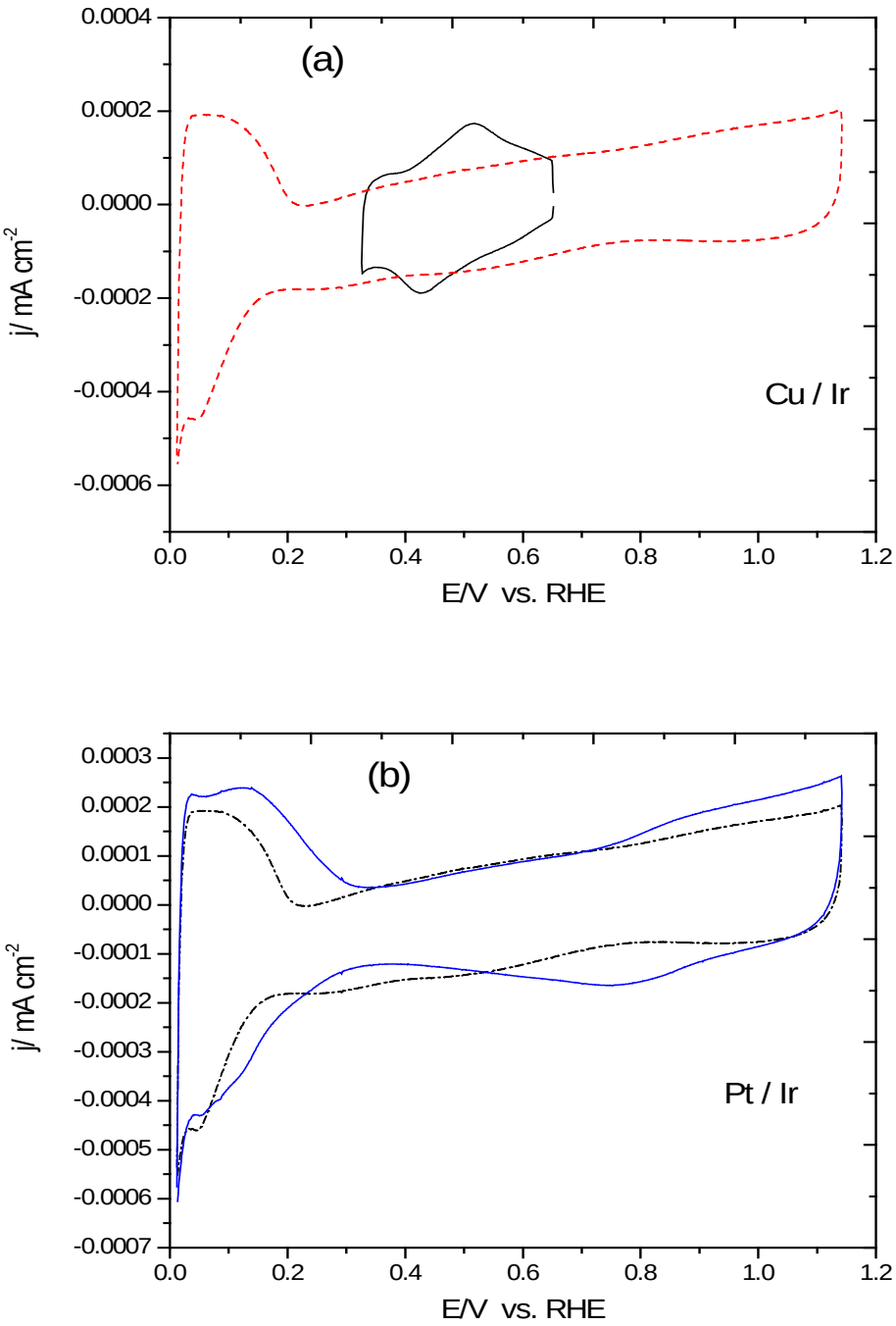

Figure3.1. (a) Voltammetry curves for the under potential deposition of Cu on a Ir surface (solid line) in 0.05M H_2SO_4 with 50mM Cu^{2+}; sweep rate 10mV/s, and for a Ir surface in the absence of Cu (dashed line)in 0.1M $HClO_4$ acid; sweep rate 20 mV/s; (b) Voltammetry curves for a Pt monolayer on a Ir surface (solid line) obtained by galvanic displacement of the Cu monolayer from Fig. 3.1a, and for a Ir surface (dashed line). The electrolyte solution is 0.1M $HClO_4$ and the sweep rate is 20mV/s.

3.1.2 ORR activity for Pt monolayer on Ir nanoparticles

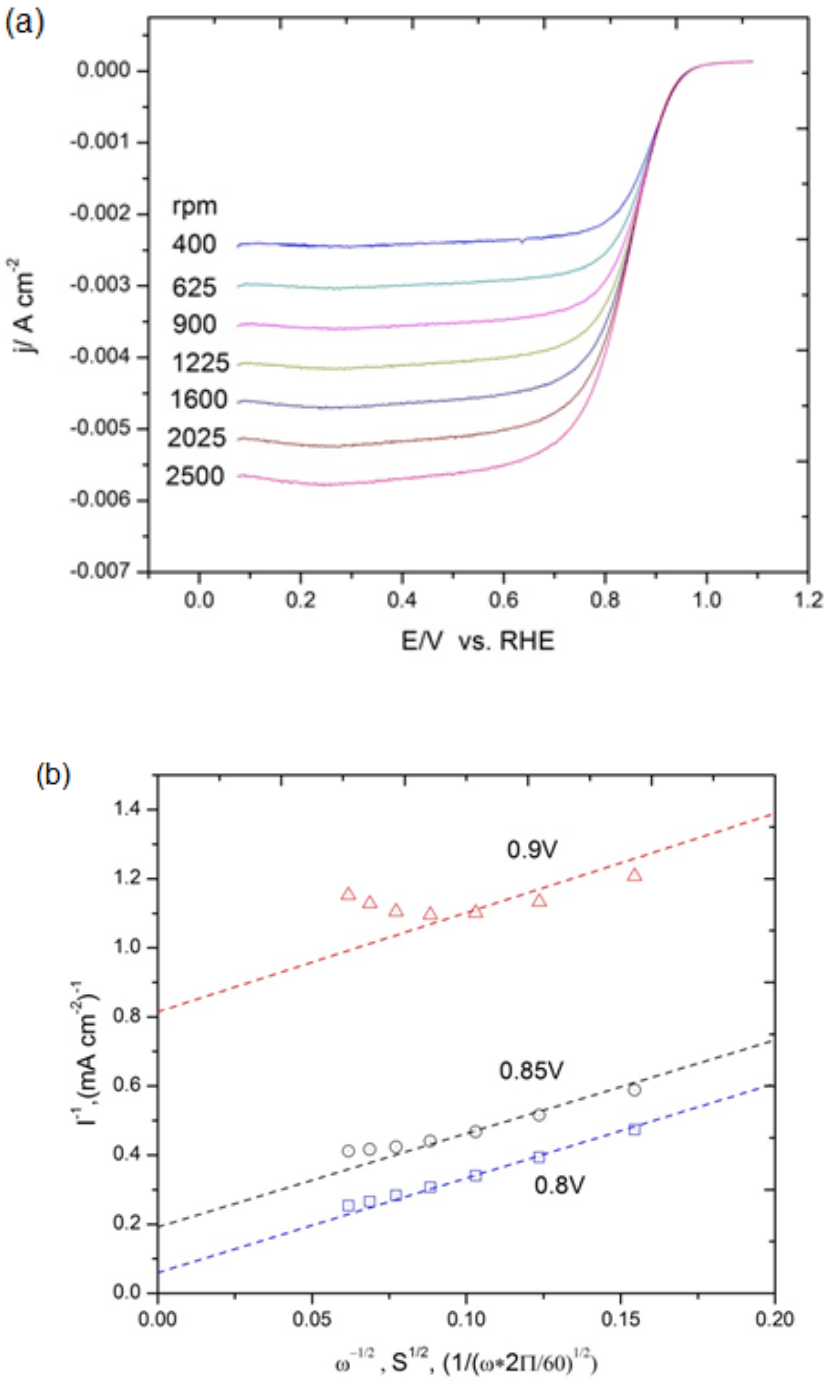

Figure3.2. (a) Polarization curves for the ORR on carbon supported Pt_{ML}/Ir surface in 0.1M $HClO_4$ solution at scan rate of 10mV/s. (b) Koutecky-Levich plots at different potentials.

Fig. 3.2(a) shows rotating disk electrode measurements of the O_2 reduction reaction on the Pt monolayer on an Ir electrode surface in a 0.1 M $HClO_4$ solution at various rotation rates. The activity of this surface is considerable, as indicated by the very positive potential at the onset of O_2 reduction (0.95-1V) and a half-wave potential of 0.850 V at 1600rpm. Fig. 3.2(b) represents the inverse current density (j^{-1}) as a function of the inverse square root of the rotation rate ($\omega^{-1/2}$), the so called Koutecky-Levich plot. The Pt mass activity and specific activity of carbon supported Pt_{ML}/Ir catalyst is 0.33A mg^{-1}_{Pt} and 0.13mA cm^{-2}at 0.9 V/RHE respectively, which almost comparably to commercial Pt/C (4nm) electrocatalyst (Table 3.3).

3.2 Pt Monolayer Deposited on Carbon Supported IrNi Nanoparticles

The carbon supported IrNi core shell nanoparticle was prepared by thermal decomposition. Figure 3.3 displays the ideal model of the synthesis of IrNi core shell nanoparticles and the deposition of Pt monolayer on them using the RDE synthesis method. The noble metal shell in the core shell nanoparticles has two roles: First, it protects the non-noble core from contacting the acid electrolyte. Second, the shell should improve the catalytic properties of a Pt monolayer by affecting its electronic properties and/or by inducing strain in a Pt monolayer that increases its activity.

A strong surface segregation of the noble metal component is the key feature of this system. The surface segregation of Ir and its protecting the Ni core from dissolution was verified by linear sweep voltammetry and upd of Cu (Figure 3.4). The voltammetry curves for the thin film electrodes of IrNi/C nanoparticles revealed no anodic currents that can be ascribed to the oxidation/dissolution of Ni, demonstrating that the cores are covered by the noble metal shell and

thus inaccessible to the electrolyte solution. The upd of Cu is evidence that the surface mainly consist of Ir; it is not apparent on Ni surface. The amount of Pt on the electrode was 8.61μg cm^{-2} calculated using the upd charge.

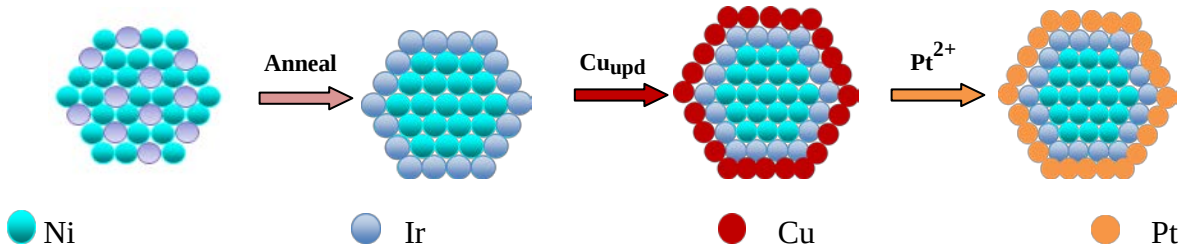

Figure3.3. Ideal model of Pt monolayer catalyst on IrNi core shell nanoparticles

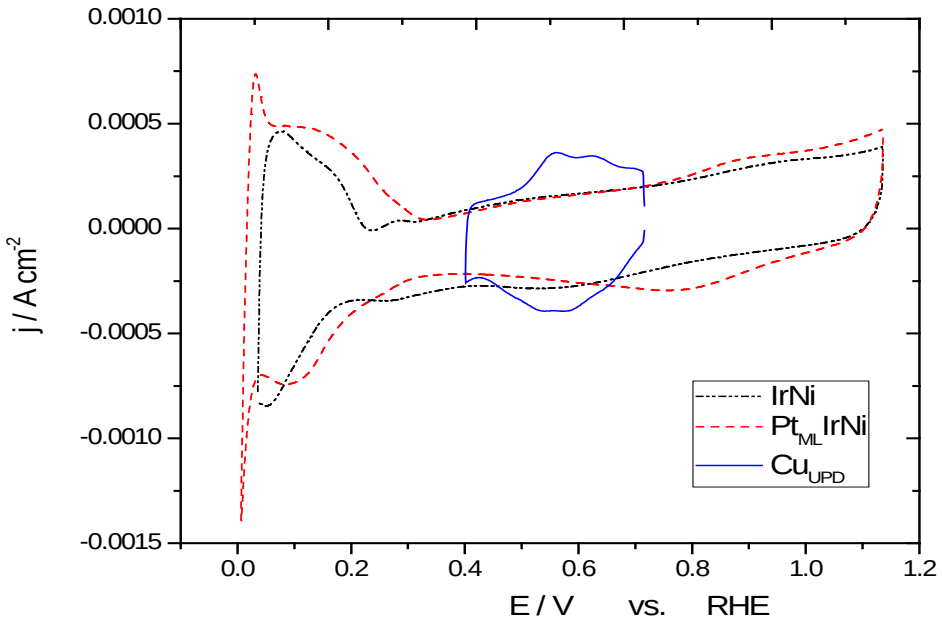

Figure3.4. Voltammetry curves for the UPD of Cu on an IrNi/C core-shell surface (blue solid line) in 50mM H_2SO_4 + 50M $CuSO_4$; sweep rate 10mV/s, and for IrNi/C (black dotted line) and with Pt monolayer (red dashed line) in 0.1M $HClO_4$; Pt loading: 8.61µgcm^{-2}; sweep rate 20mVs^{-1}

3.2.1 Structural Characterization of IrNi Core-Shell nanoparticles

Figure 3.5 shows the XRD pattern measured from the IrNi/C nanoparticles using Cu Kα radiation (1.54056 Å). There are three pronounced reflection peaks at 2θ = 42.65°, 49.61°, and 72.42°. No separate peaks for Ir or Ni were observed (the reflection peaks of (111), (200), and (220) planes for Ir and Ni are denoted by the blue and red bars, respectively). The first peak at 2θ = 42.65° is indexed between the Ir (111) and Ni (111) planes at 2θ = 40.66° and 44.51°, respectively. Ir and Ni are known to form a solid solution alloy as a bulk at all relative concentrations of the two elements.[138] The XRD pattern points to the formation of IrNi solid-solution alloy nanoparticles, possibly with an fcc structure (Fm3m) with a lattice parameter of a ≅ 3.72 Å. (We note that both Ir and Ni have an fcc structure and that the lattice parameters for Ir and Ni are 3.839 Å and 3.524 Å, respectively. [139]) The average size of the IrNi nanoparticles is 4.7 nm, estimated from Scherer's equation. [140]

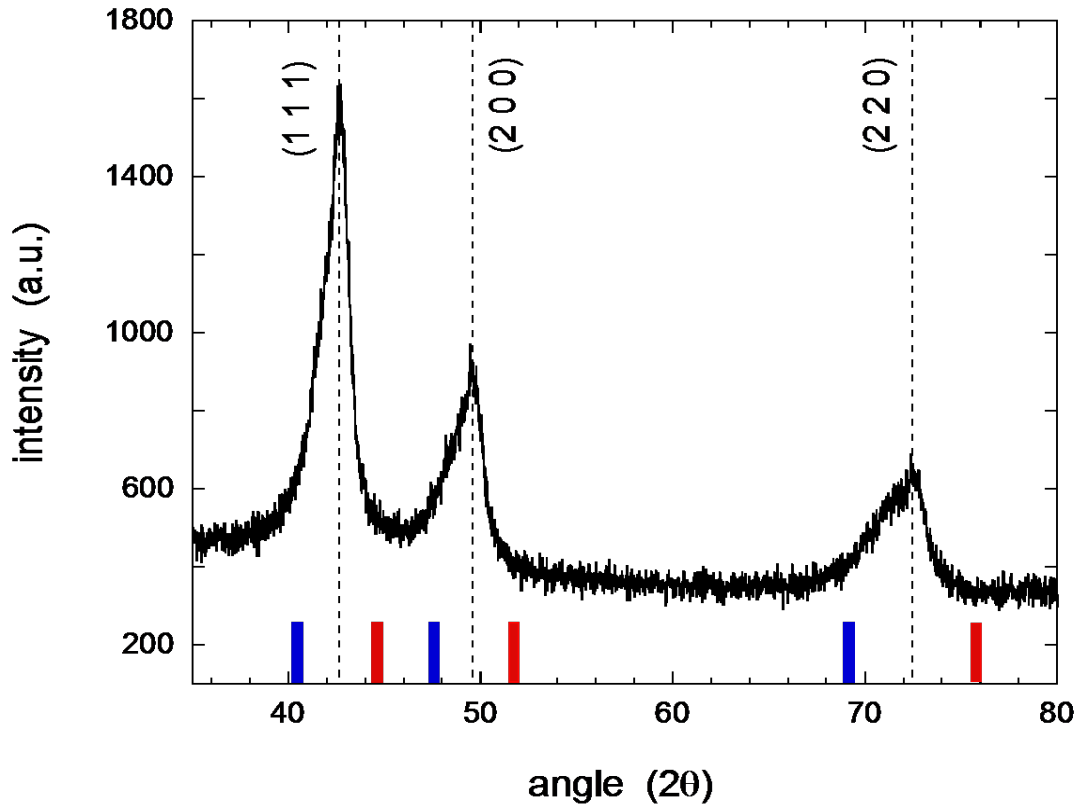

Figure3.5. XRD pattern of carbon supported IrNi nanoparticles with Cu Kα radiation after annealing at 600 °C in H_2 atmosphere for 2 h. Blue and red bars designate the (111), (200), (220) reflections from pure Ir and Ni, respectively.

Another intriguing feature in Figure 3.5 is that the reflection peaks are asymmetrical, with tails towards the 2θ values of Ir planes. The asymmetry of the XRD peaks may be caused by the Ir shells due to the segregation of Ir on the surfaces of IrNi solid solution alloy cores during annealing, as discussed below.

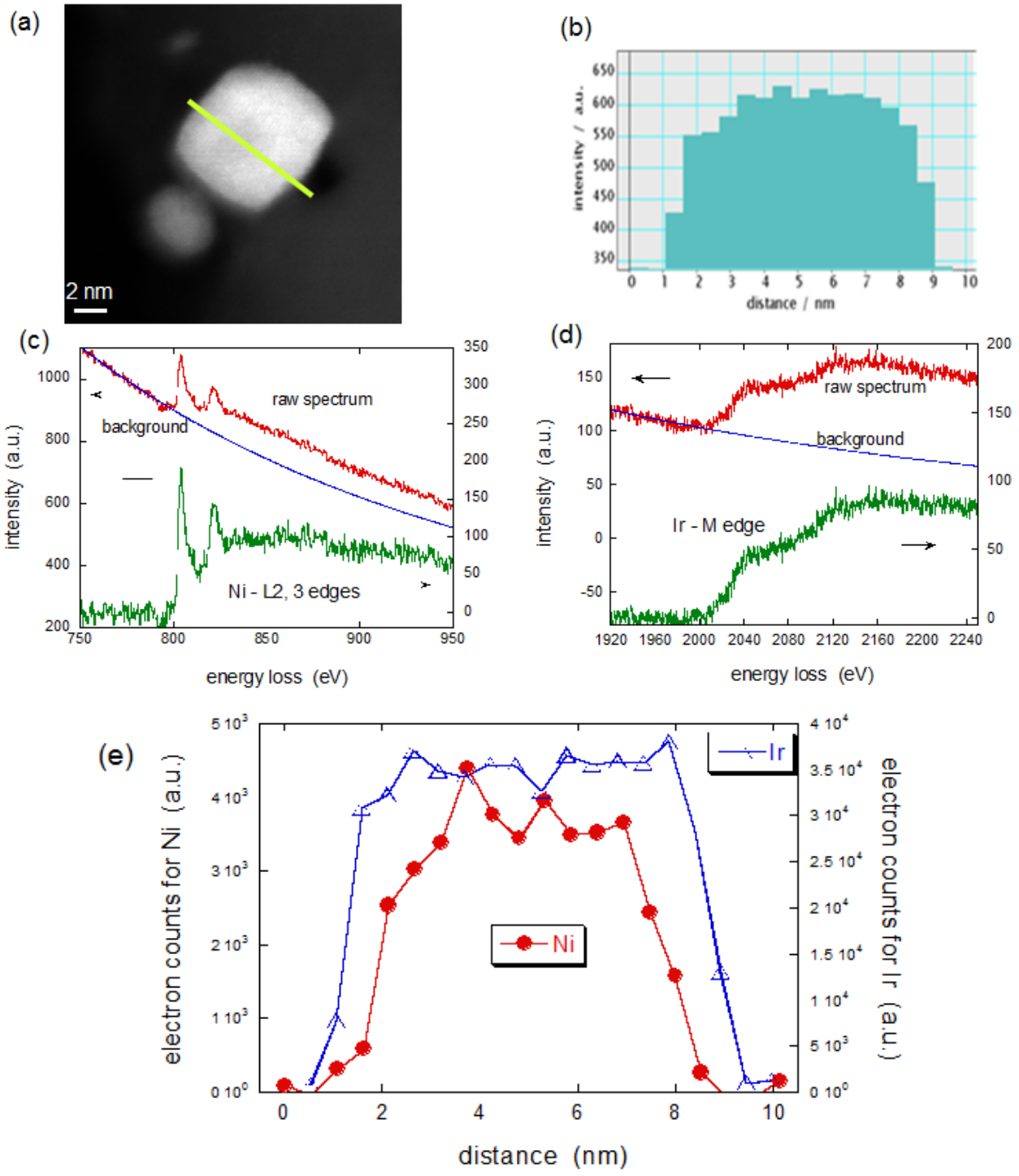

Figure3.6. (a) HAADF-STEM image of a IrNi nanoparticle: (b) HAADF intensity along the line of the nanoparticle: EELS spectra for (c) Ni L edge and (d) Ir M edge at the center of nanoparticle: and (e) comparison of the EELS intensities for the Ir M-edge and Ni L-edge along the scanned line as indicated in (a)

STEM-EELS observations were made on some of the nanoparticles. Figure 3.6 shows (a) a high angle annular dark field (HAADF) image of a single nanoparticle together with (b) the HAADF intensity profile along the line. The EELS spectra for Ni L-edge (at around 850 eV) and Ir M-edge (at around 2040 eV) taken at the center of the nanoparticle are shown in Figures (c) and (d), respectively. These figures also show the raw and background-subtracted spectra. A STEM-EELS line scan of Ir M-edge and Ni L-edge was obtained by moving the electron probe along the line indicated in Figure 3.6(a); their intensities are shown in Figure 3.6(e). It is evident that both the intensities of both Ir and Ni are approximately constant around the center of nanoparticle and that Ir is enriched (or Ni is depleted) at both edges of nanoparticles; the thickness of Ir enriched layers is *ca* 0.75~1 nm. Hence, we clearly demonstrated the formation of the Ir shell. The flat region of both Ir and Ni suggests that the core is the solid solution alloy of these two elements. The HAADF intensity profile (Figure 3.6(b)) more closely resembles the EELS profile from Ir, rather than that from Ni (Figure 3.6(e)). Since HAADF intensity is approximately proportional to the square of z [141] and the Ir mole ratio of the sample is higher than that of Ni, the HAADF profile depicted in Figure 3.6(b) likely represents the distribution of Ir in the particle.

Figure 3.7 shows another STEM-EELS observation on a different IrNi nanoparticle (Figure 3.7(a)); Figure 3.7(b) depicts the HAADF intensity profile while Figure 3.7(c) illustrates the EELS intensity profiles derived from Ir M-edge and Ni L-edge spectra, along the line designated in the HAADF image (Figure 3.7(a)). The Ni concentration decreases from the center of particle to its edge (Figure 3.7(c)); no Ni atoms are visible at the most outer layer at x = 0.3 nm. On the other hand, Ir is enriched in the surface layers (from x = 0.25 nm). By combining the XRD and the STEM-EELS measurements, it is concluded that the core-shell structure

consists of Ir-rich top layers on the surfaces of IrNi solid-solution alloy cores. Figure 3.7 shows (d) a low-resolution STEM image and (e) particle size distributions of the IrNi nanoparticles based on the statics of 150 nanoparticles. Most particles have round, sphere-like shapes, while some are slightly semi-rounded. The average particle size is determined to be 4.8 nm, which is fairly in line with the values determined by the XRD experiments.

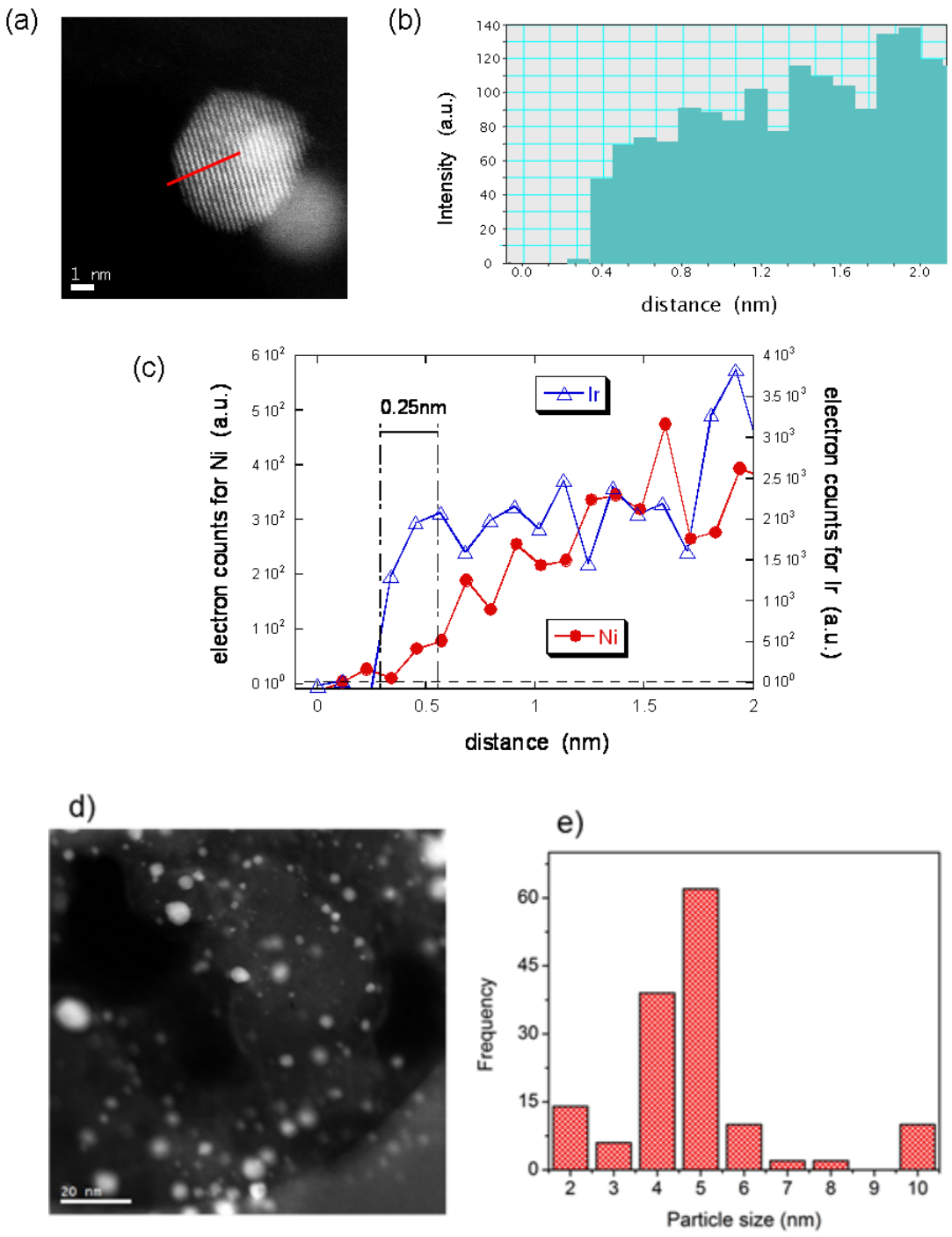

Figure3.7. (a) HAADF-STEM image of an IrNi nanoparticle: (b) HAADF intensity along a line of the nanoparticle: and (c) comparison of the EELS intensities for the Ir M-edge and Ni L-edge along the scanned line as indicated in Figure (a). (d) Low-resolution STEM image and (e) particle size distributions of the IrNi nanoparticles based on the statics of 150 nanoparticles.

3.2.2 In situ XAS study of IrNi Core-Shell nanoparticles

Figures 3.8(a) and (b) show the *in situ* XANES of the Ir L3 and Ni K edges from the IrNi nanoparticles in 1 M $HClO_4$ at a potential of 0.41 V/RHE, together with those from reference materials, viz., Ir black (the particle diameter ≅ 5 μm) and Ni foil (the thickness ≅ 10 μm), respectively. The Ni in the IrNi nanoparticles is considered to be metallic because the edge energy (E_0) [†] shows no shift compared with that of the Ni bulk foil (8333 eV). The Ni spectrum from the IrNi nanoparticles also exhibits three peaks at 8348 eV, 8353 eV, and 8378 eV; the energy values are lower and the peak intensities are higher than those for the peaks from the Ni foil, consistent with the reasonable assumption that alloying with Ir may change the electronic states of Ni atoms. Also shown in Figure 3.8(b) is the Ni K edge spectrum from the IrNi nanoparticles at a potential of 1.11 V/RHE. Surprisingly little change is observed between the two spectra at 0.41 V and 1.11 V. On the other hand the *in situ* XANES of Ir L3 edge from the IrNi nanoparticles displays a decrease in intensity of the white line compared with that from the Ir back (Figure 3.8(a)); this suggests that electronic properties of Ir may change by alloying with Ni.

[†] This is defined as the energy of first derivative of the spectrum.

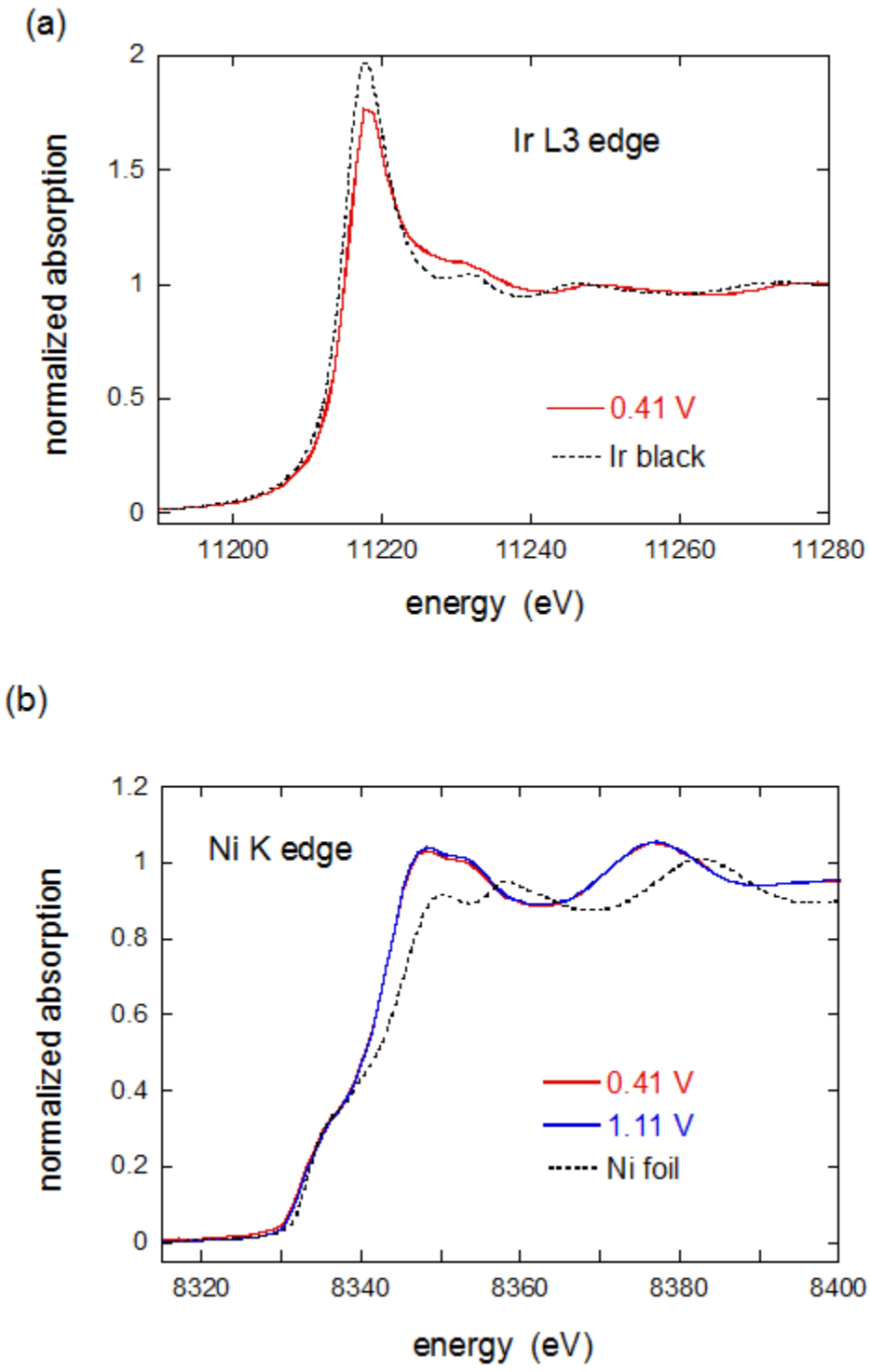

Figure3.8. *In situ* XANES of (a) Ir L3 edge and (b) Ni K edges from the IrNi nanoparticles in 1 M HClO4 at potentials of 0.41 V/RHE for (a) & (b) and 1.11 V/RHE for (b). Also shown are spectra from (a) Ir black, and (b) a Ni foil.

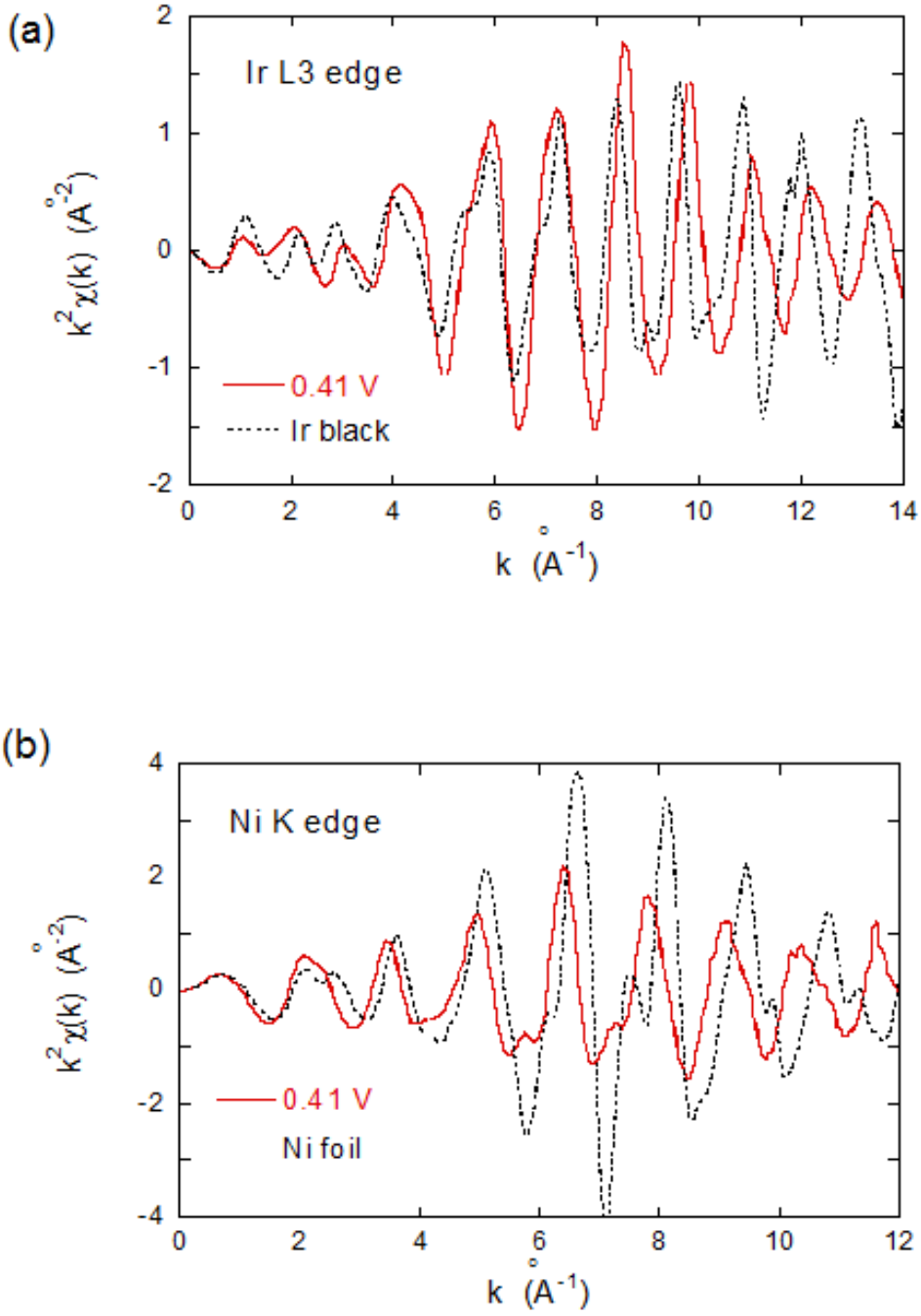

Figure3.9. *In situ* EXAFS k-space spectra (k^2-weighted) of (a) Ir L3 edge and (b) Ni K edge obtained from IrNi nanoparticles in 1M $HClO_4$ at 0.41 V/RHE. Also shown are spectra from (a) Ir black and (b) Ni foil.

Figure 3.9 depicts the k^2-weighted EXAFS spectra of the Ir L3 and Ni K edges from the IrNi nanoparticles in 1 M $HClO_4$ at a potential of 0.41 V/RHE, together with those from their respective reference foils. Differences are very apparent in oscillation behavior in the k-space of the nanoparticles and their reference materials in Figures 3.9(a) and (b), indicating that the atomic structures surrounding both Ir and Ni in the IrNi nanoparticles are significantly different from those in their 3D bulks.

The difference also is apparent in the Fourier transformed spectra (Figures 3.10(a) and (b)). The highest peak in Ni from the IrNi nanoparticles is shifted to a higher *r* compared with that from the Ni foil, while the highest peak in Ir from the IrNi nanoparticles is displaced to a lower *r* than that from the Ir black. These figures represent the expansion in the Ni-metal (M) bonds and the contraction in the Ir-M bonds as a consequence of the formation of IrNi solid solution alloy cores; the result is in line with those obtained from the XRD measurements (Figure 3.5) and the EXAFS fitting as discussed below. The EXAFS spectra of Ni K edge from the IrNi nanoparticles at potentials of 0.71, 0.91, 1.11 V/RHE also are illustrated in Figure 3.10(b). Little change occurs with increasing potentials, and no characteristic signature of Ni oxides and/or Ni ions is seen, even at the high potentials. As per the Pourbaix diagrams,[142] Ni cannot be present as a metallic state when exposed to acid solutions, unless the potential applied is below -0.4 V. The experimental result from the *in situ* EXAFS indicates that Ni atoms constituting the IrNi cores are not exposed to the electrolyte since the Ir shell completely encapsulates the IrNi core; Ni in the IrNi solid solution cores therefore is protected from oxidation or corrosion.

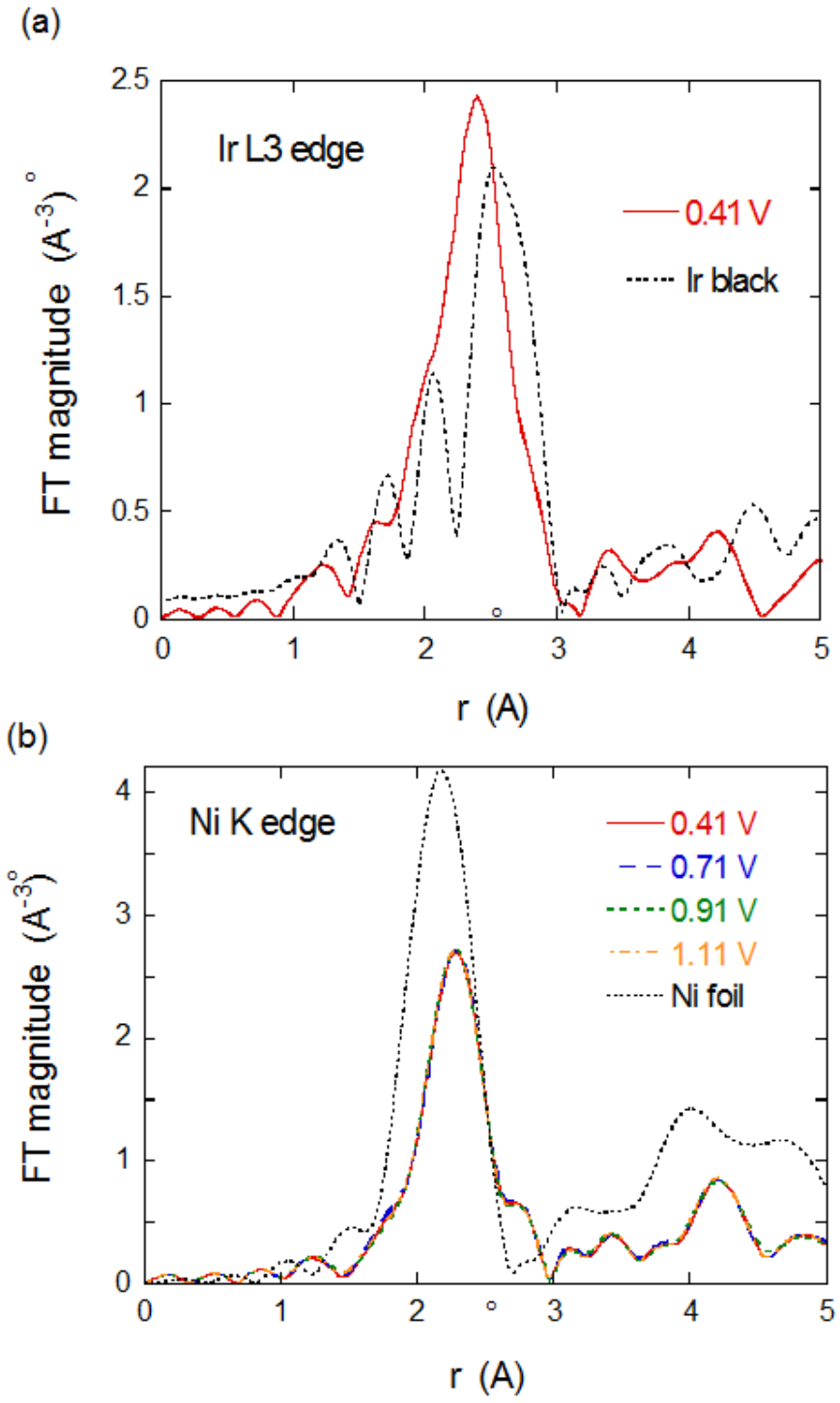

Figure3.10. *In situ* EXAFS Fourier transformed magnitudes of (a) Ir L3 edge and (b) Ni K edge obtained from IrNi nanoparticles in 1M $HClO_4$ at 0.41 V/RHE for (a), and 0.41, 0.71, 0.91, and 1.11 V/RHE for (b). Also shown are spectra from (a) Ir black and (b) Ni foil.

The Ir L3 and Ni K edge data were fitted concurrently with the passive electron reduction factors ($S_0^2{}_{Ir}$ and $S_0^2{}_{Ni}$) equal to those determined from fitting the Ir black and Ni metal foil data (0.81 and 0.82, respectively). The following constraints were applied: (i) The Ir-Ni bond distance is the same as measured from either edge (i.e., $R_{Ir\text{-}Ni} = R_{Ni\text{-}Ir}$,): (ii) the bond length disorder parameters of heterogeneous metal bonds are the same as measured from opposite atoms (i.e., $\sigma^2_{Ir\text{-}Ni} = \sigma^2_{Ni\text{-}Ir}$): (iii) the ratio of coordination numbers ($N_{Ir\text{-}Ni}/N_{Ni\text{-}Ir}$) reflects the actual molar fractions of the metals (x_{Ni}/x_{Ir}) determined as 0.56 by the EDX analysis: and, (iv) the total coordination numbers ($N_{Ir\text{-}M}$ and $N_{Ni\text{-}M}$) with a diameter of 4.7 nm are 11, as shown by modeling the core-shell nanoparticle (i.e. $N_{Ir\text{-}Ir} = 11 - N_{Ir\text{-}Ni}$ and $N_{Ni\text{-}Ni} = 11 - N_{Ni\text{-}Ir}$). Figure 3.11 displays the fitting results of the Ir-Ni nanoparticles. Good agreement is given between the fits and the original spectra for both Ir L3 (Figure 3.11(a)) and Ni K (b) edges.

	$N_{Ir\text{-}Ir}$	$N_{Ir\text{-}Ni}$	$N_{Ni\text{-}Ni}$	$N_{Ni\text{-}Ir}$	$N_{Ir\text{-}Ni} / N_{Ni\text{-}Ir}$	$N_{Ni\text{-}Ni} / N_{Ni\text{-}Ir}$
EXAFS	8.2 ± 0.7	2.8 ± 0.7	6.0 ± 0.7	5.0 ± 0.7	0.56	1.2 ± 0.7
1 Ir layer	6.47	3.76	5.28	6.72	0.56	0.79
2 Ir layers	7.82	2.42	7.69	4.31	0.56	1.78

Table3.1. Coordination numbers determined by the EXAFS experiment, and 1 Ir layer and 2 Ir layers models.

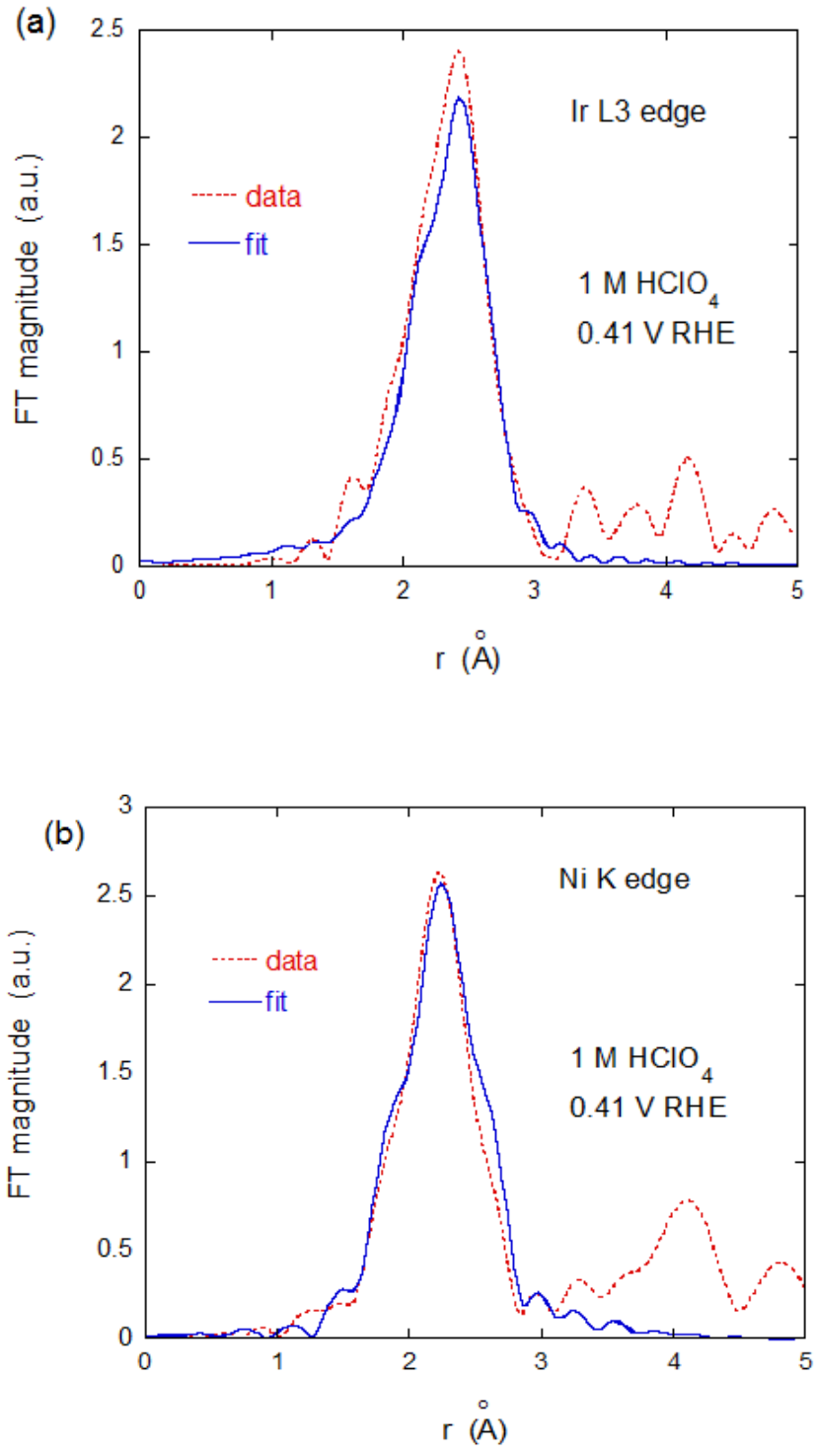

Figure3.11. Fourier transform magnitudes of the data (dotted red) and first-shell fit (solid blue) of (a) Ir L3 and (b) Ni K edges from IrNi nanoparticles in 1M $HClO_4$ at a potential of 0.41 V/RHE.

Table 3.1 and 3.2 summarizes the coordination numbers for 1 Ir layer and 2 Ir layers models obtained and bond distance R and bond length disorder parameter σ^2 respectively determined by EXAFS experiment. The Ir-Ir, Ir-Ni (the same as Ni-Ir) and Ni-Ni bond lengths are 2.664 ± 0.006 Å, 2.594 ± 0.007 Å, and 2.562 ± 0.014 Å, respectively. It should be noted that the length of the Ir-Ir bond is less than that of pure Ir (2.714 Å), while the Ni-Ni bond is longer than that of pure Ni (2.492 Å), indicating their alloying.

	R (Å)	σ^2 (Å^2)
Ir-Ir	2.664 ± 0.006	0.0055 ± 0.0003
Ir-Ni (Ni-Ir)	2.594 ± 0.007	0.0037 ± 0.0012
Ni-Ni	2.562 ± 0.014	0.0091 ± 0.0017

Table3.2. Other structural parameters (bond distance R and bond length disorder parameter σ^2) determined by the EXAFS experiment.

The interpretation of the coordination numbers obtained is not straightforward since they are the ensemble-average values from both the shells and cores, except for $N_{\text{Ni-Ni}}$ that is derived only from the cores. For an A-B binary solid-solution alloy, the ratio (relative to the A atom) of the coordination number $N_{A\text{-}A}$ to $N_{A\text{-}B}$ is equal to the mole fraction ratio x_A/x_B of the elements in the bulk,[143] i.e., $N_{A\text{-}A} / N_{A\text{-}B} = x_A / x_B$. As listed in Table 3.1, the ratio of coordination numbers $N_{\text{Ni-Ni}} / N_{\text{Ni-Ir}}$ is 1.2, which is much larger than the actual mole fraction ratio $x_{\text{Ni}}/x_{\text{Ir}} = 0.56$. This finding indicates that more Ni-Ni bonds (and fewer Ni-Ir bonds) are present than in a random alloy wherein the two atoms have a homogeneous distribution; this finding is well consistent with the STEM observations showing the Ir-rich (or Ni-depleted) shells; in the cores the number of Ni-Ni bonds should be larger than on the average.

A suite of programs that model polyhedral nanoparticles with different diameters, different Ir shell thicknesses, and different molar ratios of IrNi cores to calculate the atomic coordination numbers for various core-shell structures were used. [144-145] Then the coordination numbers in the model with those from the EXAFS analysis were compared in order to determine the most suitable core-shell structure. Table 3.1 also lists the calculated coordination numbers from two core-shell models; one comprises 1 shell layer of Ir (812 atoms) on an IrNi alloy core (1027 Ni and 1030 Ir atoms), while the other represents 2 shell layers of Ir (1454 atoms) on an IrNi alloy core (1030 Ni and 385 Ir atoms). Ir and Ni atoms in the cores are randomly alloyed via a random number generator. For both models, the atomic ratio of Ni/Ir was set at 0.56, the diameter was calculated as 4.68 nm, and the average (metal-metal) coordination numbers were estimated to be 11. The 2 layer model fits the most of the EXAFS data much better cumulatively than does the 1 layer model. Thus, the EXAFS analysis is consistent with the model wherein the IrNi nanoparticles are composed of 2-layer Ir shells and IrNi alloy cores, as schematically shown in Figure 3.12.

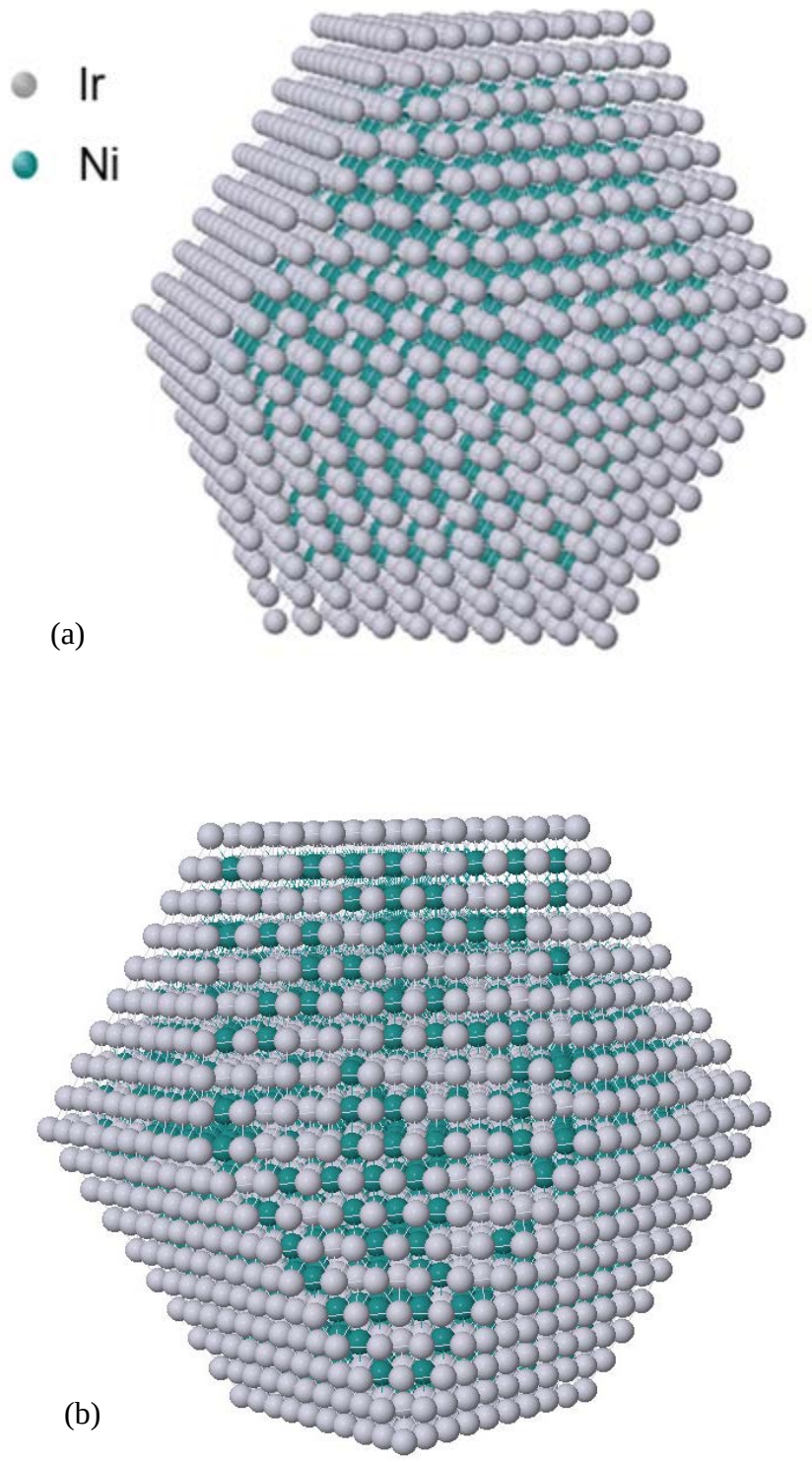

Figure3.12. (a) Atomic configuration of 2 shell layers of Ir (1454 atoms) on IrNi alloy core (1030 Ni and 385 Ir atoms), and (b) atomic configuration of 1 shell layer of Ir (812 atoms) on IrNi alloy core (1027 Ni, 1030 Ir). Ir: grey spheres. Ni: green spheres

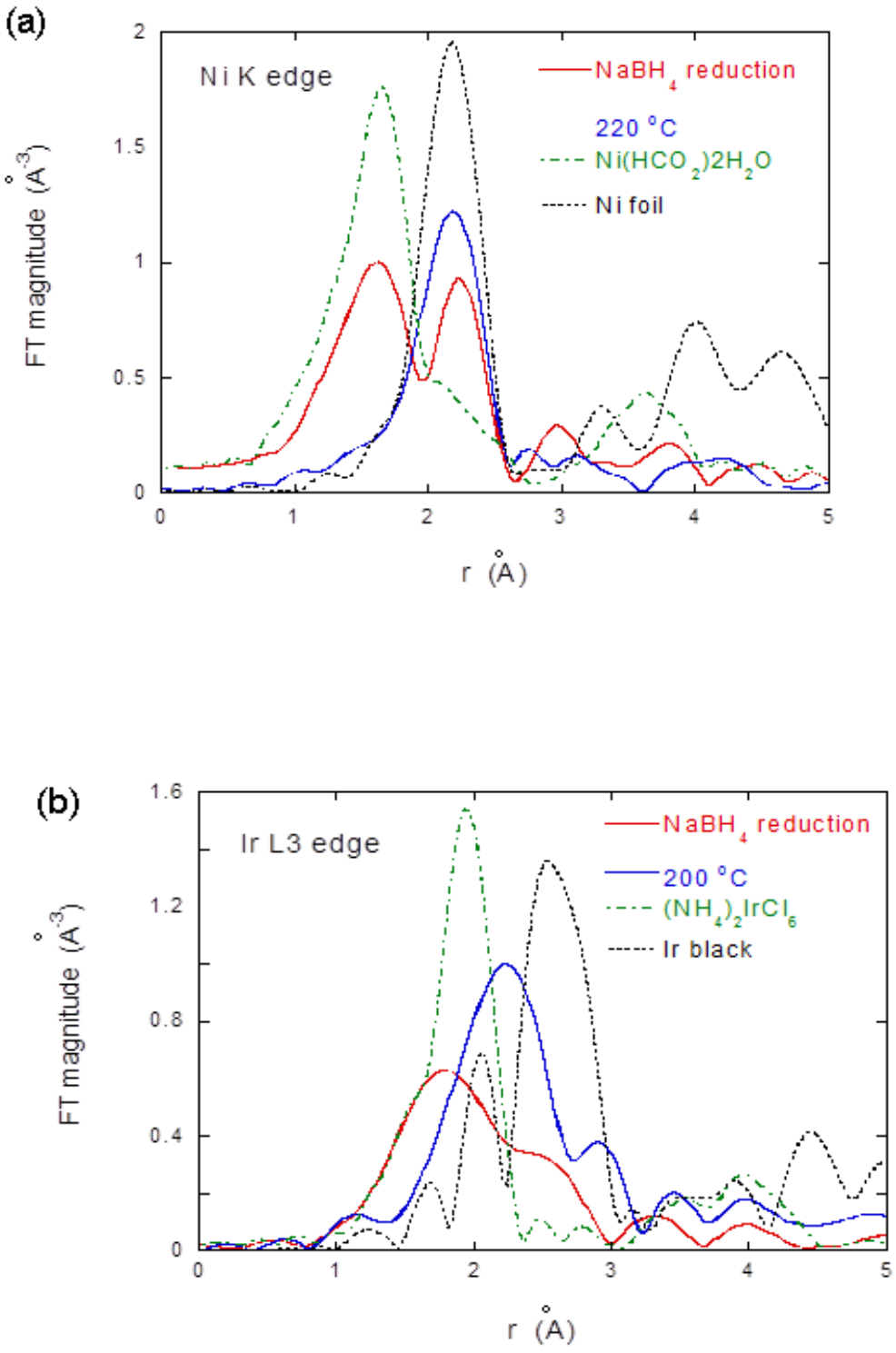

Figure3.13. Fourier transformed magnitudes of EXAFS spectra of (a) Ni K and (b) Ir L3 edges from the IrNi nanoparticles before (reduced only by $NaBH_4$ but not annealed in H_2 atmosphere) and after annealing in H_2 atmosphere at given temperatures (220 ºC and 200 ºC, respectively) using a thermal XAS cell. Also shown is those from the precursors ($(NH_4)_2IrCl_6$ and $Ni(HCO_2)\cdot 2H_2O$, respectively), and the reference materials (Ni foil and Ir black).

To understand the effect of thermal treatment on the formation of IrNi solid solution, *in situ* thermal XAS was carried out. Figure 3.13 shows the Fourier transformed EXAFS spectra of the (a) Ni K and (b) Ir L3 edges from the IrNi nanoparticles before and after annealing in H_2 atmosphere at given temperatures (220 ºC and 200 ºC, respectively) using the thermal XAS cell. (The nanoparticles were reduced only by $NaBH_4$ but were not annealed in the H_2 atmosphere before these measurements.) Also shown in the figure is spectra from the precursors ($Ni(HCO_2)\cdot 2H_2O$ and $((NH_4)_2IrCl_6)$, and the reference materials (Ni foil and Ir black). The Fourier transformed EXAFS spectrum of Ni K edge from the un-annealed sample (red curve in Fig. 3.13(a)) has two prominent peaks at 1.62 Å and 2.23 Å. The former is likely to be due to the presence of Ni^{2+} because of its similarity of that from $Ni(HCO_2)\cdot 2H_2O$ (green dot-dash curve), while the latter is considered to originate from metallic Ni considering from its resemblance of that from Ni foil (black dot curve). This result implies that the $NaBH_4$ treatment occasions only a partial reduction of Ni. However, the peak due to Ni^{2+} disappears while the Ni metallic peak grows, as shown in the spectrum from the sample annealed at 220ºC in the H_2 atmosphere (blue curve), indicating the complete reduction of all Ni atoms at this temperature. Similarly, Figure 3.13(b) shows a partial reduction of Ir in the IrNi nanoparticles before annealing and its full reduction by thermal annealing at 200°C (blue curve).

3.2.3 Time Resolved XRD study of Ni-Ir Core-Shell nanoparticles

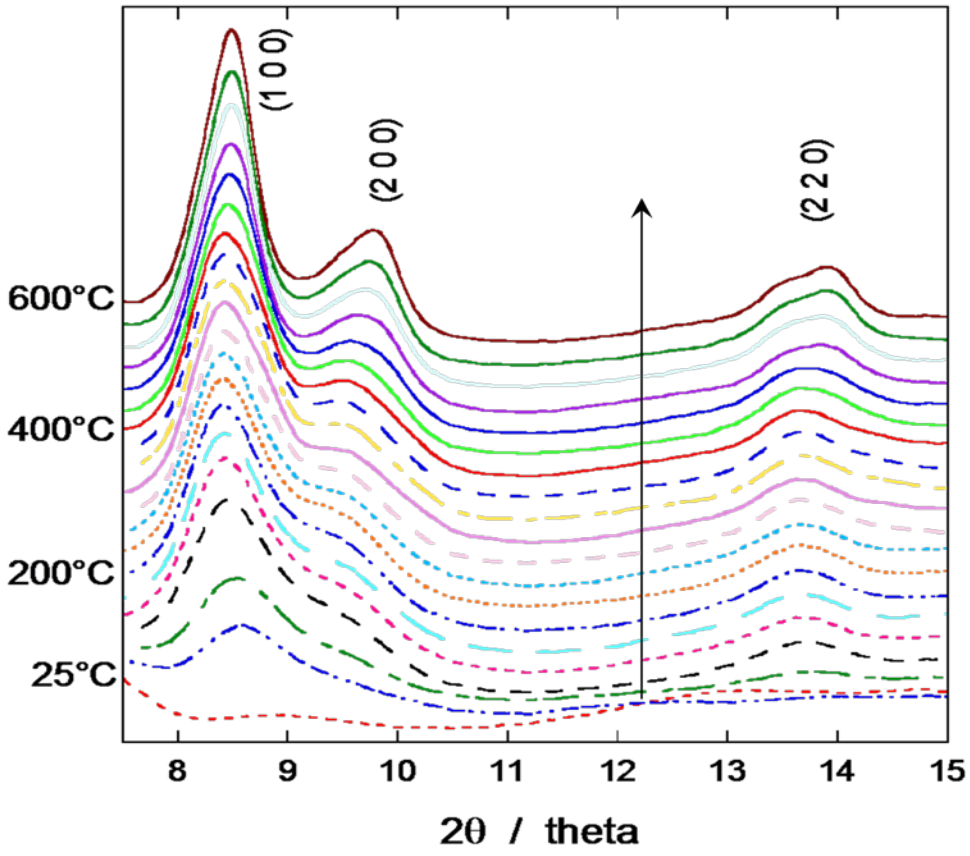

Figure3.14. *In situ* time-resolved XRD patterns (the wavelength: 0.3184 Å) obtained from the IrNi nanoparticles (reduced only by $NaBH_4$ before the test) during reduction in 5% H_2/He flow at increasing temperatures (a heating rate of 4.8 °C/min).

Figure 3.14 depicts the *in situ* time-resolved XRD patterns collected during the annealing process (the wavelength: 0.3184 Å); the IrNi/C sample reduced only by $NaBH_4$, was loaded into a quartz reactor and annealed from room temperature up to 600°C with a flow of 5%H_2/He gas mixture. No prominent diffraction peaks were observed at room temperature (dashed red curve), indicating that the initial sample had no long-range ordered structure; rather, it has partially reduced Ir and Ni, as shown in Figure 3.13, which must form small clusters with short-range

atomic order. However, as temperature increases (designated by the arrow in the figure) three diffraction features appear, and the peaks become more intense as the temperature rises.

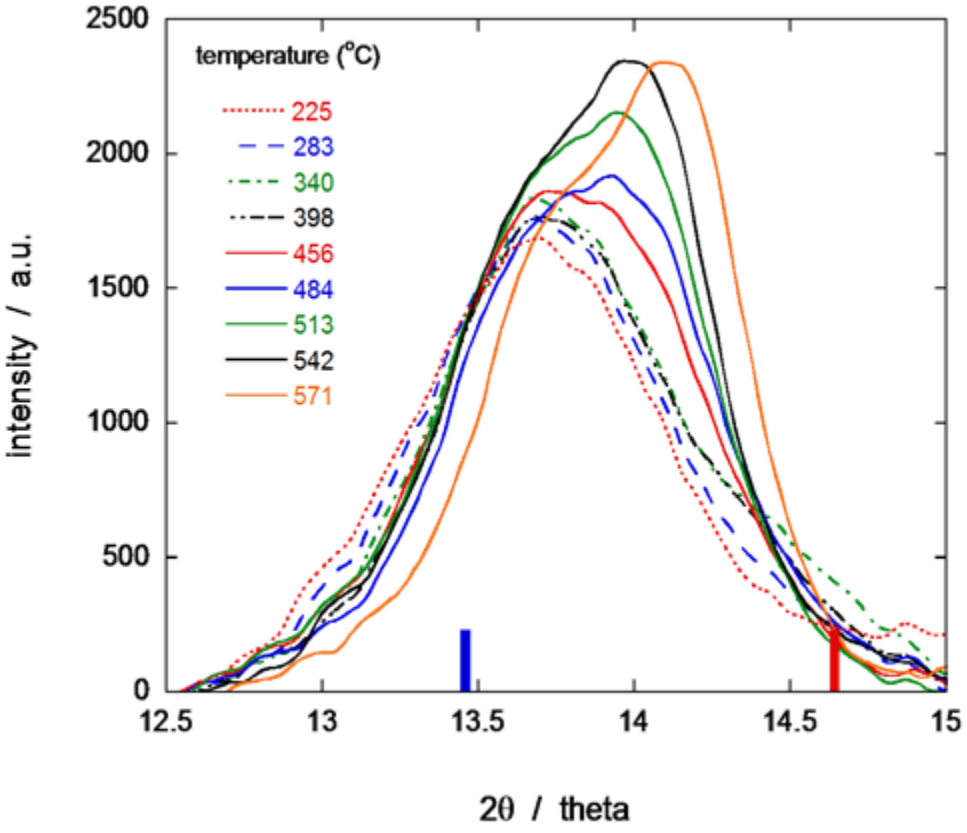

Figure3.15. Details of *in situ* time-resolved XRD patterns obtained from the IrNi nanoparticles between (2θ =) 12.5° and 15° at annealing temperatures from 225°C to 571°C. Blue and red bars designate a (220) reflection from pure Ir and Ni, respectively.

Figure 3.15 illustrates details of the *in situ* XRD patterns between (2θ =) 12.5° and 15° at annealing temperatures from 225°C to 571°C.[‡] As demonstrated in Fig. 3.13, both Ir and Ni in

[‡] With an increase in temperature the XRD peak positions shift to lower angles due to an increase in thermal expansion of lattice. Assuming that the thermal expansion with elevating temperature is linear, the peak positions were corrected in Figure 3.14 as well as the lattice constants in Figure 3.15.

the IrNi sample must have been fully reduced up to 220 °C. Although the observed peaks lie between the reflections from Ir(220) (2θ = 13.47°, indicated by the blue bar) and Ni(220) (2θ = 14.681°, indicated by the red bar) during the annealing temperature range, two features are noticeable. One is that the peak, as a whole, shifts toward a higher angle with increasing temperature. This phenomenon can be rationalized as reflecting the progress in IrNi solid solution alloying; Ni atoms diffuse into the Ir clusters, yielding a more homogeneous mixture of IrNi solid solution alloy. The other is the development of asymmetry in the peak; a ramp on the right-hand side of the peak begins to grow with an increase in temperature, particularly above 456 °C. This is likely to result from the enrichment of Ni in the IrNi solid-solution alloy cores and the segregation of Ir on the core surfaces, induced by elevating temperatures.

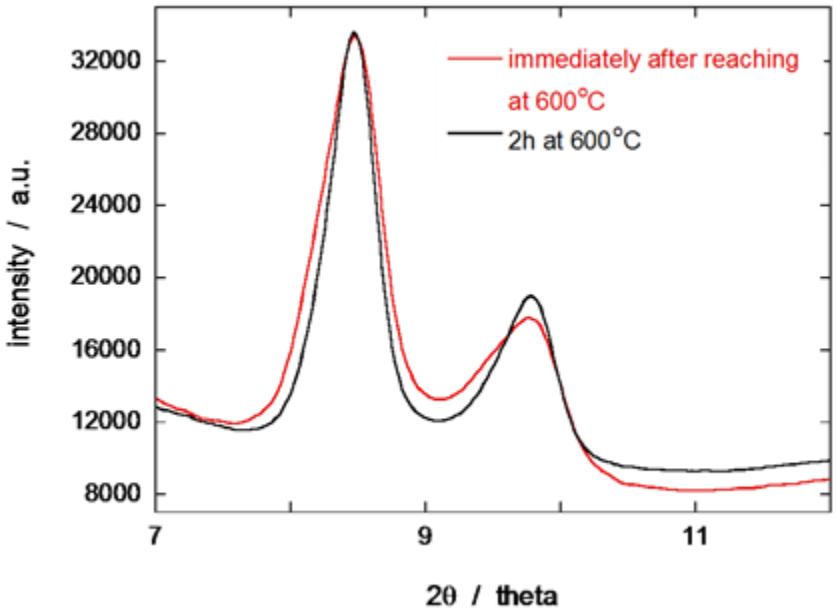

Figure3.16. Changes in peak position observed on *in situ* time-resolved XRD patterns from the IrNi nanoparticles immediately after reaching at 600°C (red curve) and after 2 hrs. at 600°C (black curve).

When the temperature reached 600°C in the quartz reactor, we maintained it constant for 2 hours. The peak position did not change but its width decreased during these 2 hours (Figure 3.16). This finding demonstrates that the core-shell structure basically does not change, while the particles keep growing at 600°C. After 2hr annealing at 600°C, the particle size was 4.7 nm, i.e., identical to that examined by the XRD measurement with Cu Kα.

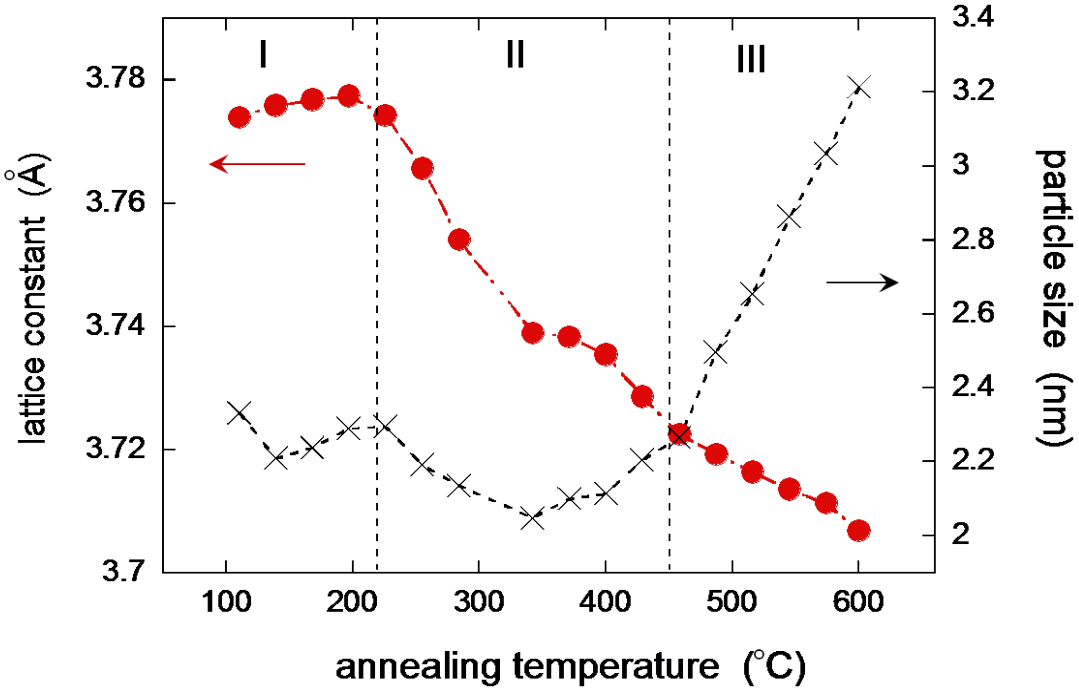

Figure3.17. Rietveld refinement analyses showing changes in cell dimension and particle size of the IrNi nanoparticles as a function of annealing temperatures.

The Rietveld refinement analyses were used to follow the changes in the cell dimension and particle size with annealing temperature (Figure 3.17). It was found that up to 220°C the cell dimension of IrNi sample is approximately constant at 3.775 Å. This value is smaller than that of pure Ir metal (3.839 Å), but much larger than that of Ni metal (3.524 Å), pointing to the formation of Ir-rich clusters in the nanoparticles. The temperature region up to 220°C was

designated as Regime I. Figure 3.18 illustrates a schematic of the IrNi nanoparticle containing Ir-rich clusters in this Regime. Above 220°C, the cell dimension starts to decline considerably with rising temperatures. The region between 220°C and 450°C was termed as Regime II. This cell contraction likely reflects further alloying of Ni with the Ir-rich clusters, generating in a more homogeneous IrNi alloy nanoparticle (Figure 3.18). From the Rietveld refinement the particle size was also estimated, which is shown as a function of temperature in Figure 3.17. The particle size remains approximately constant (*ca* 2.2 nm) up to 450°C; thereafter, the particles start to grow up to 600°C. The region between 450°C and 600°C was designated as Regime III. It is considered that the neighboring nanoparticles may migrate and coalesce on carbon supports above 450 °C. Intriguingly, this onset temperature is almost coincident with that of the asymmetry in peak shape (Figure 3.15) that is caused by the segregation of Ir atoms on the nanoparticle surfaces. Likely, long-range atomic diffusion occurs above 450°C, and therefore, induce the segregation of Ir to the particle surfaces as well as the growth of the particles, while below 450°C, atomic diffusion is confined to short-range order, presumably by the place-exchange mechanism. The formation of Ir shell on IrNi alloy core in Regime III also is illustrated schematically in Figure 3.18. As the EXAFS analysis revealed, the nanoparticles will eventually comprise the 2 layers of Ir on the IrNi alloy cores by thermal annealing at 600°C.

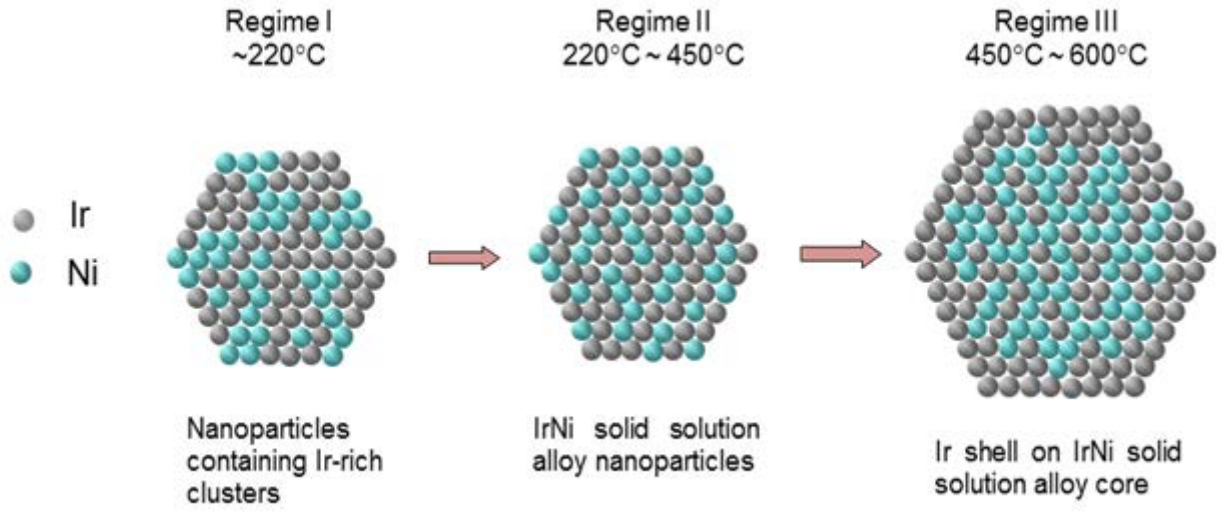

Figure3.18. Schematics of changes in atomic structure of IrNi nanoparticles with increasing temperatures.

3.2.4 ORR measurements on Pt_{ML} IrNi nanoparticles

Fig. 3.19 shows rotating disk electrode (RDE) measurements of the ORR on the Pt_{ML} IrNi/C electrocatalyst, made by RDE synthesis method, in a 0.1M $HClO_4$ solution purged by O_2 at different rotation speeds (400–3025 rpm) and scanned at a rate of 10mV/sec. The activity of the electrocatalyst is significant, as indicated by the half wave potentials (890mV at a rotation rate of 1600rpm). Using the polarization curves, the inverse current density ($1/j$) (figure 3.20) was plotted as a function of the inverse of the square root of the rotation rate ($\omega^{1/2}$), also known as Koutecky–Levich plot. The kinetic currents for ORR can be determined from the intercepts of the $1/j$ axis at $\omega^{1/2} = 0$. The Pt mass activity of the Pt_{ML} IrNi/C electrocatalyst is 1.4 A/mg_{Pt} at 0.9 V/RHE, which is approximately 6 times higher than that of the commercial Pt/C electrocatalyst. The platinum group metal mass activity is 0.78 A/mg_{PGM} at 0.9V/RHE which is also higher than the 2015 DOE target (0.44 A/mg_{Pt}). [146] Table3.3 compares the mass activities and specific

activities of Pt/C (4nm), Pt_{ML} Ir/C and Pt_{ML} IrNi/C nanoparticles. The Pt specific activities of the Pt_{ML}/IrNi/C, Pt_{ML}/Ir/C, and Pt/C electrocatalysts at 0.9 V/RHE are 0.60, 0.13, and 0.24mA/cm^2, respectively. Figure 3.21 compares the currents obtained during the ORR in the anodic sweep cycle on the Pt_{ML}/IrNi/C, Pt_{ML}/Ir/C and Pt/C (E-tek 20%) electrocatalyst at 1600 rpm in 0.1M $HClO_4$ solution. The diffusion current for Pt/C (10 μg/cm^2 (10 nmol) Pt loading) is almost comparable to Pt_{ML}/Ir/C (3.6 μg/cm^2 Pt). So adding a Pt monolayer on Ir nanoparticles does not improve the ORR activity. Moreover alloying Ni with Ir (Pt_{ML}/IrNi/C) one can clearly observe the increases in diffusion current and activity for ORR. This enhancement in activity may be due to electronic modifications induced by strain and ligand and segregation effects in bimetallic surfaces. It has always been difficult to separate the role of strain and ligand effects in ORR activity enhancements as both plays a cumulative effect on the modification of chemical properties of these surfaces. [147]

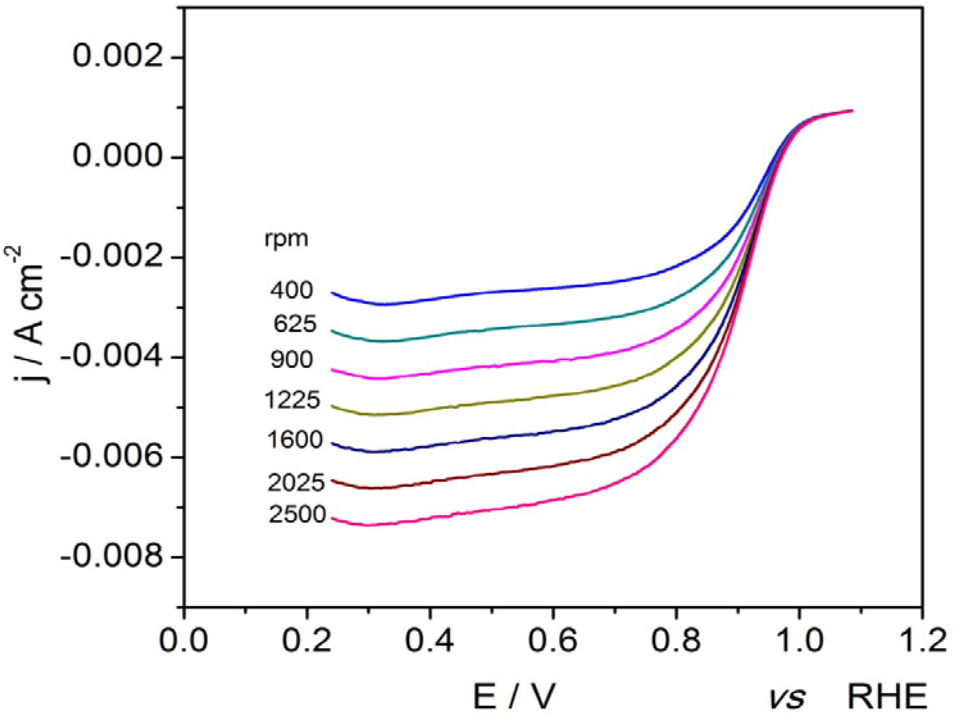

Figure3.19. Polarization curves for the ORR on $Pt_{ML}IrNi/C$ nanoparticles electrocatalysts at various rpm in oxygen-saturated 0.1 M $HClO_4$.

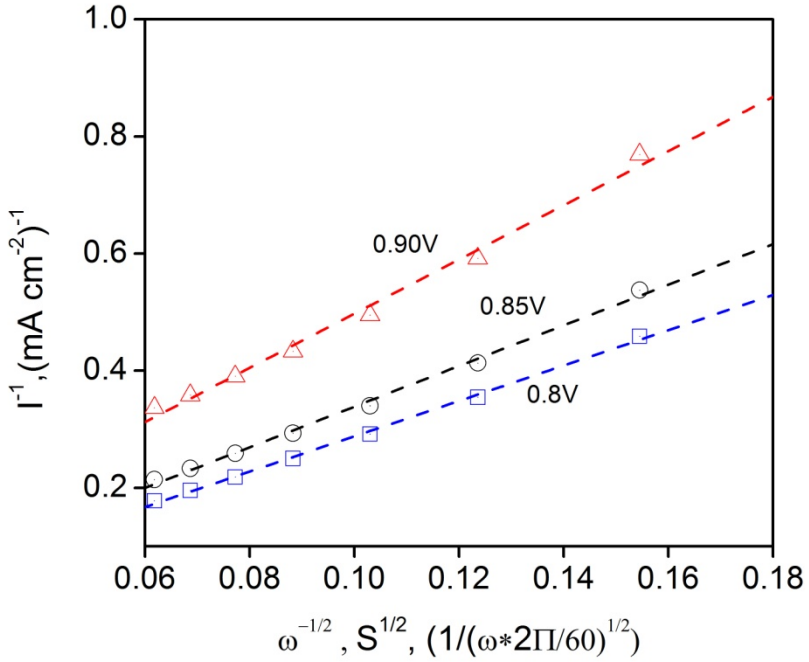

Figure3.20. Levich-Koutecky plots at various potentials for $Pt_{ML}IrNi/C$ nanoparticles electrocatalysts

Pt_{ML}/IrNi/C (RDE synthesized)			Pt_{ML}/Ir/C (RDE synthesized)		Commercial Pt/C (4 nm)	
Pt mass activity (j / A mg_{Pt}^{-1})	PGM mass activity (j /A mg_{PGM}^{-1})	Specific activity (j / mA cm^{-2})	Pt mass activity (j/A mg_{Pt}^{-1})	Specific activity (j/mAcm^{-2})	Pt mass activity (j/A mg_{Pt}^{-1})	Specific activity (j/mAcm^{-2})
1.4	0.78	0.60	0.33	0.13	0.20	0.24

Table3.3. Pt Mass and Specific Activities of Pt/C (4nm), Pt_{ML} Ir/C and Pt_{ML} IrNi/C electrocatalyst at 0.90 V/RHE

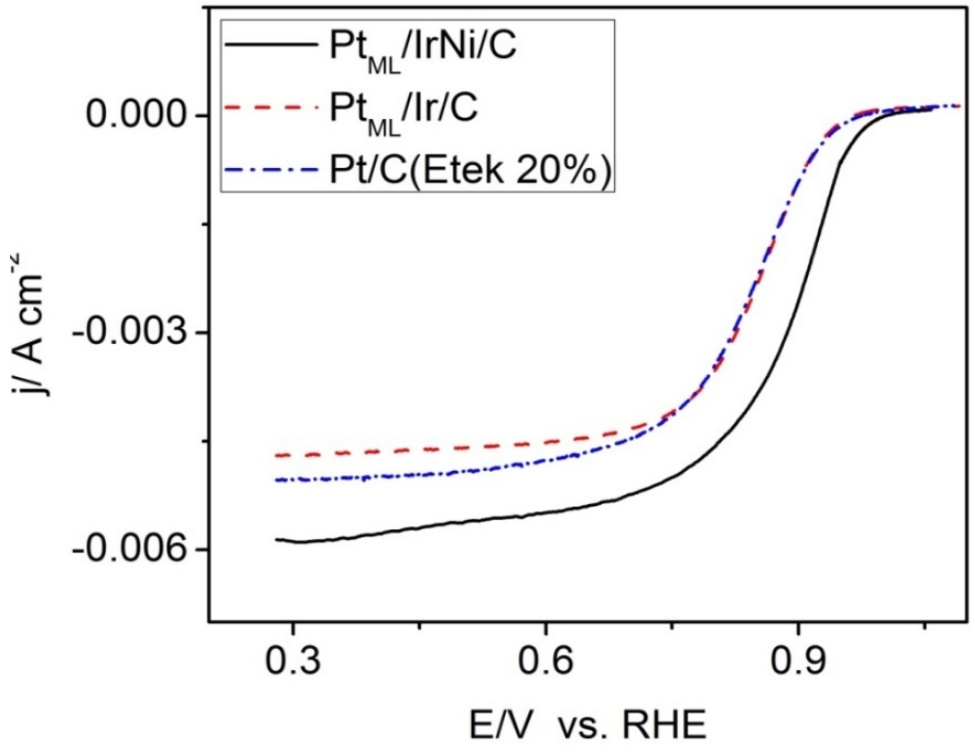

Figure3.21. Polarization curves for the ORR on thin-film electrodes of the Pt_{ML}/IrNi/C and Pt_{ML}/Ir/C and Pt/C (E-tek 20%) nanoparticles electrocatalysts at 1600 rpm in oxygen-saturated 0.1 M $HClO_4$.

3.2.5 Durability testing on RDE

The long-term stability of the ORR electrocatalysts is another critical requirement for applying them in fuel cells. The stability of the Pt monolayer electrocatalyst was evaluated by cycling in an air-saturated $HClO_4$ solution at 0.6V and 1.0V/RHE at a scan rate of 50mV/sec. Voltammetry was used to determine the Pt surface area of the electrodes by measuring H adsorption before and after potential cycling. Integrating the charge between 0 and 0.33 V associated with H adsorption for Pt_{ML} IrNi/C shows a small loss of Pt surface area. A decrease in H adsorption and desorption charges was observed after the potential cycling test compared with the one before cycling as shown in figure 3.22(a). The Pt_{ML} IrNi catalyst made by the RDE synthesis method showed a 45% loss in the surface area and 18mV loss in half-wave potential after 30,000 cycles (figure 3.22 (b)). The degradation in the ORR observed for the Pt_{ML} IrNi/C electrocatalyst is smaller compared with a commercial Pt electrocatalyst, which showed a negative shift of 40 mV in half wave potential and a loss of approximately 45% in Pt surface area. [148]

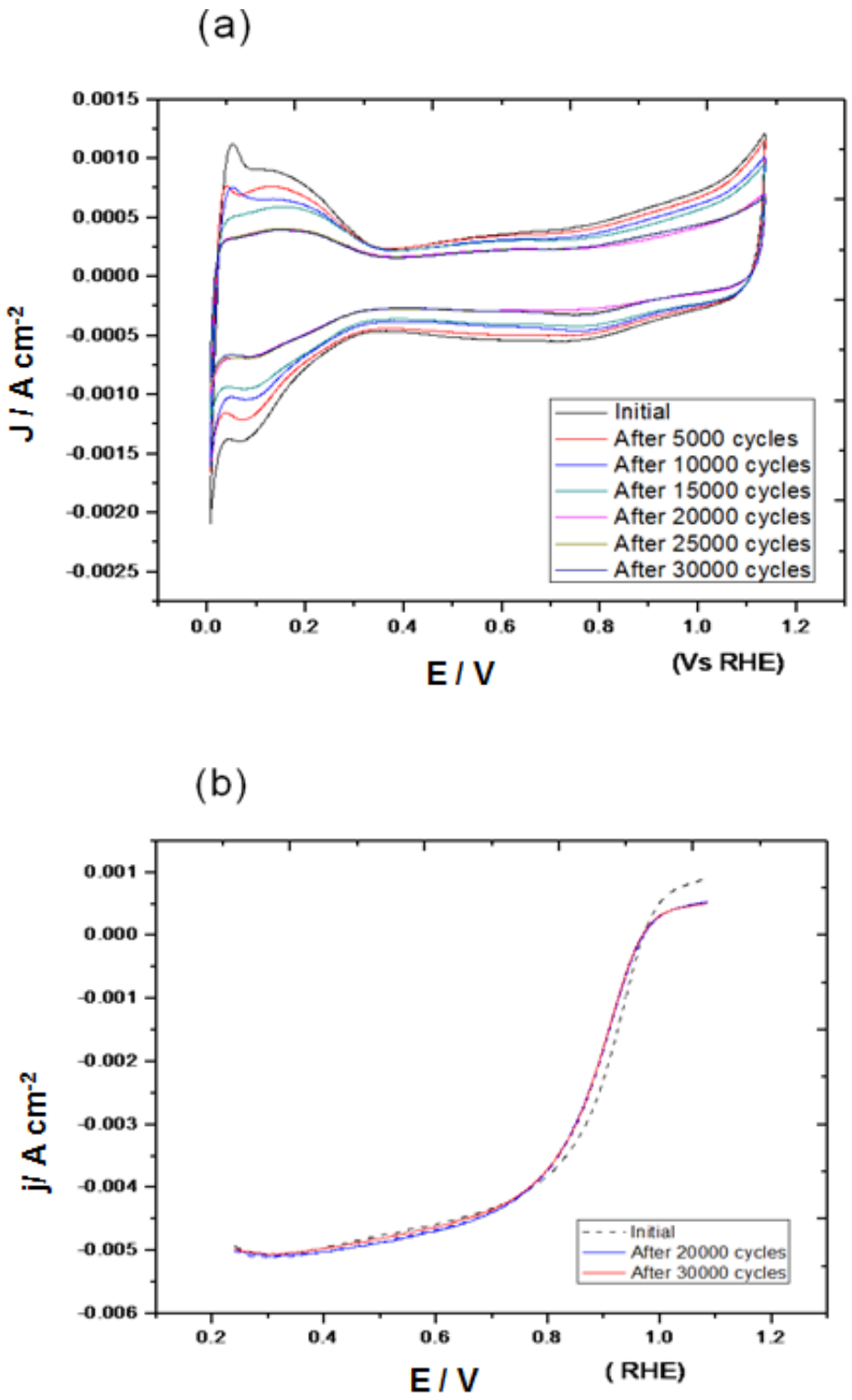

Figure3.22. (a) Cyclic voltammetry for Pt_{ML} IrNi/C in Ar-saturated 0.1 M $HClO_4$ (b) Polarization curves for the ORR at 1600 rpm in oxygen-saturated 0.1 M $HClO_4$, after various potential cycles

3.2.6 Summary and Discussion

Carbon supported IrNi core-shell structured nanoparticles were synthesized by chemical reduction, followed by thermal annealing. XRD, STEM-EELS and *in situ* XAS study has revealed the structure of IrNi nanoparticles as Ir shell on the IrNi alloy. The EXAFS analysis is consistent with the model which suggests that the IrNi nanoparticles are composed of two-layer Ir shells and IrNi alloy cores. In situ XAS studies for IrNi core-shell nanoparticles show Ir-Ir bond is contracted and Ni-Ni bond is expanded. In situ XAS and EELS studies show that Ir shells completely protect Ni atoms in cores from oxidation and dissolution. Time-resolved synchrotron XRD measurements combined with Rietveld refinement analyses demonstrated the progress of reaching a solid solution alloy of Ir and Ni atoms during thermal annealing above 220ºC, and the onset of Ir segregation on the IrNi core surfaces above 450°C.

It has been widely reported that the phenomenon of surface segregation is primarily determined by the surface energy and atomic size of alloy constituents. [149] Metal atoms having larger radii and lower surface energies usually tend to segregate to the surface. The experimental surface energies for Ir and Ni are 3.000 J m^{-2} and 2.450 J m^{-2}, [150] and the metallic radii for Ir and Ni are 1.36 Å and 1.24 Å,[151] respectively. The Ir segregation for the present IrNi system can be predicted from the difference in radii but cannot be explained in terms of surface energies. It is known that Pt atoms tend to segregate to the surfaces of Pt-Ni system [152]; the radius of Pt (1.39 Å) is much larger than that of Ni while the surface energy of Pt (2.475 J m^{-2}) is almost comparable to that of Ni. This implies that the difference in atomic size is an important factor for the PtNi system; the segregation of Pt atoms to the surface alleviates strain in the alloy significantly, resulting in a decrease in the total energy. [149] A similar rationale may be applied to the Ir segregation for the IrNi system.

We also demonstrated the formation of a new class of core-shell electrocatalysts for the ORR, consisting of a Pt monolayer shell and bimetallic IrNi core. Thus, we coupled highly stable, inexpensive core-shell nanoparticles with a Pt monolayer to produce electrocatalysts with high activity and high stability. The Pt mass activity of the RDE synthesized Pt_{ML} IrNi/C electrocatalyst is 1.4 A/mg_{Pt} at 0.9 V/RHE, which is approximately 6 times higher than that of the commercial Pt/C electrocatalyst and around 4 times higher than Pt_{ML} on Ir nanoparticles. The resulting electrocatalyst is cost-effective, providing a way of using Pt that can resolve key ORR problems.

3.3 Compositional Optimization of Carbon supported IrNi nanoparticles

The Pt_{ML} placed on IrNi nanoparticles with core-shell structures shows about four or five times higher Pt mass activity than the state-of-the-art Pt catalysts, demonstrating the potential of Pt_{ML} approach for resolving the problem of high Pt content. Reducing the amount of noble metal in the substrate for the Pt monolayer without much reducing the activity would be a much better milestone and a step closer to make fuel cells cheaper. We synthesized different sets of IrNi alloy samples reducing the Ir concentration and examined its ORR activity. The molar ratios mentioned in this section are calculated from the amount of precursors added while preparing the samples. It was observed that reducing the Ir content and annealing the mixture at 600°C increases the particle size of the IrNi alloy which in turn reduces the ORR activity. This could be observed in the XRD pattern and polarization curves for ORR for $Ir_{40}Ni_{60}$ alloy nanoparticles annealed at 600°C.

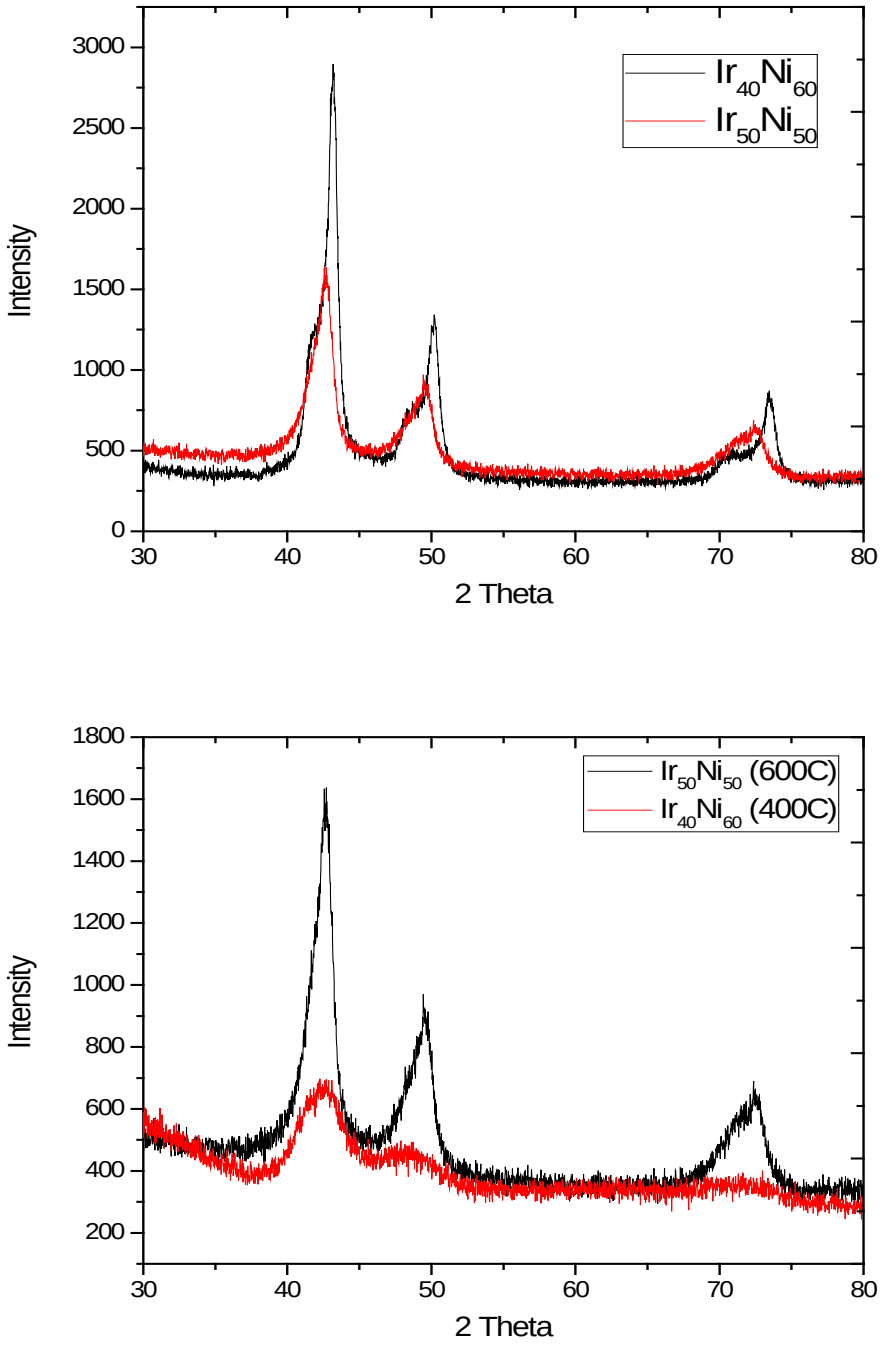

Figure3.23. (a) XRD pattern of carbon supported $Ir_{40}Ni_{60}$ and IrNi nanoparticles with Cu Kα radiation after annealing at 600°C in H_2 atmosphere for 2 h. (b) XRD pattern of carbon supported $Ir_{40}Ni_{60}$ annealed at 400°C along with IrNi nanoparticles annealed at 600°C

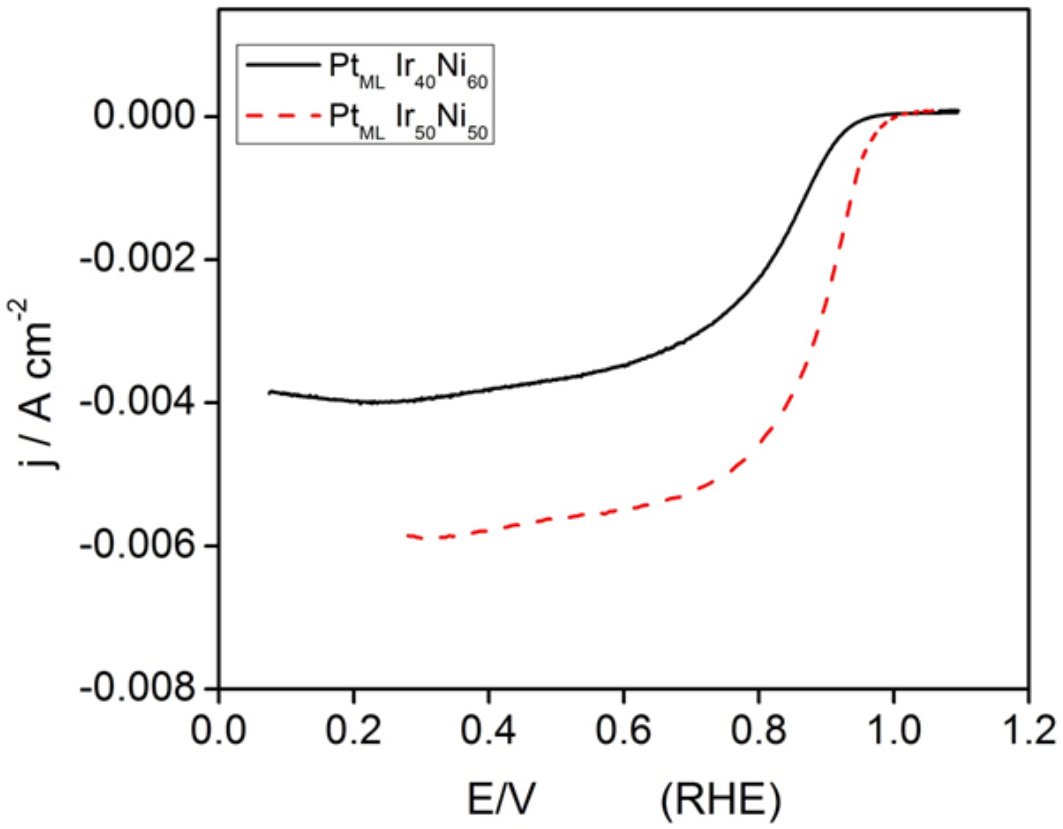

Figure3.24. Polarization curves for the ORR on $Pt_{ML}Ir_{40}Ni_{60}$/C nanoparticles (solid red line) electrocatalysts and Pt_{ML} IrNi/C nanoparticles (dotted black line) annealed at 600°C in oxygen-saturated 0.1 M $HClO_4$ at 1600 rpm.

Figure 3.23(a) shows the XRD pattern measured from the $Ir_{40}Ni_{60}$/C nanoparticles and compared with IrNi/C nanoparticles using Cu Kα radiation (1.54056 Å). There are three pronounced reflection peaks but all of them shifted to higher angles when compared to IrNi nanoparticles. No separate peaks for Ir or Ni were observed similar to that of IrNi nanoparticles which points to the formation of IrNi solid-solution alloy nanoparticles with an average particle size of 8.1 nm, estimated from Scherer's equation. The particle size increases almost two times more when the Ir concentration is reduced by just 20%, is a bad factor for ORR as shown in figure 3.24. The 54mV decrease in half wave potential when compared to Pt_{ML} IrNi/C

nanoparticles is due to the lower Ir content in the alloy. To analyze the annealing temperature factor, XRD and electrochemical characterization for the $Ir_{40}Ni_{60}$/C alloy nanoparticles annealed at 400°C is discussed in the next section.

3.3.1 Electrochemical and XRD characterization of $Ir_{40}Ni_{60}$ alloy nanoparticles

Carbon supported $Ir_{40}Ni_{60}$ nanoparticles were synthesized using the same procedure as mentioned in chapter 2, section 2.1, except for the molecular ratio of salts were adjusted accordingly and the annealing temperature was maintained at 400°C to avoid particle size broadening. Figure 3.23(b) shows the XRD patterns for carbon supported $Ir_{40}Ni_{60}$ annealed at 400°C and IrNi nanoparticles annealed at 600°C with Cu Kα radiation in H_2 atmosphere for 2hrs. The pattern shows a formation of a solid solution with a particle size of 3nm.

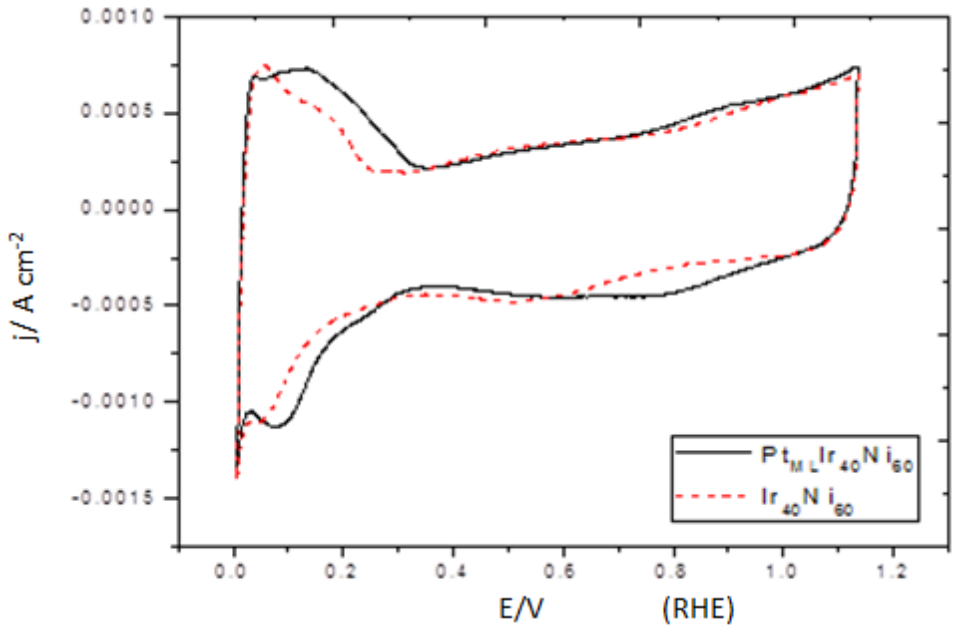

Figure3.25. Cyclic voltammetry curves for carbon supported $Ir_{40}Ni_{60}$ (red dash line) and for a Pt monolayer on a $Ir_{40}Ni_{60}$ surface (black solid line); sweep rate 20mV/s.

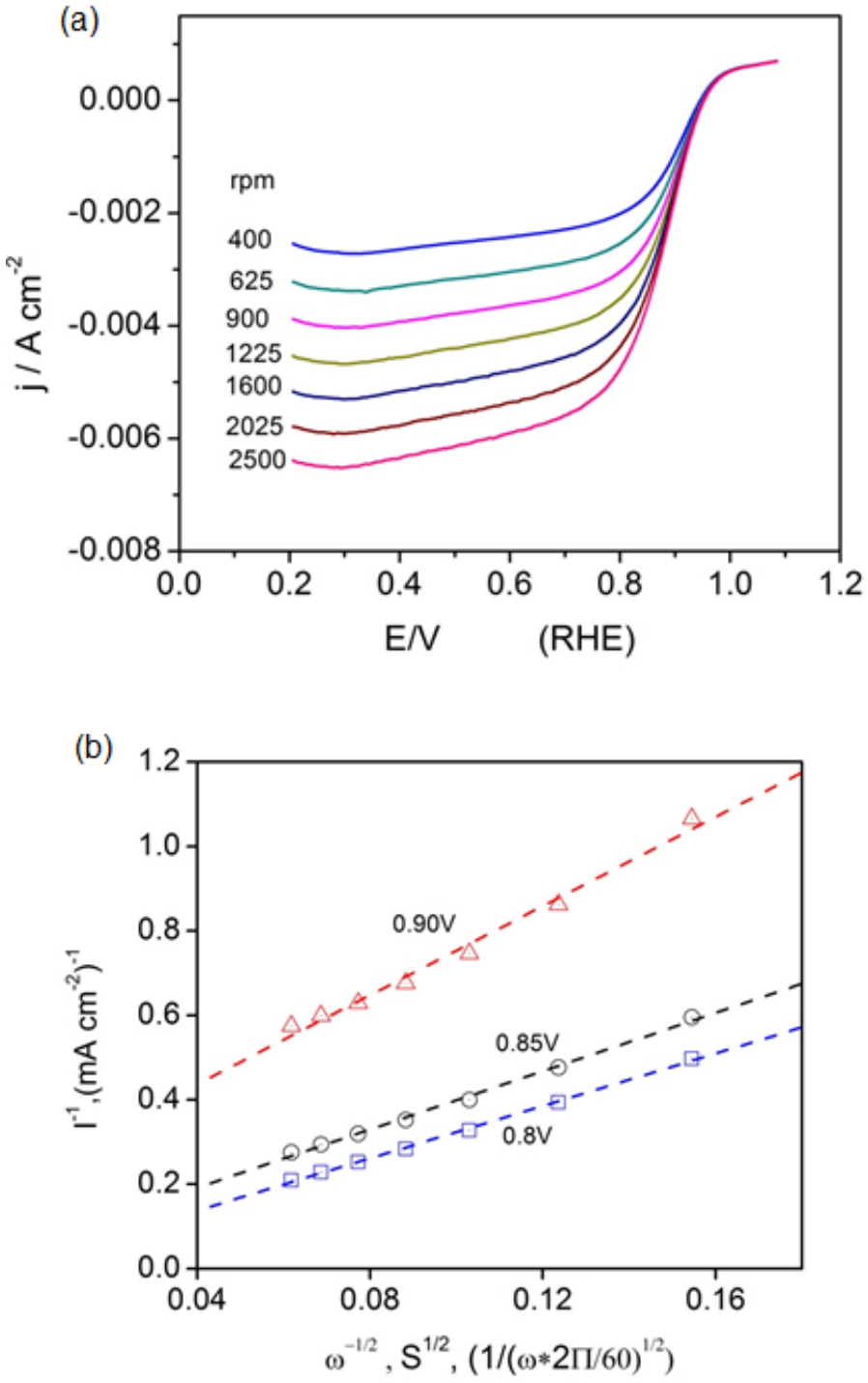

Figure3.26. (a) Polarization curves for the ORR on $Pt_{ML}Ir_{40}Ni_{60}$/C nanoparticles electrocatalysts at various rpm in oxygen-saturated 0.1 M $HClO_4$ and (b) Levich-Koutecky plots at various potentials

Cyclic voltammetry curves for carbon supported $Ir_{40}Ni_{60}$ and for a Pt monolayer deposited using Cu upd on an $Ir_{40}Ni_{60}$ surface is shown in figure 3.25. The voltammetry curves revealed no anodic currents that can be ascribed to the oxidation/dissolution of Ni, demonstrating that the Ni cores may have been covered by the noble metal shell and thus inaccessible to the electrolyte solution. The amount of Pt on the electrode was 6.17μg cm^{-2} calculated using the upd charge. Fig. 3.26 shows rotating disk electrode (RDE) measurements of the ORR on the Pt_{ML} $Ir_{40}Ni_{60}$/C electrocatalyst, made by RDE synthesis method, in a 0.1M $HClO_4$ solution purged by O_2 at different rotation speeds (400–2500 rpm) and scanned at a rate of 10mV/sec. The activity of the electrocatalyst is less compared to IrNi core-shell nanoparticles, as indicated by their half wave potentials (870mV Vs 890mV at a rotation rate of 1600rpm). Koutecky-Levich plot (Figure 3.26 (b)) was used to calculate the Pt mass activity of the Pt_{ML} $Ir_{40}Ni_{60}$/C electrocatalyst, which was 0.55 A/mg_{Pt} at 0.9 V/RHE, approximately 2.5 times less than Pt_{ML} IrNi electrocatalyst.

3.3.2 Summary and Discussion

Composition of metal and annealing temperature play an important role in the formation of IrNi solid solution. Carbon supported $Ir_{40}Ni_{60}$ nanoparticles when annealed at 600°C show larger particle size and much lower ORR activity. The same samples when annealed at 400°C show smaller particle size, but the ORR activity does not increase much due to poor Ir segregation to the surface. So formation of Ir rich shell is the key to better activity for ORR, reducing the amount of Ir in the alloy would jeopardize its segregation to the surface. Since the activity of Pt_{ML} $Ir_{40}Ni_{60}$/C electrocatalyst annealed at 400°C and 600°C is not comparably to Pt_{ML} IrNi electrocatalyst, further investigation into reducing the amount of precious metal remains

doubtful. Moreover further reducing the Ir content will result in Ni particles on the surface. Since Cu upd occurs neither on Ni nor on Ni rich surface, it is difficult to deposit a monolayer of Pt using the upd method.

3.4 Scale-up Synthesis of Pt Monolayer on IrNi Core-Shell Nanoparticles

The ideal model for the deposition of Pt monolayer on IrNi core shell nanoparticles is shown in Figure 3.27. Though the RDE synthesizing technique yields a higher ORR activity, large scale production of the catalyst is a requirement to make it feasible for practical fuel cell use. A method involving galvanic displacement of an upd Cu layer is environmentally friendly and economical because the Cu solution can be easily recycled and organic surfactant is not used. [135, 153-154] The synthesized catalysts are free of any surface contamination, which is highly favored for fuel cell applications. More importantly, the Pt shell thickness can be controlled through stepwise deposition, which is critical in engineering core-shell nanoparticles with high catalytic activity and cost efficiency.

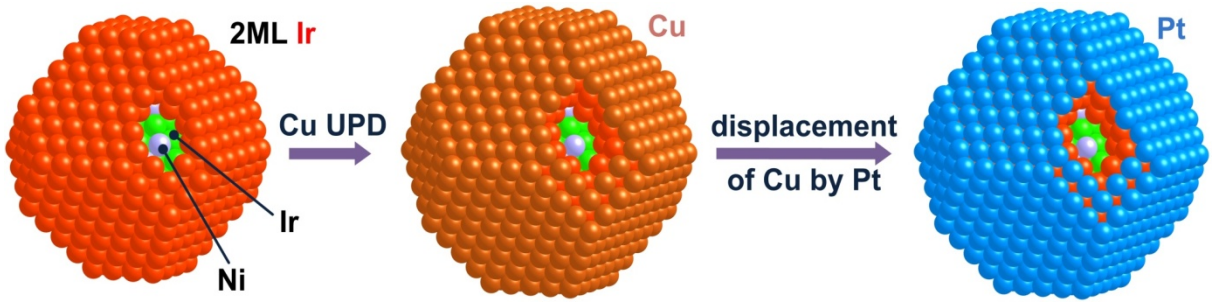

Figure3.27. Schematic of the Pt monolayer deposition on IrNi core using Cu upd method

3.4.1 XAS study on Pt_{ML} IrNi/C nanoparticles

In situ XANES of Pt L3, Ir L3 and Ni K edges were measured from the nanoparticles in 1 M $HClO_4$ at 0.41, 0.71, 0.91 and 1.11V. As shown in Figure 3.28(c) Ni in the nanoparticles is considered to be metallic and alloying with Ir has changed the electronic states of Ni atoms. Also the *in situ* XANES of Ir L3 edge (Figure 3.28(b)) from the nanoparticles does not show any shift in the Edge energy at various potentials indicating that the Ir atoms in the IrNi core material retain the same metallic form and that no appreciable amount of oxygenate species adsorb on the Ir sites in the potential range of 0.41-1.11 V. On the other hand the XANES spectra for Pt_{ML}IrNi/C at Pt L3 edge (Figure 3.28(a)) indicate a very small potential dependence. This effect is more evident in the relative change of the x-ray absorption peak intensity of the Pt L3 edge spectra for Pt_{ML}IrNi/C and Pt/C as a function of potential (Figure 3.28(d)). The increase in the intensity of the absorption edge peak for the Pt_{ML}IrNi/C electrocatalyst commences at considerably higher potentials than does that for the Pt/C catalyst. The Pt skin surface on the IrNi substrate is able to alleviate the OH inhibition on the catalyst surface and thus enhance the ORR activity. The difference in absorption properties between IrNi/C supported Pt monolayer and pure Pt is due to modification of the electronic properties of the surface atoms by the underlying metal via geometric strain and ligand interactions. [155-156]

(a)

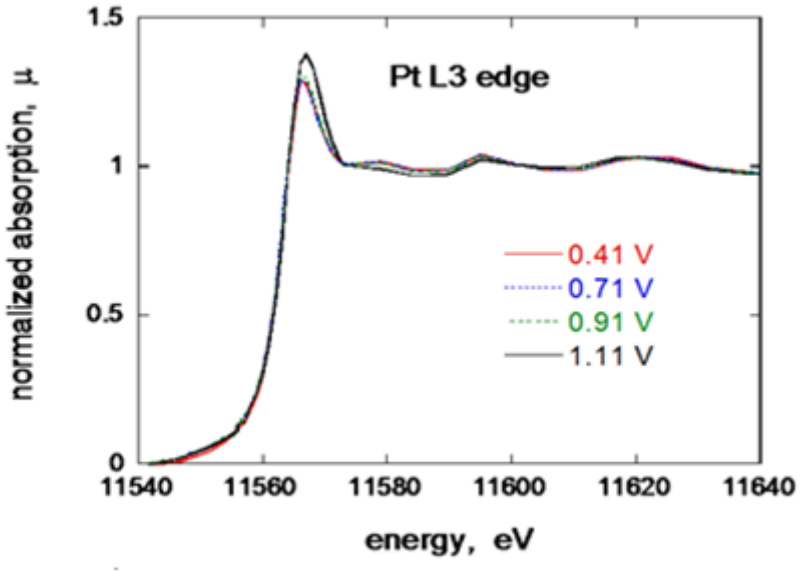
Pt L3 edge
normalized absorption, μ
energy, eV
0.41 V
0.71 V
0.91 V
1.11 V
1.5
1
0.5
0
11540
11560
11580
11600
11620
11640

(b)

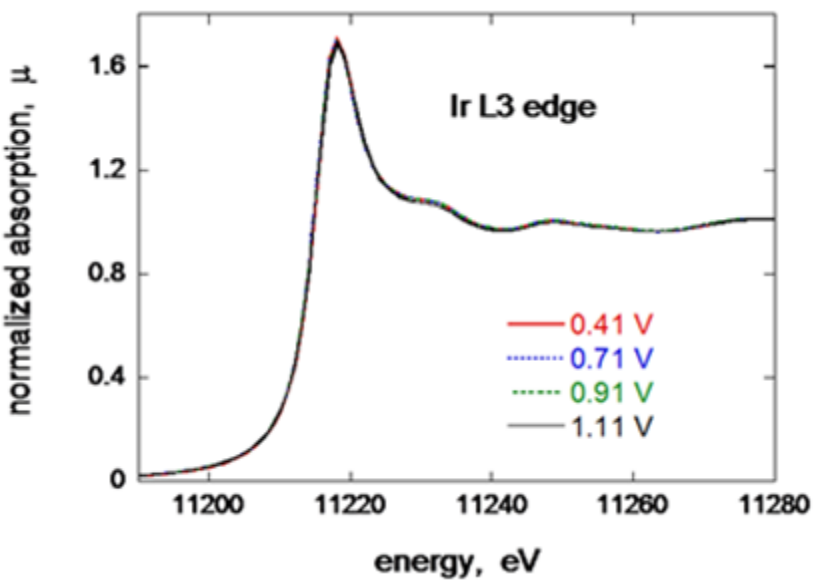
Ir L3 edge
normalized absorption, μ
energy, eV
0.41 V
0.71 V
0.91 V
1.11 V
1.6
1.2
0.8
0.4
0
11200
11220
11240
11260
11280

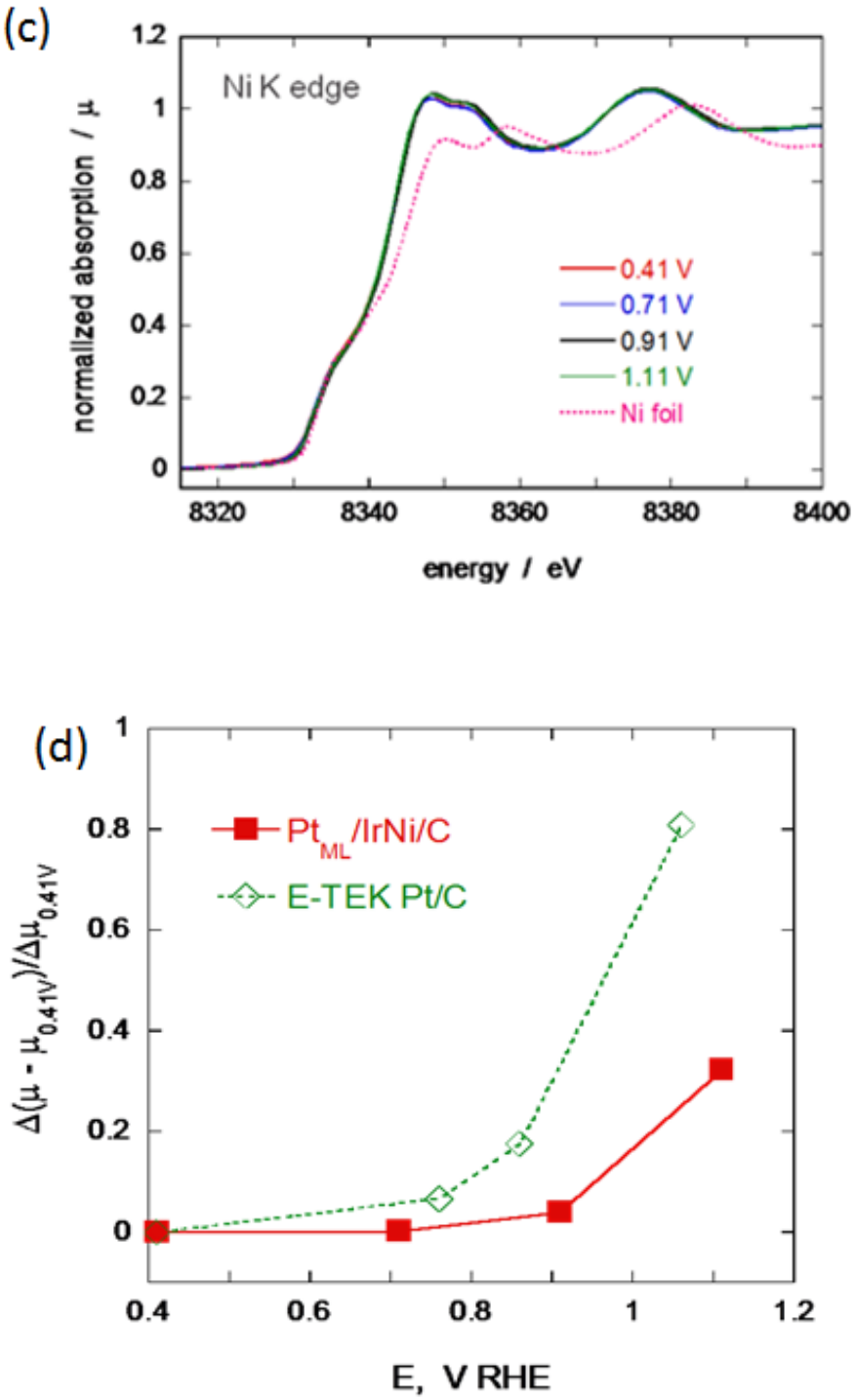

Figure3.28. In situ XANES for Pt monolayer IrNi electrocatalyst at various potentials, (a) Pt L3 edge, (b) Ir L3 edge (c) Ni K edge and (d) comparison on the change of the adsorption peak as a function of potential for Pt_{ML} IrNi/C and Pt/C

The significant delay in PtOH formation of the $Pt_{ML}IrNi/C$ electrocatalyst clearly indicates the better stability for the electrocatalyst which is also discussed further. The Pt and Ir mole ratio was 3:7 which was determined by the *ex situ* XAS analysis (figure 3.29). So, from combined XAS and EDX/TEM elemental analysis we get the final product molar ratio as $Pt\ Ir_{2.29}\ Ni_{1.29}$.

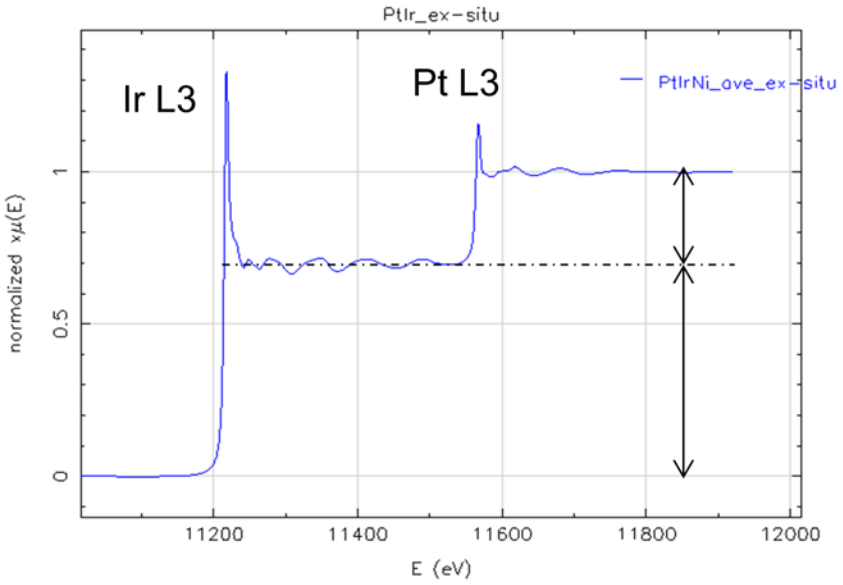

Figure3.29. *Ex situ* XAS analysis for Pt and Ir L3 edge

3.4.2 Structural Characterization of $Pt_{ML}IrNi/C$ nanoparticles

From the scaled-up synthesized sample, numerous individual particles of different sizes were imaged, and their Pt shell thicknesses were analyzed simultaneously by element-sensitive EELS spectroscopy. All signals from the Pt M (2122 eV), Ir M (2040 eV) and Ni L (855 eV) edges were detected by EELS mapping. Fig. 3.30 illustrates the line profile analysis by STEM/EELS showing distribution of Pt and IrNi components in a single nanoparticle.

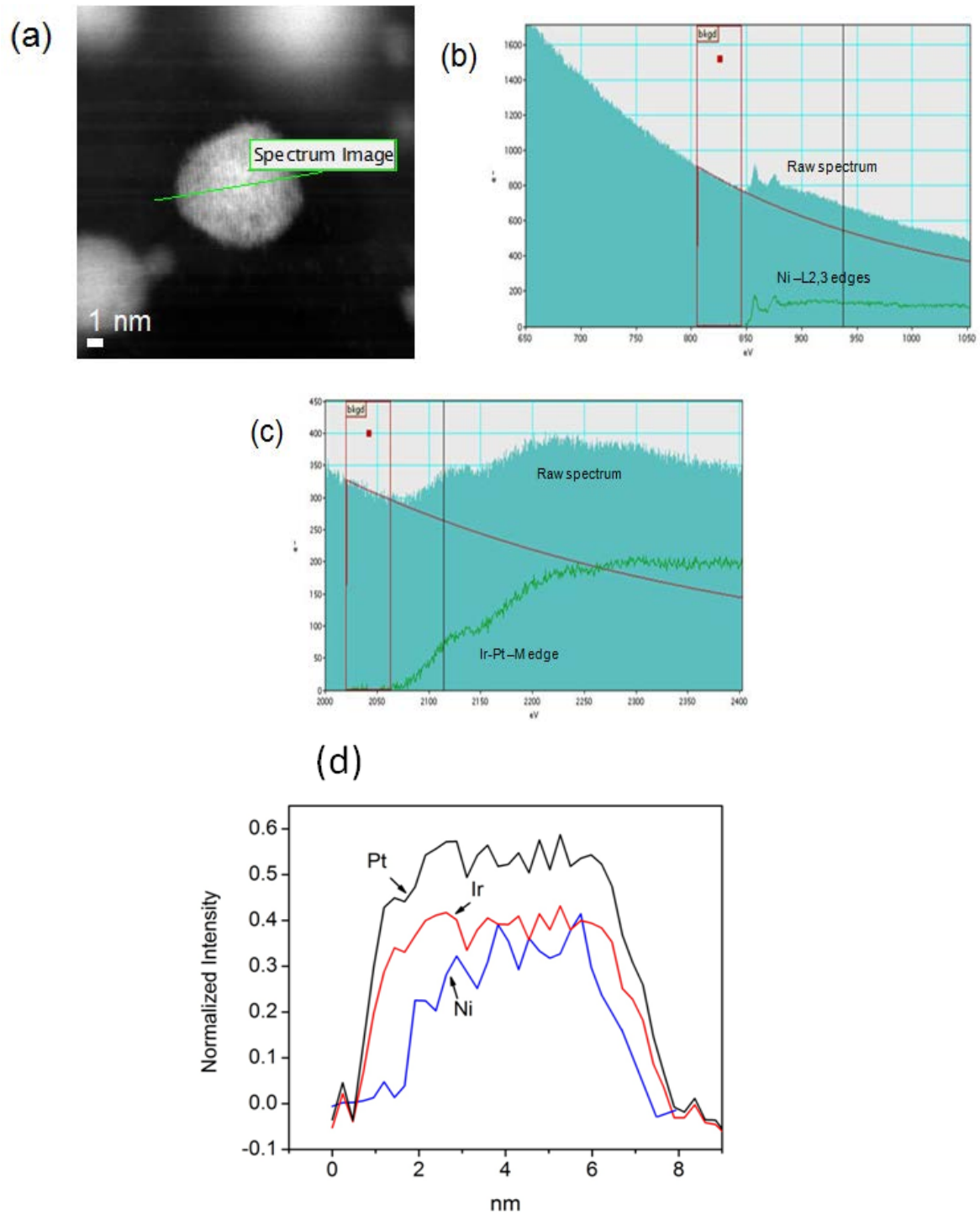

Figure3.30. (a) HAADF-STEM image of a PtIrNi nanoparticle, EELS spectra for (b) Ni L edge at the center of nanoparticle and (c) Ir and Pt M edge, and (d) comparison of the EELS intensities for the Pt and Ir M-edge and Ni L-edge along the scanned line (as indicated in Figure (a)).

Figure 3.30(a) shows a high angle annular dark field (HAADF) image of a representative single nanoparticle. The EELS spectra for Ni L-edge, Pt M-edge and Ir M-edge taken at the center of the nanoparticle are shown in Figures 3.30(b) and (c), respectively. In the figures, raw and background-subtracted spectra are illustrated. A STEM-EELS line scan of Pt, Ir M-edge and Ni L-edge scan can be done by moving the electron probe along the line indicated in figure 3.30(a) and their intensities are as shown in shown in figure 3.30(d). It is clearly observed that both the intensities of Ir and Ni are approximately constant around the center of nanoparticle and Ni is depleted at the both edges of nanoparticles. The differences in the Pt and the Ir profile, measured at the half value of the intensities are from 0.27 to 0.33nm, corresponding to approximately one monolayer Pt shell on IrNi alloy core. Thus, the formation of one monolayer of Pt shell over IrNi solid solution core is confirmed by EELS.

3.4.3 ORR measurements on scaled-up Pt_{ML} IrNi/C nanoparticles

Using the polarization curves of the Pt_{ML}/IrNi/C electrocatalyst in 0.1M $HClO_4$ solution purged by O_2 at different rotation speeds at a scan rate of 10mV/s, the inverse current density ($1/j$) was plotted as a function of the inverse of the square root of the rotation rate ($\omega^{1/2}$), also known as Koutecky–Levich plot (Figures 3.31 and 3.32(a) respectively). The linearity and parallelism of the Koutecky-Levich plots suggest first-order kinetics with respect to molecular oxygen. [50] Figure 3.32(b) compares the Pt mass activities at 0.9V for Pt/C (20%E-tek), Pt_{ML}/Ir/C and Pt_{ML}/IrNi/C nanoparticles. The Pt mass activity for our scaled-up Pt_{ML}/IrNi/C electrocatalyst and RDE synthesized Pt_{ML}/IrNi/C electrocatalyst are, respectively three to six times that of Pt/C electrocatalyst.

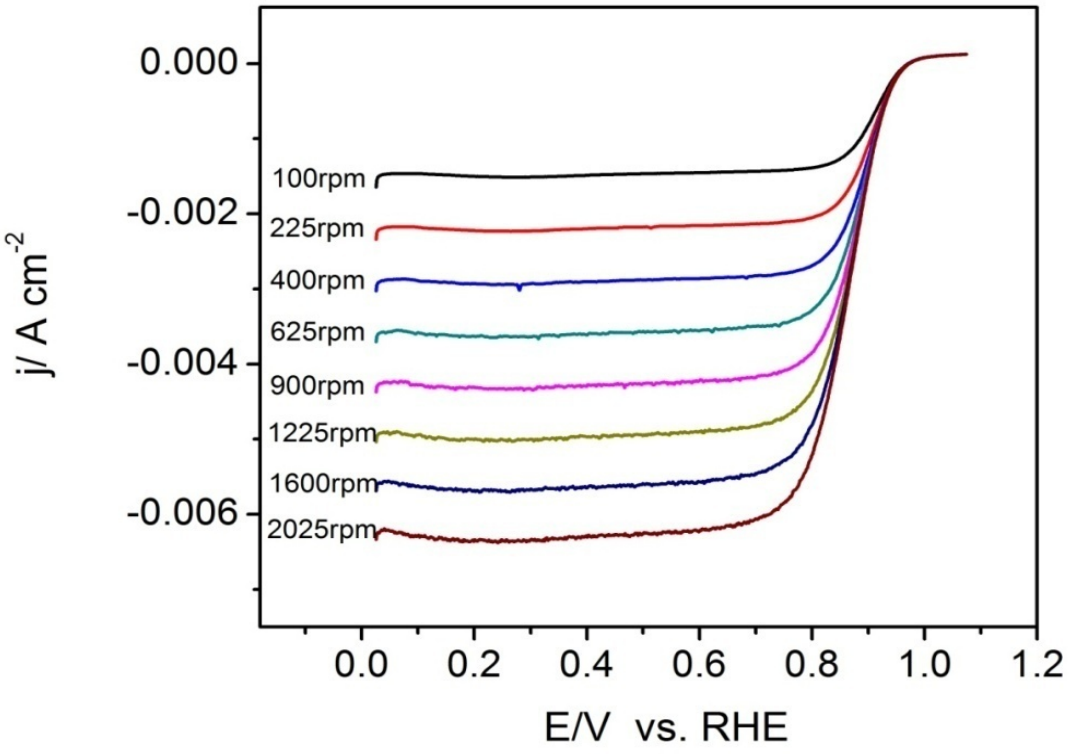

Figure3.31. Polarization curves for the ORR on the scaled-up Pt monolayer IrNi core electrocatalysts at various rpm in oxygen-saturated 0.1 M $HClO_4$.

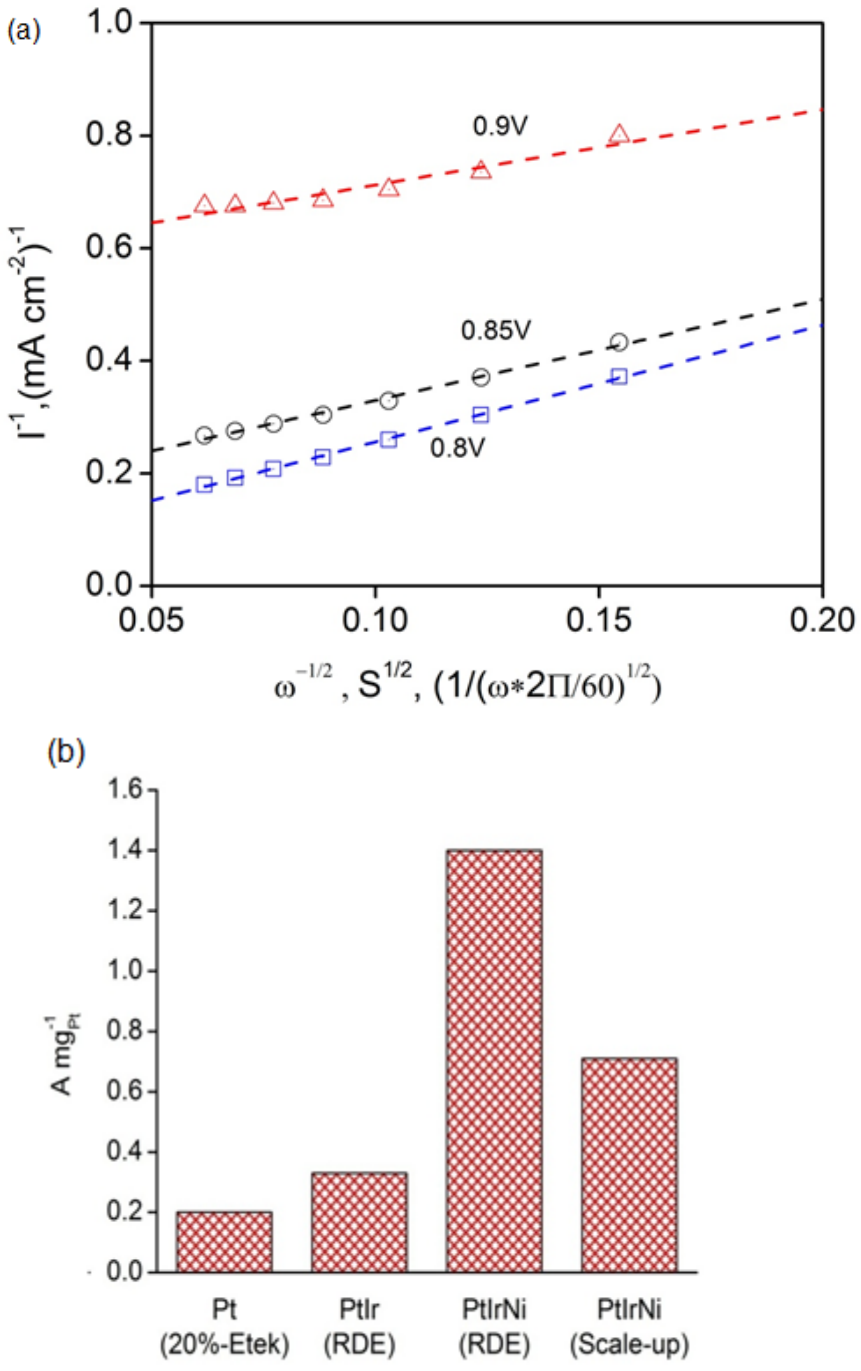

Figure3.32. (a) Levich-Koutecky plot for scaled-up Pt monolayer IrNi core electrocatalyst at various potentials. (b) Comparison of Pt mass activities for Pt/C (E-tek 20%), Pt_{ML}/Ir/C and Pt_{ML}/IrNi/C synthesized using RDE and scale-up synthesis method.

3.4.4 DFT calculations

DFT calculations were done to elucidate the observed enhancement of the Pt specific activity of $Pt_{ML}IrNi/C$ compared to that of the Pt/C and $Pt_{ML}Ir/C$ electrocatalysts. To simulate the nanoparticles properly, and to save computational time, sphere-like nanoparticle models of ~1.7 nm based on a truncated octahedron were constructed (Figure 3.33(a)). Since the model nanoparticle is smaller than the average size of the experimental ones (~5.0 nm), the experimental mole ratio of Ni/Ir = 0.56 with the two Ir monolayers for the $Pt_{ML}IrNi$ model couldn't be used. Thus, the mole ratio of the IrNi subcore (Ni/Ir = 0.37) was used. As Figure 3.33(d) shows, while the IrNi core has one Ir submonolayer (60 Ir atoms), it retains the Ir/Ni ratio of ~0.36 by replacing 14 of the 33 Ir atoms in the subcore with Ni atoms.

As Figure 3.33 illustrates, the BE-O was calculated that serves as a descriptor for scaling the ORR activity. [135] Figure 3.33(e) shows that partially replacing Ni in the core weakens the BE-O, and introduces more contraction therein (–3.45 eV and –4.12 %, respectively) compared to that of $Pt_{ML}Ir$ (–3.52 eV and –3.81 %, correspondingly). Figure 3.33(f) plots the BE-O variations against the d-band center, in which the trend from Pt to $Pt_{ML}Ir$ nanoparticles agrees with that reported for the extended surfaces (Pt(111) and $Pt_{ML}Ir(111)$). [37] In addition, this figure also shows that using Ir or IrNi as a core shifts the d-band center of Pt in the shell away from the Fermi level, thereby lowering the BE-O. [86] Interestingly, the partial replacement of Ir with Ni entails a slightly weaker BE-O than that of $Pt_{ML}Ir$ (~0.1 eV) (Figure 3.33(f)). Therefore, it is likely that extending the partial replacement of Ir by Ni in $Pt_{ML}IrNi$ should augment surface strain, and accordingly, lower the BE-O; expectedly, there should be a maximum for this due to the low stability of the Ni core under the ORR conditions. [157-158] To verify the trend of weakening of the BE-O upon mixing Ni with Ir, the extreme case with a pure Ni core ($Pt_{ML}Ni$)

was calculated; this led to the most strained surface and the weakest BE-O (–5.60 % and –3.12 eV, respectively).

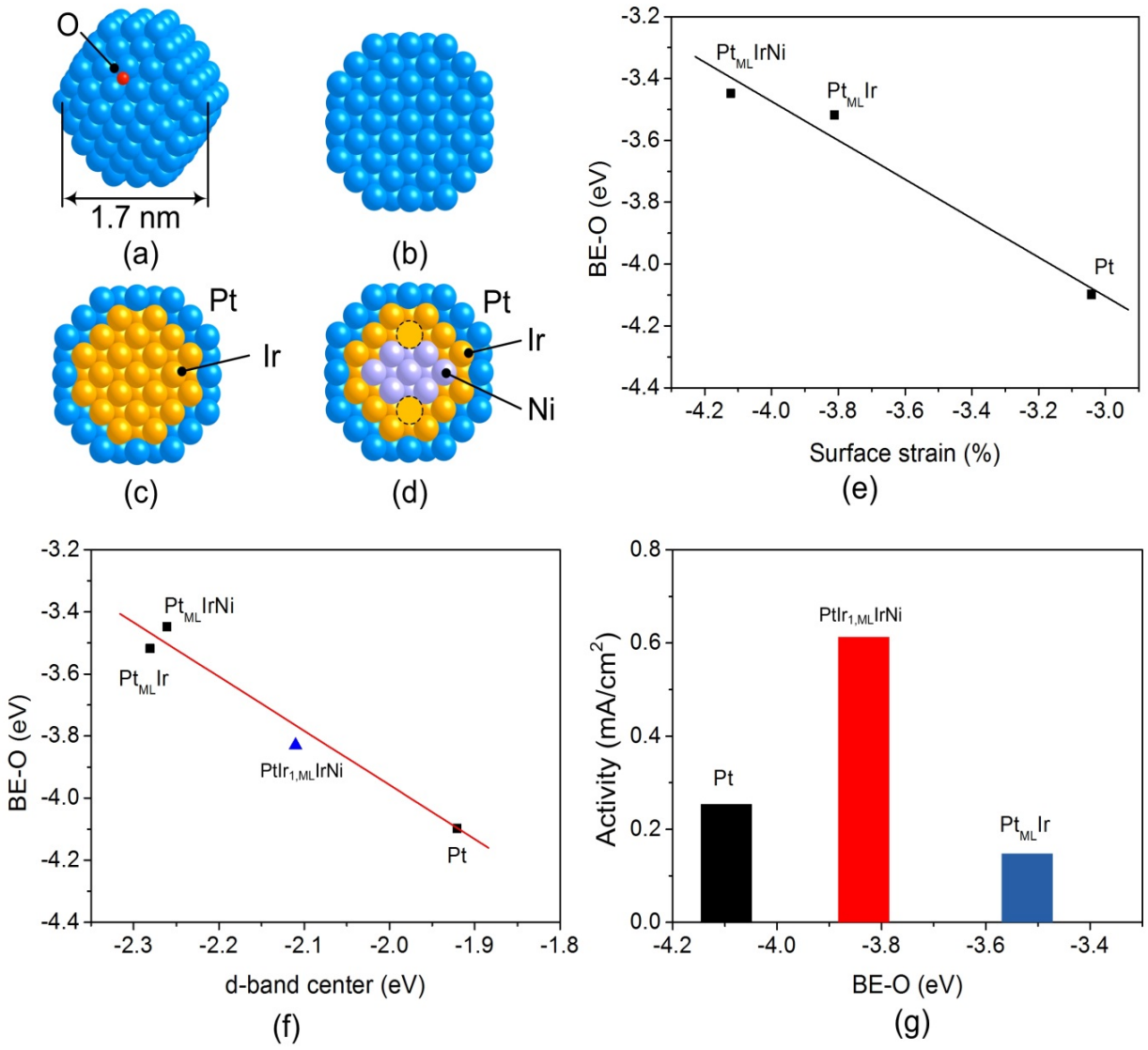

Figure3.33. (a) Schematic of a sphere-like nanoparticle representing adsorption of atomic oxygen at the fcc site. Cross sectional view of nanoparticle models of (b) Pt, (c) $Pt_{ML}Ir$, and (d) $Pt_{ML}IrNi$ with 1.7 nm. (e) Predicted binding energy of oxygen (BE-O) as a function of strain on $Pt_{ML}IrNi$, $Pt_{ML}Ir$ and Pt using the nanoparticle models. (f) Predicted binding energy of oxygen (BE-O) as a function of average d-band center of metals interacting with O on $PtIr_{1,ML}IrNi$, $Pt_{ML}IrNi$, $Pt_{ML}Ir$, and Pt. (g) Pt specific activity against BE-O on $PtIr_{1,ML}IrNi$, $Pt_{ML}Ir$ and Pt. "ML" is the monolayer.

Careful structural examination showed that $Pt_{ML}Ni$ is slightly collapsed inwardly, causing more surface contraction than do the other nanoparticles. Table 3.4 shows the predicted surface stains and binding energies of atomic oxygen of various nanoparticles. Based on the calculated strain, d-band center, and BE-O, a descriptor for the ORR activity, [135] it is anticipated that $Pt_{ML}Ir$ and $Pt_{ML}IrNi$ may have similar ORR activities, which cannot fully support experimental findings. Thus to gain a better understanding of the experimentally measured ORR activity, the possibility of anti-segregation under the ORR condition was also considered. Possibly, the Ir in the core might be exchanged with the Pt in the shell, driven by a stronger Ir-O interaction than that of Pt-O. To examine anti-segregational effects, one Ir atom was interchanged in the core with its interconnected Pt atom in the shell (in notation, $PtIr_{1,ML}IrNi$ for $Pt_{ML}IrNi$, and $PtIr_{1,ML}Ir$ for $Pt_{ML}Ir$. In agreement with a previous study by others on extended surfaces, [86] the calculations clearly show that for bare clusters, Ir preferentially remains in the core due to the energy cost of such transitions, i.e., 0.64 eV for $Pt_{ML}Ir \rightarrow PtIr_{1,ML}Ir$, and 0.53 eV for $Pt_{ML}IrNi \rightarrow PtIr_{1,ML}IrNi$. In addition, it is to be noted that it is energetically more costly to pull out Ir from the $Pt_{ML}Ir$ core and move it to the shell than it is when Ir is in a $Pt_{ML}IrNi$ core. Therefore, it should be concluded that only the anti-segregation of Ir of that latter, rather than the former. On exposure to oxygen, as shown in Figure 3.33(f), O predominantly moves to the Pt-Pt-Ir hybrid hollow site, and the corresponding BE-O is negatively shifted, –3.83 eV. Consequently, the cost of pulling one Ir atom out to the shell declines from 0.53 eV to 0.14 eV. That is, on interacting with oxygen, the anti-segregation of Ir energetically is more likely than that on the bare cluster, so strengthening the O-$Pt_{ML}IrNi$ interaction. Figure 3.33(g) illustrates the calculated BE-Os versus the measured specific activities for Pt/C, $Pt_{ML}Ir/C$, and $Pt_{ML}IrNi/C$. It should be noted that the BE-O for $Pt_{ML}IrNi$ corresponds to the strength of O binding after the exchange of one Ir atom in the core

with one Pt atom in the shell ($PtIr_{1,ML}IrNi$). Pt nanoparticles bind O too strongly to be removed from the catalyst, while $Pt_{ML}Ir$ does so too weakly to dissociate oxygen; hence, it lowers the ORR activity more than does Pt. In contrast, the partial replacement of Ir in the core with Ni favors the anti-segregation of Ir to the shell, and $Pt_{ML}IrNi$ supports a moderate binding of oxygen between Pt and $Pt_{ML}Ir$, so facilitating the efficient breakage of the O-O bond, and allowing the facile removal of O under fuel cell conditions. Accordingly, the highest ORR activity was measured. Overall, it is evident that the geometric, electronic, and segregation effects under fuel cell conditions are crucial in rationalizing the increase in the ORR activity of $Pt_{ML}IrNi/C$ compared to that of $Pt_{ML}Ir/C$ and Pt/C.

	Pt	$Pt_{ML}Ir$	$Pt_{ML}IrNi$	$PtIr_{1,ML}Ir$	$PtIr_{1,ML}IrNi$	$Pt_{ML}Ni$
Strain (%)	–3.04	–3.81	–4.12	–3.81	–4.12	–5.60
BE-O (eV)	–4.10	–3.52	–3.45	–3.93	–3.83	–3.12
d-band center (eV)	–1.92	–2.28	–2.26	–2.13	–2.11	–2.32

Table3.4. Predicted surface stains and binding energies of atomic oxygen of various nanoparticles

3.4.5 Stability of Scaled-up Pt_{ML} IrNi/C nanoparticles

The long-term stability of the ORR electrocatalysts is another critical requirement for applying them in fuel cells. The stability of the Pt monolayer electrocatalyst was evaluated by an accelerated test involving potential cycling between 0.6V and 1.0V/RHE at a scan rate of 50mV/sec in an air-saturated $HClO_4$ solution. Table 3.5 compares the loss in Pt and noble metal mass activity for the Pt_{ML}/IrNi/C electrocatalyst prepared on the glassy carbon electrode and in

the scale-up synthesis method. Voltammetry was used to determine the Pt surface area of the electrodes by measuring H adsorption before and after potential cycling. Integrating the charge between 0 and 0.33 V associated with H adsorption for Pt_{ML}/IrNi/C shows a small loss of Pt surface area (Figure 3.34). The table also shows the percentage loss in the initial surface area and the half wave potential after the accelerated cycling test. A decrease in H adsorption and desorption charges was observed after the potential cycling test compared with those before cycling. The catalyst made on glassy carbon electrode showed a 45% loss in the surface area and 18mV loss in half-wave potential after 30,000 cycles whereas the catalyst made by the scale-up synthesis method showed only a 23% loss in the Pt surface area and no loss in half-wave potential were observed even after 50,000 cycles.. The catalyst activity was much more stable for the sample obtained using the scale-up synthesis method. The Pt mass activity of the Pt_{ML}/IrNi/C electrocatalyst after 50,000 cycles is 0.57 A/mg_{Pt} at 0.9 V/RHE. The polarization curves at 1600 rpm on the Pt_{ML}/IrNi/C sample before and after 50000 potential cycles in 0.1 M $HClO_4$ show no change in activity as shown in Figure 3.35. This demonstrates the advantages of applying the galvanic displacement of a Cu upd layer to the large-scale synthesis of catalysts with well-defined core-shell structures.

	Synthesis on Glassy Carbon electrode					Scale-up synthesis Method				
	Mass Activity (j_k/ A mg^{-1})		Half-Wave Potential (mV)		% loss in surface area	Mass Activity (j_k/ A mg^{-1})		Half-Wave Potential (mV)		% loss in surface area
	Initial (0.9V)	After 30000 cycles (0.9V)	Initial	After 30000 cycles	After 30000 cycles	Initial (0.9V)	After 50000 cycles (0.9V)	Initial	After 50000 cycles	After 50000 cycles
Pt	1.4	0.48	890	872	45	0.71	0.57	851	851	23
PGM	0.78	0.27				0.22	0.17			

Table3.5. Mass activity, half-wave potentials and % loss in Pt surface area for the Pt_{ML}/IrNi/C catalyst before and after potential cycling

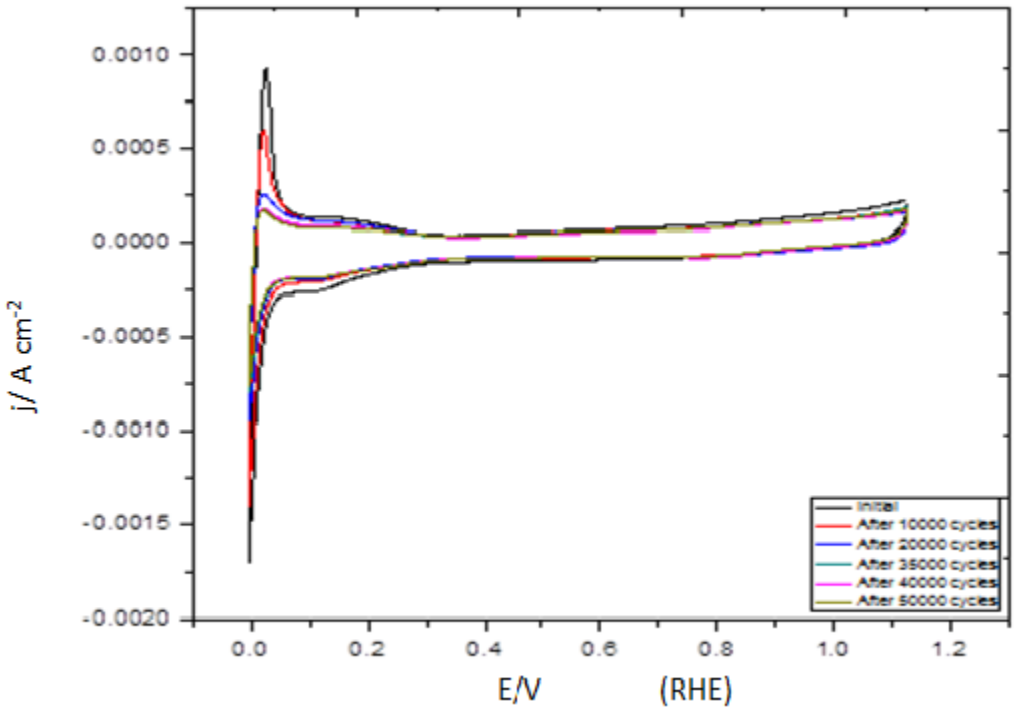

Figure3.34. Cyclic voltammetry in argon-saturated 0.1 M $HClO_4$ after various potential cycles; the scan rate was 20mVs^{-1}.

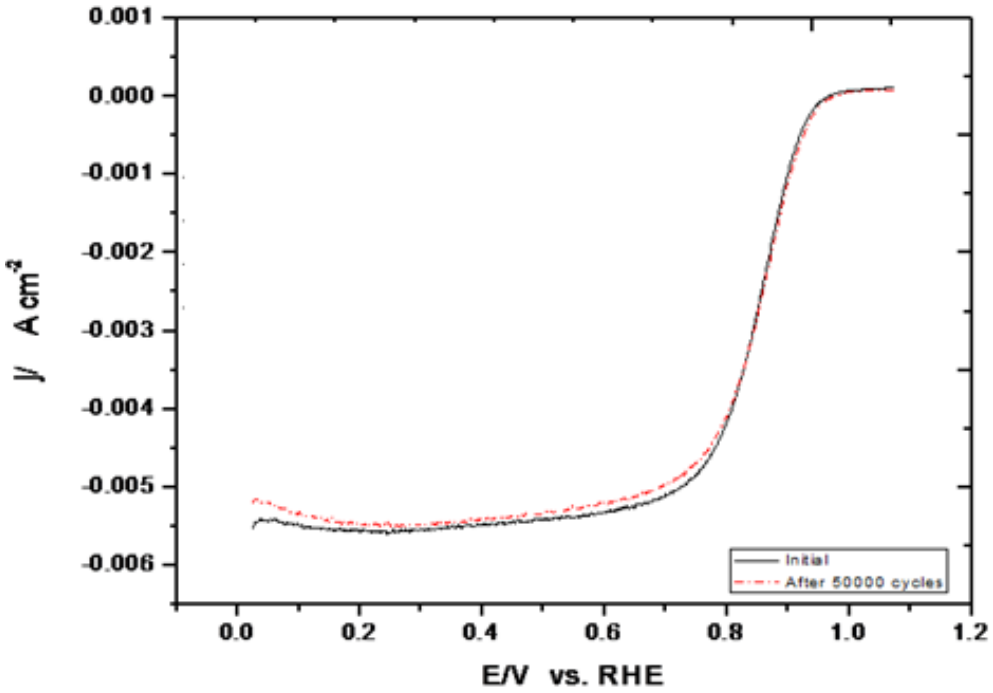

Figure3.35. Polarization curves for the ORR for scaled-up Pt_{ML}/IrNi/C electrocatalysts at 1600 rpm in oxygen-saturated 0.1 M $HClO_4$ at room temperature before and after 50000 cycles; the scan rate was $10mVs^{-1}$.

There have always been questions about Ni leaching out after potential cycling in acidic environment , so to check the hypothesis STEM/EELS analysis on numerous individual particles obtained after potential cycling was carried out. Figure 3.36(b) shows the distribution of Pt and IrNi components in a single representative nanoparticle after 50,000 cycles accelerated potential cycling. Figure 3.36(a) shows a HAADF image of a single nanoparticle after 50,000 potential cycles. The intensity of the spectra for the Pt M-edge, Ir M-edge and Ni L-edge are integrated along the line for a given energy region and the integrated values along the scanned line (as indicated in Figure 3.36a are shown in Figure 3.36b). It is clearly shown that the core-shell structure of IrNi nanoparticle is maintained even after 50,000 cycles of potential cycling. The Pt

and Ir shell protects Ni from leaching out. The Pt shell on IrNi nanoparticles is also intact which clearly justifies that IrNi core is very stable substrate for Pt monolayer.

The table 3.6 summarizes Electrochemical Surface Area (ECSA) and Pt mass and specific activities of various Pt/C catalysts with Pt monolayer catalyst system studied in this literature. Pt monolayer on IrNi substrate shows the highest activity and meets the Department of Energy (DOE) 2015 targets for Pt mass activity.

	Pt/C 8 nm	Pt/C 4nm	Pt/C 2.5nm	Pt/C 2nm	**Pt_{ML}/Ir RDE synthesis**	**Pt_{ML}/IrNi RDE synthesis**	**Pt_{ML}/IrNi Scale-up synthesis**	DOE Target (2015)
ECSA m^2/g Pt	35	75	96	115	253	103	167	
Pt specific activity j_k $mAcm^{-2}$	0.27	0.24	0.12	0.10	0.13	0.60	0.56	0.72
Pt mass activity j_k Amg^{-1}	0.10	0.20	0.12	0.12	0.33	1.4	0.71	0.44

Table3.6. ECSA, Pt specific and mass activity for various Pt/C catalysts and Pt monolayer catalyst

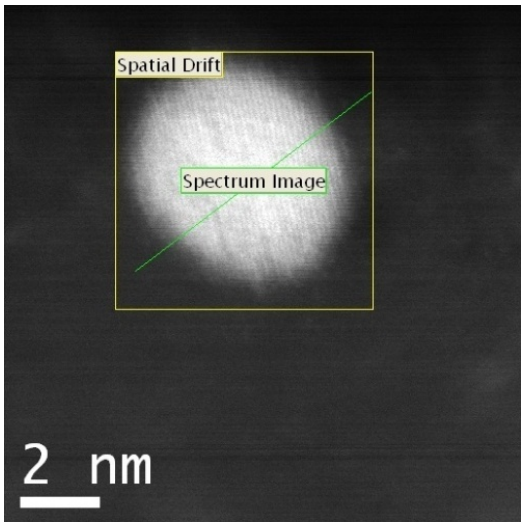

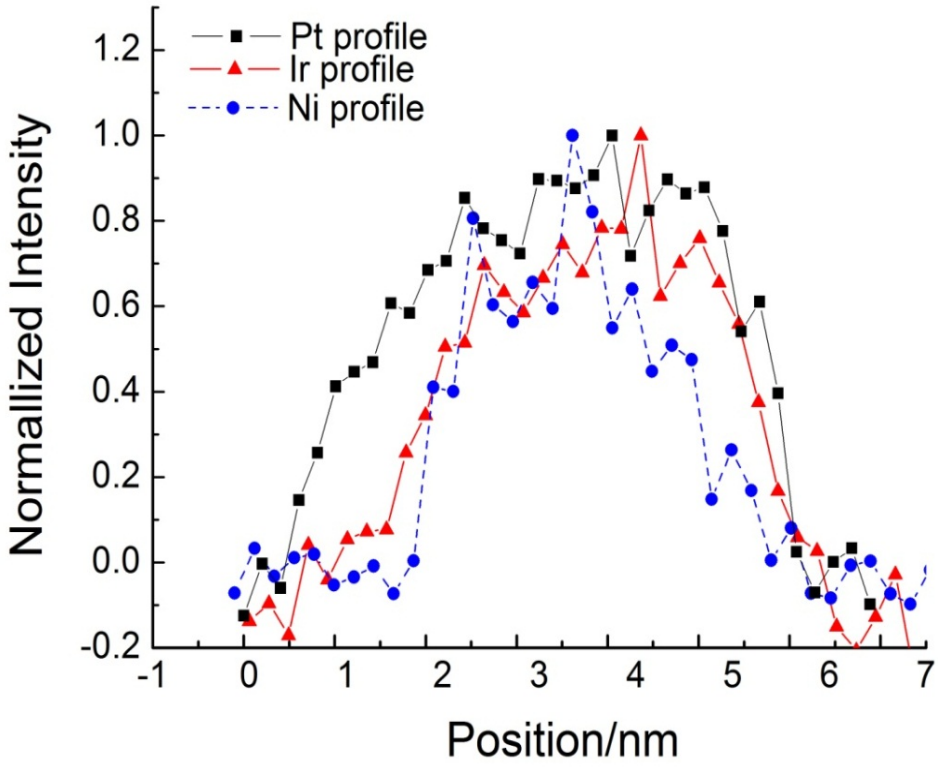

Figure3.36. (a) Representative HAADF-STEM image of a Pt_{ML}/IrNi/C nanoparticle after potential cycling test. (b) Comparison of the corresponding HAADF Pt (black), Ir (red) and Ni (blue) EELS intensity profiles in a line scan indicated.

3.4.6 Summary and Discussions

We demonstrated the formation of a new class of core-shell electrocatalysts for the ORR, consisting of a Pt monolayer shell and bimetallic IrNi core. Thus, we coupled highly stable, inexpensive core-shell nanoparticles with a Pt monolayer to produce electrocatalysts with high activity and very high stability. The results show that the activity of Pt monolayer electrocatalysts for the ORR is strongly substrate metal-dependent and our IrNi core-shell structured substrate is a new attractive core for Pt monolayer electrocatalysts. The electronic structure of substrates is an important factor because it can alter the catalytic activity of deposited Pt. Our DFT calculations using a sphere-like model clearly demonstrate that mixing Ni with Ir (Pt_{ML}/IrNi/C) induces geometric, electronic, and segregation effects and thus weakens the binding energy of oxygen, resulting in higher activity than in pure Pt/C and Pt_{ML}/Ir/C electrocatalysts. The galvanic displacement of a Cu upd layer demonstrated through gram-scale synthesis of Pt-shell on IrNi core catalysts seems very promising in scale-up synthesis of highly active, cost-effective nanoparticles with a core-shell structure suitable for specific catalytic reaction requirements. Thus the Pt monolayer approach holds excellent potential for creating efficient fuel cell electrocatalysts with cheaper price tags.

Chapter 4. Conclusion and Suggestions for Future Work

4.1 Conclusion

1) We showed a simple method of synthesizing carbon-supported IrNi core-shell structured nanoparticles by chemical reduction, followed by thermal annealing in H_2. We detailed the structure of the Ir shell on the IrNi alloy using XRD, STEM-EELS, and in situ XAS. The EXAFS analysis is consistent with the model wherein the IrNi nanoparticles are composed of two-layer Ir shells and IrNi alloy cores. In situ XAS showed that the Ir shells completely protect the Ni atoms comprising the cores from oxidation or dissolution in an acid solution under elevated potentials. Time-resolved synchrotron XRD measurements combined with Rietveld refinement analyses demonstrated the process of reaching a homogeneous mixture of Ir and Ni atoms during thermal annealing above 220°C, and the onset of Ir segregation on the IrNi core surfaces above 450°C. Iridium is known as one of the most stable elements against corrosion; thus, a shell comprising two Ir layers can protect non-noble metals such as Ni in cores, as this study clearly revealed. This new class of core-shell nanoparticles affords various possibilities for practical applications, such as electrocatalysts for fuel cells; one highly promising application is an anode electrocatalyst for hydrogen oxidation reaction. [159]

2) A new class of electrocatalysts consisting of a Pt monolayer deposited on carbon supported IrNi nanoparticles were synthesized and found to be very active electrocatalyst for the ORR in acid solutions. The modification of electronic and geometrical structures of Pt monolayer by the substrates results in a catalytic activity different from that of pure Pt. So it is possible to devise ORR electrocatalyst containing only a fractional amount of Pt and a very small amount of another noble metal whose activity can surpass that of the state-of-the-art carbon

supported Pt electrocatalyst. The intrinsic activity of Pt was found to be enhanced up to 3–fold by alloying Ir and Ni, forming bimetallic surfaces. This new approach represents a viable way to designing electrocatalyst with enhanced activity and with very low platinum loading. This new class of electrocatalyst also promises to alleviate some major problems of existing fuel cell technology by simultaneously decreasing the amount of precious materials and enhancing performance.

3) Composition of metal and annealing temperature play an important role in the formation of IrNi solid solution. Formation of Ir rich shell is the key to better activity for ORR, so reducing the amount of Ir in the alloy would jeopardize its segregation to the surface and thus its core-shell structure.

4) DFT calculations using a sphere-like model clearly demonstrate that mixing Ni with Ir (Pt_{ML}/IrNi/C) induces geometric, electronic, and segregation effects and thus weakens the binding energy of oxygen, resulting in higher activity than in pure Pt/C and Pt_{ML}/Ir/C electrocatalysts.

5) The galvanic displacement of a Cu upd layer demonstrated through gram-scale synthesis of Pt-shell on IrNi core catalysts seems very promising in scale-up synthesis of highly active, cost-effective nanoparticles with a core-shell structure suitable for specific catalytic reaction requirements. Thus the Pt monolayer approach holds excellent potential for creating efficient fuel cell electrocatalysts with cheaper price tags.

6) The results show that the activity of Pt monolayer electrocatalysts for the ORR is strongly substrate metal-dependent and our IrNi core-shell structured substrate is a new attractive core for Pt monolayer electrocatalysts. The structure of substrates is an important factor because it can alter the catalytic activity of deposited Pt.

7) Accelerated potential cycling test shows a negligible loss of activity for Pt_{ML}/IrNi/C catalyst thus demonstrating an effective way of using Pt that can resolve key ORR problems which include inadequate activity and durability while minimizing the Pt loading.

4.2 Suggestions for Future Work

1) Durability test under potential cycling

The long term durability of the Pt monolayer electrocatalysts under fuel cell operating conditions needs to be investigated and improved. Continuously cycling the catalysts in Fuel cell membrane electrode assemblies (MEAs) at elevated temperature under fuel cell operating conditions in wide potential range is a useful way to test the durability of the catalysts, because the cycling in MEAs leads to accelerated Pt dissolution rates compared to extended holds at constant potentials. [160-161]

2) Theoretical modeling

The likelihood of developing cathode catalysts with improved mass activity and durability would be largely increased if accompanied by strong fundamental molecular modeling approaches. These models should include electrochemical aspects by considering the factors of electrolyte solution and electrode potential.

3) Better understanding and designing of the core-shell structure substrate for Pt monolayer

Reducing the amount of noble metal in the substrate without affecting its activity would be a much better milestone and a step closer to make fuel cells practical. The preparation of catalyst support will be the key to achieve this goal. One of the most challenging areas in the preparation of core-shell nanoparticle is the control over size and composition in the nanometer range. New techniques to make cheaper core-shell structured substrate for Pt monolayer electrocatalyst must be further studied, thus paving way for commercialization of fuel cells.

References

[1] W. Grove, Phios. Mag., Ser. 3 **1839**, 14, 127.

[2] L. Carrette, K.A. Friedrich, U. Stimming, *Fuel Cells*, **2001**.

[3] M.R. Tarasevich, A. Sadkowski, E. Yeager, in *Comprehensive Treatise of Electrochemistry*, Vol. 7 (Eds.: B. E. Conway, J. O. Bockris, E. Yeager, S. U. M. Khan, R. E. White), Plenum Press, New York, **1983**, p. 301.

[4] R. R. Adzic, in *Electrocatalysis* (Eds.: J. Lipkowski, P. N. Ross), Wiley-VCH, Inc., **1998**, p. 197.

[5] P.W. Atkins, *Physical Chemistry*, 5th Ed; Oxford University Press: Oxford, 1994.

[6] *The Hydrogen Economy: Opportunities, Cost, barriers and R&D Needs*; National Research Council, Ed.; The National Academic Press: Washington, D.C., 2004.

[7] M.W. Breiter, Reaction Mechanism of the H_2 Oxidation/Evolution Reaction. In *Handbook of Fuel Cells- fundamentals, Technology and Applications*; Vielstich, W., Lamm, A., Gasteiger, H.A., Eds.; John Wiley & Sons: Chichester, 2003; Vol. 2: Electrocatalysis; pp 361.

[8] N.M. Markovic, The Hydrogen Electrode Reaction. In *Handbook of Fuel Cells-fundamentals, Technology and Applications*; Vielstich, W., Lamm, A., Gasteiger, H.A., Eds.; John Wiley & Sons: Chichester, 2003; Vol. 2: Electrocatalysis; pp 368.

[9] J. Heyrovsky, *Recl. Trav. Chim. Pays-Bas* **1927**, 46, 582.

[10] J.Z. Tafel, *Phys. Chem. Stoechiom. Verwandtschaftsl*. **1905**, 50, 641.

[11] T. Volmer, M.Z. Erdey-Gruz, *Phys. Chem. Abt. A* **1930**, 150, 203.

[12] J.X. Wang, T.E. Springer, R.R. Adzic, *J. Electrochem. Soc*. **2006**, 153, A1732.

[13] B. C. H. Steele, A. Heinzel, *Nature* **2001**, 44, 345.

[14] K. Wang, H. A. Gasteiger, N. M. Markovic, P. N. Ross, *Electrochim. Acta* **1996**, 41, 2587.

[15] J. Divisek, H. F. Oetjen, V. Peinecke, V. M. Schmidt, U. Stimming, *Electrochim. Acta* **1998**, 43, 3811.

[16] M. Gotz, H. Wendt., *Electrochim. Acta.* **1998**, 43, 3637.

[17] L. E. Ley, R. Liu, C. Pu, Q. Fan, N. Leyarovska, C. Segre, E. S. Smotkin, *J.Electrochem. Soc.* **1997**, 144, 1543.

[18] B. Gurau, R. Viswanathan, R. Liu, T. J. Lanfrez, K. Ley, E. S. Smotkin, E. Reddington, A. Sapienza, C. Chan, T. E. Mallouk, S. Sarangapani, *J. Phys. Chem.B* **1998**, 102, 9997.

[19] S. R. Brankovic, J. X. Wang, Y. Zhu, R. Sabatini, J. McBreen, R. R. Adzic, *Journal of Electroanalytical Chemistry* **2002**, 524–525, 231–241.

[20] K. Sasaki, Y. Mo, J. X. Wang, M. Balasubramanian, F. Uribe, J. McBreen, R. R. Adzic, *Electrochimica Acta* **2003**, 48, 3841.

[21] K. Sasaki, J. X. Wang, M. Balasubramanian, J. McBreen, F. Uribe, R. R. Adzic, *Electrochimica Acta* **2004**, 49, 3873–3877.

[22] T. Iwasita, *Electrochim. Acta* **2002**, 47, 3663.

[23] T. Iwasita, R. Dalbeck, E. Pastor, X. Xia, *J. Electroanal. Chem*. **1994**, 39, 1817.

[24] H.A. Gasteiger, S.S. Kocha, B. Sompalli, F.T. Wagner, *Appl. Catal. B* **2005**, 56, 9.

[25] D.A. Landsman, F.J. Luczak, catalyst studies and Coating Technologies. In *Handbook of Fuel Cells- fundamentals, Technology and Applications*; W. Vielstich, A. Lamm,

H.A. Gasteiger, Eds.; John Wiley & Sons: Chichester, 2003; Vol. 4: Fuel Cell Technology and Applications; pp 811.

[26] D. Thompsett, Pt alloys as Oxygen Reduction Catalyst. In *Handbook of Fuel Cells-fundamentals, Technology and Applications*; W. Vielstich, A. Lamm, H.A. Gasteiger, Eds.; John Wiley & Sons: Chichester, 2003; Vol. 3: Fuel Cell Technology and Applications; pp 467.

[27] K.J.J. Mayrhofer, B.B. Blizanac, M. Arenz, V.R. Stamenkovic, P.N. Ross, N.M. Markovic, *Journal of Physical Chemistry B* **2005**, 109, 14433.

[28] S. Mukerjee, S. Srinivasan, M.P. Soriaga, J. McBreen, *J.Electrochem. Soc.* **1995**, 142, 1409.

[29] M.H. Shao, K. Sasaki, R.R. Adzic, *J. Am. Chem. Soc*. **2006**, 128, 3526.

[30] M.H. Shao, T. Huang. P. Liu. J. Zhang. K. Sasaki, R.R. Adzic, *Langmuir*. **2006,** *22* (25), pp 10409–10415.

[31] J.L. Fernandez, V. Raghuveer, A. Manthiram, A.J. Bard, *J. Am. Chem. Soc*. **2005**, 127, 13100.

[32] J.L. Fernandez, D.A. Walsh, A.J. Bard, *J. Am. Chem. Soc*. **2005**, 127, 357.

[33] M. Bron, J. Radnik, M. Fieber-Erdmann, P. Bogdanoff, S. Fiechter, *J. Electroanal. Chem*. **2002**, 535, 113.

[34] G. Faubert, R. Cote, J.P. Dodelet, M. Lefevre, P. Bertrand, *Electrochim. Acta*. **1999**, 44, 2589.

[35] M. Lefevre, J.P. Dodelet, P. Bertrand, *J. Phys. Chem. B*. **2000**, 104, 11238.

[36] F. Jaouen, S. Marcotte, J.P. Dodelet, G. Lindbergh. *J. Phys. Chem. B*. **2003**, 107, 1376.

[37] J. L. Zhang, M.B. Vukmirovic, Y. Xu, M. Mavrikakis, R.R. Adzic, *Angew. Chem. Int. Ed*. **2005**, 44, 2132.

[38] A. C. Templeton, W. P. Wuelfing, R. W. Murray, *Acc. Chem. Res*. **2000**, 33, 27.

[39] F. Caruso, *Adv. Mater.* **2001**, 13, 11.

[40] W. Schärtl, *Adv. Mater*. **2000**, 12, 1899.

[41] P. Liu, J. K. Norskov, *Phys. Chem. Chem. Phys*. **2001**, 3, 3814.

[42] S. Gottesfeld, T.A. Zawodzinski, *In advances in Electrochemical Science and Engineering*; R.C. Alkire, D.M. Kolb, Eds.; Wiley: Weinheim, 1997, Vol.5.

[43] N.M. Markovic, T.J. Schmidt, V. Stamenkovic, P.N. Ross, *Fuel Cells* **2001**, 1, 105.

[44] L. Mueller, L. Nekrasov, *Electrochim. Acta*. **1964**, 9, 1015.

[45] A. Damjanovic, M. A. Genshaw, J. O. M. Bockris, *J. Phys. Chem*. **1966**, 45, 4057.

[46] A. Damjanovic, V. Brusic, *J. Electrochim. Acta* **1967**, 12, 615.

[47] H. S. Wroblowa, Y.-C. Pan, G. Razumney, *J. Electroanal. Chem*. **1976**, 69, 195.

[48] V. S. Bagotskii, M. R. Tarasevich, V. Y. Filinovskii, *Elektrokhimiya*. **1969**, 5, 1218.

[49] V. S. Bagotskii, M. R. Tarasevich, V. Y. Filinovskii, *Elektrokhimiya.* **1972**, 8, 84.

[50] N. A. Anastasijevic, V. B. Vesovic, R. R. Adzic, *J. Electroanal. Chem*. **1987**, 229, 305; 317.

[51] M. Gattrell, B. Macdougall, Reaction Mechanism of the Oxygen reduction/evolution reaction. In *Handbook of Fuel Cells- fundamentals, Technology and Applications*; W. Vielstich, A. Lamm, H.A. Gasteiger, Eds.; John Wiley & Sons: Chichester, 2003; Vol. 2: pp 443.

[52] A. Damjanovic, M. A. Genshaw, J. O. M. Bockris, *J. Electrochem. Soc*. **1967**, 114, 1107.

[53] J. C. Huang, R. K. Sen, Yeager, *J. Electrochem. Soc*. **1979**, 126, 736.

[54] V. J. Lukyanycheva, A. V. Yuzhenina, B. J. Lentsner, L. L. Knots, N. A Shumilova, V. S. Bagotskii, *Elektrokhimiya* **1971**, 7, 1287.

[55] L. I. Antropov, C. G. Vrzhosek, M. R. Tarasevich, M. A. Marinich, *Elektrokhimiya* **1972**, 8, 149.

[56] C. Puglia, A. Nilsson, B. Hernnais, O. Karis, P. Bennich, N. Martensson, *Surf. Sci*. **1995**, 342, 119.

[57] A. W. E. Chan, R. Hoffmann, W. Ho, *Langmuir* **1992**, 8, 1111.

[58] A. Damjanovic, M. A. Genshaw, J. O. M. Bockris, *J. Phys. Chem*. **1964**, 45, 4057.

[59] A. Damjanovic, V. Brusic, J. O. M. Bockris, *J. Phys. Chem*. **1967**, 71, 2471.

[60] D. B. Sepa, M. V. Vojnovic, A. Damjanovic, *Electrochim. Acta* **1981**, 26, 781.

[61] D. B. Sepa, M. V. Vojnovic, L. M. Vracar, A. Damjanovic, *Electrochim. Acta* **1987**, 32, 129.

[62] N. M. Markovic, P. N. Ross, *In Interfacial Electrochemistry* (Ed.: A. Wieckowski), Marcel Dekker, New York, 1999, p. 821.

[63] N. M. Markovic, T. J. Schmidt, V. Stamenkovic, P. N. Ross, *Fuel Cells* **2001**, 1, 105.

[64] J. X. Wang, N. M. Markovic, R. R. Adzic, *J. Phys. Chem. B* **2004**, 108, 4127.

[65] E. Yeager, M. Razaq, D. Gervasio, A.Razaq, D. Tryk, *In Structrual Effects in Electrocatalysis and Oxygen Electrochemistry*, Vol. 92-11 (Eds.: D. Scherson, D. Tryk, M. Daroux, X. Xing), The Electrochem. Soc. Inc, Pennington NJ, 1992, p. 440.

[66] E. Yeager, M. Razaq, D. Gervasio, A.Razaq, D. Tryk, *J. Serb. Chem. Soc*. **1992**, 57, 819.

[67] S. J. Clouser, J. C. Huang, E. Yeager, *J. Appl. Electrochem*. **1993**, 23, 597.

[68] N. Freyer, M. Kiskinova, G. Pirug, H. P. Bonzel, *Surf. Sci*. **1986**, 166, 206.

[69] J. Schidt, C. Stuhlmann, H. Ibach, *Surf. Sci*. **1993**, 284, 121.

[70] A. C. Luntz, J. Grimblot, D. E. Fowler, *Phys. Rev. B* **1989**, 39, 12903.

[71] B. N. Grgur, N. M. Markovic, P. N. Ross, Jr., *Langmuir* **1997**, 13, 6370.

[72] N. M. Markovic, H. A. Gasteiger, P. N. Ross, Jr., *J. Phys. Chem*. **1996**, 100, 6715.

[73] J. K. Nørskov, J. Rossmeisl, A. Logadottir, L. Lindqvist, J. R. Kitchin, T. Bligaard, H. Jonsson, *J. Phys. Chem. B* **2004**, 108, 17886.

[74] V. M. Jalan, E. J. Taylor, *J. Electrochem. Soc*. **1983**, 130, 2299.

[75] S. Mukerjee, *J. Appl. Electrochem*. **1990**, 20, 537.

[76] S. Mukerjee, S. Srinivasan, M. Soriaga, J. M. Breen, *J. Phys. Chem*. **1995**, 99, 4577.

[77] K. Kinoshita, *Electrochemical Oxygen Technology*, John Wiley & sons, Inc., Pennington, New Jersey.

[78] J.M. Yan, X.B. Zhang, T. Akita, M. Haruta and Q. Xu, *J. Am. Chem. Soc*., **2010**, 132, 5326-5327.

[79] S. Alayaglu, P. Zavalij, B. Eichhorn, Q. Wang, A.I. Frenkel and P. Chupas, *ACS Na*no, **2009**, 3, 3127-3137.

[80] Y.W. Lee, M. Kim, Z.H. Kim and S.W. Han, *J. Am. Chem. Soc*., **2009**, 131, 17036-1737.

[81] S. Alayaglu, A.U. Nilekar, M. Mavrikakis and B. Eichhorn, *Nature Mater*., **2008**, **7**, 333-338.

[82] Y. Cui, B. Ren, J.L. Yao, R.A. Gu, and Z.Q. Tian, *J. Phys. Chem. B,* **2006**, 110, 4002-4006.

[83] M.P. Mallin and C.J. Murphy, *Nano Lett.*, **2002**, 2, 1235-1237.

[84] A. V. Ruban, H. L. Skriver and J. K. Norskov, *Phys. Rev. B*, **1998**, 59, 15990-16000.

[85] E. Christoffersen, P. Liu, A. Ruban, H.L. Skriver and J.K. Noskov, *J. Catal*., **2001**, 199, 23-131.

[86] B. Hammer and J.K. Norskov, *Adv. Catal*., **2000**, 45, 71-129.

[87] M. Mavrikakis, B. Hammer and J. K. Nørskov, *Phys. Rev. Lett.* **1998**, 81, 2819-2822.

[88] A. Naitabdi, L.K. Ono, F. Behafarid and B. Roldan Cuenya, *J. Phys. Chem. C*, **2009**, 113, 1433-1446.

[89] P.S. Normile, J.A. De Toro, J.P. Andres, J.A. Gonzalez, T. Munoz, P. Muniz, A.J. Barbero and J.M. Riveiro, *J. Appl. Phys*., **2006**, 100, 064312-4.

[90] A. J. Appleby, *Journal of Power Source*, **1996**, 69, 153.

[91] S. R. Brankovic, J. X. Wang, R. R. Adzic, *J. Serb. Chem. Soc*. **2001**, 66, 887.

[92] J. X. Wang, S. R. Brankovic, R. R. Adzic, *Electrochem. Solid-state Lett*. **2001**, 4, A217.

[93] J. Zhang, Y. Mo, M. B. Vukmirovic, R. Klie, K. Sasaki, R. R. Adzic, *J. Phys.Chem. B* **2004**, 108, 10955.

[94] J. A. Rodriguez, *Surf. Sci. Rep*. **1996**, 24, 225.

[95] M. Baldauf, D. M. Kolb, *J. Phys. Chem*. **1996**, 100, 11375.

[96] H. Naohara, S.Ye, K. Uosaki, *Electrochim. Acta* **2000**, 45, 3305.

[97] T. J. Schmidt, V. Stamenkovic, M. Arenz, N. M. Markovic, P. N. Ross, *Electrochim. Acta* **2002**, 47, 3765.

[98] J. R. Kitchin, J. K. Nørskov, M. A. Barteau, J. G. Chen, *J. Chem. Phys*., Vol. 120, No. 21, **2004**, 120, 10240.

[99] Y. Xu, A. V. Ruban, M. Mavrikakis, *J. Am. Chem. Soc*. **2004**, 126, 4714.

[100] J. A. Rodriguez, D. W. Goodman, *Science* **1992**, 257, 897.

[101] F. B. de Mongeot, M. Scherer, B. Bleich, E. Kopatzki, R. J. Behm, *Surf. Sci.* **1998**, 411, 249.

[102] Y. Gauthier, M. Schmid, S. Padovani, E. Lundgren, V. Bus¡, G. Kresse, J. Redinger, P. Varga, *Phys. Rev. Lett.* **2001**, 87, 036103.

[103] A. Aramata, *Modern aspects of electrochemistry* (eds) JO'M Bockris, R.E White and B.E Conway (New York: Plenum) **1997**, vol. 31, p. 181.

[104] E. Herrero, L.J. Buller, H.D Abruna, *Chem. Rev.* **2001**, 101 1897.

[105] D.M. Kolb, M. Prazasnyski, H. Gerischer, *J. Electroanal. Chem.* **1974**, 54, 25.

[106] V. Sudha, M.V. Sangaranarayanan, *J. Phys. Chem.* **2002**, B106**,** 2699.

[107] K. Sasaki, J.X. Wang, H. Naohara, N. Marinkovic, K. More, H. Inada and R.R. Adzic, *Electrochimica. Act*a, 55, **2010,** 2645–2652.

[108] R.R. Adzic, J.X. Wang, B.M. Ocko, J. Mcbreen, EXAFS, XANES, SXS. In *Handbook of Fuel Cells- Fundamentals, Technology and Applications*; W. Vielstich, A.G. Lamm, Eds.; John Wiley & Sons: Chichester, **2003**; Vol.2: Electrocatalysis; pp 279.

[109] *X-ray Absorption-Principles, Applications, Techniques of EXAFS, SEXAFS and XANES*; D.C. Koningsberger, R. Rrins, Eds.; John Wiley & Sons: Toronto, 1988.

[110] J. McBreen, *in Physical Electrochemistry*: Principles, Methods, and Applications (Ed.: I. Rubinstein), Marcel Dekker, New York, **1995**, p. 339.

[111] B. Ravel, M. Newville, *Synchrotron Radia*. 12 (2005) 537.

[112] J.A. Rodriguez, J.C. Hanson, W. Wen, X. Wang, J.L. Brito, A. Martinez-Arias, M. Fernandez-Garcia, *Catal. Today* **2009**, 145, 188-194.

[113] L. Barrio, M. Estrella, G. Zhou, W. Wen, J.C. Hanson, A.B. Hungria, A. Hornes, A. Martinez-Arias, M. Fernandez-Garcia, J.A. Rodriguez, *J. Phys. Chem. C* **2010**, 114, 12689-12697.

[114] H.M. Rietveld, A Profile Refinement Method for Nuclear and Magnetic Structures. *J. Appl. Cryst*. **1969**, 2, 65-71.

[115] B.H. Toby, *J. Appl. Crystal*. **2001**, 34, 210-213.

[116] A.C. Larson, R.B. von Dreele. GSAS General Structure Analysis System. *Report LAUR 86-748*, Los Alamos National Laboratory: Los Alamos, NM, 1995.

[117] C. Creemers, P. Deurinck, *Surf. Interface Anal*., **1997**, 25, 177.

[118] J. Florencio, D. M. Ren, T. T. Tsong, *Surf. Sci*., **1996**, 345, L29.

[119] H. A. Gasteiger, P. N. Ross, Jr., E. J. Cairns, *Surf. Sci*., **1993**, 293, 67.

[120] Y. Gauthier, R. Baudoing-Savois, J. J. W. M. Rosink, M. Sotto, *Surf. Sci*., **1993**, 297, 193.

[121] D. Brown, P. D. Quinn, D. P. Woodruff, T. C. Q. Noakes, P. Bailey, *Surf. Sci*., **2002**, 497, 1.

[122] D. S. Mainardi, P. B. Balbuena, *Langmuir*, **2001**, 17, 2047.

[123] G. Wang, M. A. Van Hove, P. N. Ross, M. I. Baskes, *Journal of Physical Chemistry B*, **2005**, 109, 11683.

[124] A. V. Ruban, H. L. Skriver, J. K. Norskov, *Phys. Rev. B: Condens. Matter Mater. Phys*., **1999**, 59, 15990.

[125] J. Greeley, M. Mavrikakis, *Nat. Mater*., **2004**, 3, 810.

[126] J. Greeley, J. K. Norskov, *Electrochim. Acta*, **2007**, 52, 5829.

[127] Z. Gu, P. B. Balbuena, *J. Phys. Chem. A*, **2006**, 110, 9783.

[128] Z. Gu, P. B. Balbuena, *J. Phys. Chem. C*, **2008**, 112, 5057.

[129] Y. Ma, P. B. Balbuena, *J. Phys. Chem. C*, **2008**, 112, 14520.

[130] V. Stamenkovic, B.S. Mun, K.J.J. Mayrhofer, P.N. Ross, N.M. Markovic, J. Rossmeisl, J. Greeley, and J.K. Nørskov, *Angew. Chem. Int. Ed*. **2006**, 45, 2897 –2901.

[131] G. Kresse, J. Hafner, *Phys. Rev. B* **1993**, 47, 558.

[132] G. Kresse, J. Furthmuller, *Phys. Rev. B* **1996**, 54, 11169.

[133] P.E. Blöchl, *Phys. Rev. B* **1994**, *50*, 17953.

[134] B. Hammer, L.B. Hansen, J.K. Nørskov, *Phys. Rev. B* **1999**, *59*, 7413.

[135] J.X. Wang, H. Inada, L. Wu, Y. Zhu, Y. Choi, P. Liu, W.P. Zhou, R.R. Adzic, *J. Am. Chem. Soc.* **2009**, *131*, 17298.

[136] K. Lee, L. Zhang and J. Zhang, *J. Power Sources* 170, **2007**, p. 291.

[137] J. McBreen, S. Mukerjee, *Interfacial Electrochemistry: Theory, Experiment, and Applications*, A. Wieckowski, Ed.; Marcel Dekker; New York, 1999; pp. 895-914.

[138] B. Predel, *Ir-Ni (Iridium-Nickel)*. O. Madelung, (ed.). SpringerMaterials - The Landolt-Börnstein Database, DOI: 10.1007/10506626_1791

[139] W.B. Pearson, *Handbook of Lattice Spacing's and Structures of Metals and Alloys*, Pergamon Press, New York, 1967, Vol. 2, pp. 592-705.

[140] B.D. Cullity, S.R. Stock, *Elements of X-Ray Diffraction*, Prentice-Hall Inc., 3rd edn., 2001, pp. 167-171.

[141] N.D. Browning, D.J. Wallis, P.D. Nellist, S.J. Pennycook, *Micron* **1997**, 5, 333-348.

[142] M. Pourbaix, *Atlas of Electrochemical Equilibria in Aqueous Solutions*, Pergamon/CEBELCOR, Oxford, 1966, pp.330-342, pp.373-377.

[143] A. I. Frenkel, *Z. Kristallogr*. **2007**, 222, 605-611.

[144] D. Glasner and A.I. Frenkel, *AIP Conf. Proc.*, **2007**, 882, 746-748.

[145] Coordinates of polyhedral clusters are available from: http://www3.bnl.gov/frenkel/coords.html.

[146] http://www1.eere.energy.gov/hydrogenandfuelcells/mypp/

[147] J. R. Kitchin, J. K. Nørskov, M. A. Barteau, J.G. Chen, *Phys. Rev. Lett.*, **2004**, 93, 15.

[148] J. Zhang, K. Sasaki, E. Sutter, R.R. Adzic, *Science* **2007**, 315, 220.

[149] Y. Ma, P.B. Balbuena, *Surf. Sci*. **2008**, 602, 107-113.

[150] F.R. De Boer, R. Boom, W.C.M. Mattens, A.R. Miedema, A.K. Niessen, *Cohesion in Metals*, Amsterdam, North-Holland, 1998.

[151] N.N. Greenwood, A. Earnshaw, *Chemistry of the Elements*, second ed., Butterworth-Heinemann, Oxford, 1997.

[152] B. Fowler, C.A. Lucas, A. Omer, G. Wang, V.R. Stamenkovic, N.M. Markovic, *Electrochim. Acta* **2008**, 53, 6076-6080.

[153] J. Zhang, F.H.B. Lima, M.H. Shao, K. Sasaki, J.X. Wang, J. Hanson, R.R. Adzic, *J. Phys. Chem. B* **2005**, *109*, 22701.

[154] M. Shao, K. Sasaki, N.S. Marinkovic, L. Zhang, R.R. Adzic, *Electrochem. Commun.* **2007**, *9*, 2848.

[155] F.H.B. Lima, J.L. Zhang, M.H. Shao, K. Sasaki, M.B. Vukmirovic, E.A. Ticianelli, R.R. Adzic, *J. Phys. Chem.C.* **2007**, 111, 404-410.

[156] Y. Ma and P.B. Balbuena. *J. Electrochem. Society*, 157, **2010**, B959-B963.

[157] E. Antolini, J.R.C. Salgado, E.R. Gonzalez, *J. Power Sources*, **2006**, 160, 957.

[158] M. Watanabe, K. Tsurumi, T. Mizukami, T. Nakamura, P. Stonehart, *J. Electrochem. Soc.*, **1994**, 141, 2659.

[159] K. Sasaki, K. Kuttiyiel, L. Barrio, D. Su, A. Frenkel, N. Marinkovic, D. Mahajan, R. Adzic , *J. Phys. Chem. C,* **2011**, 115, 9894–9902.

[160] R. Woods, in *Electroanalytical Chemistry*, Vol. 9 (Ed.: A. J. Bard), Marcel Dekker, New York, 1976.

[161] K. Kinoshita, J.T. Lundquist, P. Stonehart, *J. Electroanal. Chem. Interfacial Electrochem* **1973**, 48, 157.